

This work was written as part of one of the author's official duties as an Employee of the United States Government and is therefore a work of the United States Government. In accordance with 17 U.S.C. 105, no copyright protection is available for such works under U.S. Law.

Public Domain Mark 1.0

<https://creativecommons.org/publicdomain/mark/1.0/>

Access to this work was provided by the University of Maryland, Baltimore County (UMBC) ScholarWorks@UMBC digital repository on the Maryland Shared Open Access (MD-SOAR) platform.

Please provide feedback

Please support the ScholarWorks@UMBC repository by emailing scholarworks-group@umbc.edu and telling us what having access to this work means to you and why it's important to you. Thank you.

Atomic data and spectral modeling constraints from high-resolution X-ray observations of the Perseus cluster with Hitomi*

Hitomi Collaboration, Felix AHARONIAN,^{1,2,3} Hiroki AKAMATSU,⁴
Fumie AKIMOTO,⁵ Steven W. ALLEN,^{6,7,8} Lorella ANGELINI,⁹ Marc AUDARD,¹⁰
Hisamitsu AWAKI,¹¹ Magnus AXELSSON,¹² Aya BAMBA,^{13,14}
Marshall W. BAUTZ,¹⁵ Roger BLANDFORD,^{6,7,8} Laura W. BRENNEMAN,¹⁶
Gregory V. BROWN,¹⁷ Esra BULBUL,¹⁵ Edward M. CACKETT,¹⁸
Maria CHERNYAKOVA,¹ Meng P. CHIAO,⁹ Paolo S. COPPI,^{19,20} Elisa COSTANTINI,⁴
Jelle DE PLAA,⁴ Cor P. DE VRIES,⁴ Jan-Willem DEN HERDER,⁴ Chris DONE,²¹
Tadayasu DOTANI,²² Ken EBISAWA,²² Megan E. ECKART,⁹ Teruaki ENOTO,^{23,24}
Yuichiro EZOE,²⁵ Andrew C. FABIAN,²⁶ Carlo FERRIGNO,¹⁰ Adam R. FOSTER,¹⁶
Ryuichi FUJIMOTO,²⁷ Yasushi FUKAZAWA,²⁸ Akihiro FURUZAWA,²⁹
Massimiliano GALEAZZI,³⁰ Luigi C. GALLO,³¹ Poshak GANDHI,³²
Margherita GIUSTINI,⁴ Andrea GOLDWURM,^{33,34} Liyi GU,^{4,†}
Matteo GUAINAZZI,³⁵ Yoshito HABA,³⁶ Kouichi HAGINO,³⁷ Kenji HAMAGUCHI,^{9,38}
Ilana M. HARRUS,^{9,38} Isamu HATSUKADE,³⁹ Katsuhiko HAYASHI,^{22,40}
Takayuki HAYASHI,⁴⁰ Kiyoshi HAYASHIDA,⁴¹ Natalie HELL,¹⁷
Junko S. HIRAGA,⁴² Ann HORNSCHMEIER,⁹ Akio HOSHINO,⁴³ John P. HUGHES,⁴⁴
Yuto ICHINOHE,²⁵ Ryo IIZUKA,²² Hajime INOUE,⁴⁵ Yoshiyuki INOUE,²²
Manabu ISHIDA,²² Kumi ISHIKAWA,²² Yoshitaka ISHISAKI,²⁵ Masachika IWAI,²²
Jelle KAASTRA,^{4,46} Tim KALLMAN,⁹ Tsuneyoshi KAMAE,¹³ Jun KATAOKA,⁴⁷
Satoru KATSUDA,⁴⁸ Nobuyuki KAWAI,⁴⁹ Richard L. KELLEY,⁹
Caroline A. KILBOURNE,⁹ Takao KITAGUCHI,²⁸ Shunji KITAMOTO,⁴³
Tetsu KITAYAMA,⁵⁰ Takayoshi KOHMURA,³⁷ Motohide KOKUBUN,²²
Katsuji KOYAMA,⁵¹ Shu KOYAMA,²² Peter KRETSCHMAR,⁵² Hans A. KRIMM,^{53,54}
Aya KUBOTA,⁵⁵ Hideyo KUNIEDA,⁴⁰ Philippe LAURENT,^{33,34} Shiu-Hang LEE,²³
Maurice A. LEUTENEGGER,^{9,38} Olivier LIMOUSIN,³⁴ Michael LOEWENSTEIN,^{9,56}
Knox S. LONG,⁵⁷ David LUMB,³⁵ Greg MADEJSKI,⁶ Yoshitomo MAEDA,²²
Daniel MAIER,^{33,34} Kazuo MAKISHIMA,⁵⁸ Maxim MARKEVITCH,⁹
Hironori MATSUMOTO,⁴¹ Kyoko MATSUSHITA,⁵⁹ Dan McCAMMON,⁶⁰
Brian R. McNAMARA,⁶¹ Missagh MEHDIPOUR,⁴ Eric D. MILLER,¹⁵
Jon M. MILLER,⁶² Shin MINESHIGE,²³ Kazuhisa MITSUDA,²²
Ikuyuki MITSUISHI,⁴⁰ Takuya MIYAZAWA,⁶³ Tsunefumi MIZUNO,^{28,64}
Hideyuki MORI,⁹ Koji MORI,³⁹ Koji MUKAI,^{9,38} Hiroshi MURAKAMI,⁶⁵
Richard F. MUSHOTZKY,⁵⁶ Takao NAKAGAWA,²² Hiroshi NAKAJIMA,⁴¹
Takeshi NAKAMORI,⁶⁶ Shinya NAKASHIMA,⁵⁸ Kazuhiro NAKAZAWA,^{13,14}
Kumiko K. NOBUKAWA,⁶⁷ Masayoshi NOBUKAWA,⁶⁸ Hirofumi NODA,^{69,70}

Hirokazu ODAKA,⁶ Takaya OHASHI,²⁵ Masanori OHNO,²⁸ Takashi OKAJIMA,⁹
 Naomi OTA,⁶⁷ Masanobu OZAKI,²² Frits PAERELS,⁷¹ Stéphane PALTANI,¹⁰
 Robert PETRE,⁹ Ciro PINTO,²⁶ Frederick S. PORTER,⁹ Katja POTTSCHMIDT,^{9,38}
 Christopher S. REYNOLDS,⁵⁶ Samar SAFI-HARB,⁷² Shinya SAITO,⁴³
 Kazuhiro SAKAI,⁹ Toru SASAKI,⁵⁹ Goro SATO,²² Kosuke SATO,⁵⁹ Rie SATO,²²
 Makoto SAWADA,^{73,†} Norbert SCHARTEL,⁵² Peter J. SERLEMTSOS,⁹
 Hiromi SETA,²⁵ Megumi SHIDATSU,⁵⁸ Aurora SIMIONESCU,²²
 Randall K. SMITH,¹⁶ Yang SOONG,⁹ Łukasz STAWARZ,⁷⁴ Yasuharu SUGAWARA,²²
 Satoshi SUGITA,⁴⁹ Andrew SZYMKOWIAK,²⁰ Hiroyasu TAJIMA,⁵
 Hiromitsu TAKAHASHI,²⁸ Tadayuki TAKAHASHI,²² Shin'ichiro TAKEDA,⁶³
 Yoh TAKEI,²² Toru TAMAGAWA,⁷⁵ Takayuki TAMURA,²² Takaaki TANAKA,⁵¹
 Yasuo TANAKA,^{76,22} Yasuyuki T. TANAKA,²⁸ Makoto S. TASHIRO,⁷⁷
 Yuzuru TAWARA,⁴⁰ Yukikatsu TERADA,⁷⁷ Yuichi TERASHIMA,¹¹
 Francesco TOMBESI,^{9,38,78} Hiroshi TOMIDA,²² Yohko TSUBOI,⁴⁸
 Masahiro TSUJIMOTO,²² Hiroshi TSUNEMI,⁴¹ Takeshi Go TSURU,⁵¹
 Hiroyuki UCHIDA,⁵¹ Hideki UCHIYAMA,⁷⁹ Yasunobu UCHIYAMA,⁴³
 Shutaro UEDA,²² Yoshihiro UEDA,²³ Shin'ichiro UNO,⁸⁰ C. Megan URRY,²⁰
 Eugenio URSINO,³⁰ Shin WATANABE,²² Norbert WERNER,^{28,81,82}
 Dan R. WILKINS,⁶ Brian J. WILLIAMS,⁵⁷ Shinya YAMADA,²⁵
 Hiroya YAMAGUCHI,^{9,56} Kazutaka YAMAOKA,^{5,40} Noriko Y. YAMASAKI,²²
 Makoto YAMAUCHI,³⁹ Shigeo YAMAUCHI,⁶⁷ Tahir YAQOOB,^{9,38} Yoichi YATSU,⁴⁹
 Daisuke YONETOKU,²⁷ Irina ZHURAVLEVA,^{6,7} Abderahmen ZOGHBI,⁶² and
 A. J. J. RAASSEN^{4,83}

¹Dublin Institute for Advanced Studies, 31 Fitzwilliam Place, Dublin 2, Ireland

²Max-Planck-Institut für Kernphysik, PO Box 103980, 69029 Heidelberg, Germany

³Gran Sasso Science Institute, viale Francesco Crispi, 7 67100 L'Aquila (AQ), Italy

⁴SRON Netherlands Institute for Space Research, Sorbonnelaan 2, 3584 CA Utrecht, The Netherlands

⁵Institute for Space-Earth Environmental Research, Nagoya University, Furo-cho, Chikusa-ku, Nagoya, Aichi 464-8601, Japan

⁶Kavli Institute for Particle Astrophysics and Cosmology, Stanford University, 452 Lomita Mall, Stanford, CA 94305, USA

⁷Department of Physics, Stanford University, 382 Via Pueblo Mall, Stanford, CA 94305, USA

⁸SLAC National Accelerator Laboratory, 2575 Sand Hill Road, Menlo Park, CA 94025, USA

⁹NASA, Goddard Space Flight Center, 8800 Greenbelt Road, Greenbelt, MD 20771, USA

¹⁰Department of Astronomy, University of Geneva, ch. d'Écogia 16, CH-1290 Versoix, Switzerland

¹¹Department of Physics, Ehime University, 2-5 Bunkyo-cho, Matsuyama, Ehime 790-8577, Japan

¹²Department of Physics and Oskar Klein Center, Stockholm University, 106 91 Stockholm, Sweden

¹³Department of Physics, The University of Tokyo, 7-3-1 Hongo, Bunkyo-ku, Tokyo 113-0033, Japan

¹⁴Research Center for the Early Universe, School of Science, The University of Tokyo, 7-3-1 Hongo, Bunkyo-ku, Tokyo 113-0033, Japan

¹⁵Kavli Institute for Astrophysics and Space Research, Massachusetts Institute of Technology, 77 Massachusetts Avenue, Cambridge, MA 02139, USA

¹⁶Smithsonian Astrophysical Observatory, 60 Garden St., MS-4. Cambridge, MA 02138, USA

¹⁷Lawrence Livermore National Laboratory, 7000 East Avenue, Livermore, CA 94550, USA

¹⁸Department of Physics and Astronomy, Wayne State University, 666 W. Hancock St, Detroit, MI 48201, USA

¹⁹Department of Astronomy, Yale University, New Haven, CT 06520-8101, USA

- ²⁰Department of Physics, Yale University, New Haven, CT 06520-8120, USA
- ²¹Centre for Extragalactic Astronomy, Department of Physics, University of Durham, South Road, Durham, DH1 3LE, UK
- ²²Japan Aerospace Exploration Agency, Institute of Space and Astronautical Science, 3-1-1 Yoshino-dai, Chuo-ku, Sagami-hara, Kanagawa 252-5210, Japan
- ²³Department of Astronomy, Kyoto University, Kitashirakawa-Oiwake-cho, Sakyo-ku, Kyoto, Kyoto 606-8502, Japan
- ²⁴The Hakubi Center for Advanced Research, Kyoto University, Yoshida-honmachi, Sakyo-ku, Kyoto, Kyoto 606-8501, Japan
- ²⁵Department of Physics, Tokyo Metropolitan University, 1-1 Minami-Osawa, Hachioji, Tokyo 192-0397, Japan
- ²⁶Institute of Astronomy, University of Cambridge, Madingley Road, Cambridge, CB3 0HA, UK
- ²⁷Faculty of Mathematics and Physics, Kanazawa University, Kakuma-machi, Kanazawa, Ishikawa 920-1192, Japan
- ²⁸School of Science, Hiroshima University, 1-3-1 Kagamiyama, Higashi-Hiroshima, Hiroshima 739-8526, Japan
- ²⁹Fujita Health University, 1-98 Dengakugakubo, Kutsukake-cho, Toyoake, Aichi 470-1192, Japan
- ³⁰Physics Department, University of Miami, 1320 Campo Sano Dr., Coral Gables, FL 33146, USA
- ³¹Department of Astronomy and Physics, Saint Mary's University, 923 Robie Street, Halifax, NS, B3H 3C3, Canada
- ³²Department of Physics and Astronomy, University of Southampton, Highfield, Southampton, SO17 1BJ, UK
- ³³Laboratoire APC, 10 rue Alice Domon et Léonie Duquet, 75013 Paris, France
- ³⁴CEA Saclay, 91191 Gif sur Yvette, France
- ³⁵European Space Research and Technology Center, Keplerlaan 1 2201 AZ Noordwijk, The Netherlands
- ³⁶Department of Physics and Astronomy, Aichi University of Education, 1 Hirosawa, Igaya-cho, Kariya, Aichi 448-8543, Japan
- ³⁷Department of Physics, Tokyo University of Science, 2641 Yamazaki, Noda, Chiba 278-8510, Japan
- ³⁸Department of Physics, University of Maryland Baltimore County, 1000 Hilltop Circle, Baltimore, MD 21250, USA
- ³⁹Department of Applied Physics and Electronic Engineering, University of Miyazaki, 1-1 Gakuen Kibanadai-Nishi, Miyazaki, Miyazaki 889-2192, Japan
- ⁴⁰Department of Physics, Nagoya University, Furo-cho, Chikusa-ku, Nagoya, Aichi 464-8602, Japan
- ⁴¹Department of Earth and Space Science, Osaka University, 1-1 Machikaneyama-cho, Toyonaka, Osaka 560-0043, Japan
- ⁴²Department of Physics, Kwansei Gakuin University, 2-1 Gakuen, Sanda, Hyogo 669-1337, Japan
- ⁴³Department of Physics, Rikkyo University, 3-34-1 Nishi-Ikebukuro, Toshima-ku, Tokyo 171-8501, Japan
- ⁴⁴Department of Physics and Astronomy, Rutgers University, 136 Frelinghuysen Road, Piscataway, NJ 08854, USA
- ⁴⁵Meisei University, 2-1-1 Hodokubo, Hino, Tokyo 191-8506, Japan
- ⁴⁶Leiden Observatory, Leiden University, PO Box 9513, 2300 RA Leiden, The Netherlands
- ⁴⁷Research Institute for Science and Engineering, Waseda University, 3-4-1 Ohkubo, Shinjuku-ku, Tokyo 169-8555, Japan
- ⁴⁸Department of Physics, Chuo University, 1-13-27 Kasuga, Bunkyo-ku, Tokyo 112-8551, Japan
- ⁴⁹Department of Physics, Tokyo Institute of Technology, 2-12-1 Ookayama, Meguro-ku, Tokyo 152-8550, Japan
- ⁵⁰Department of Physics, Toho University, 2-2-1 Miyama, Funabashi, Chiba 274-8510, Japan
- ⁵¹Department of Physics, Kyoto University, Kitashirakawa-Oiwake-cho, Sakyo-ku, Kyoto, Kyoto 606-8502, Japan
- ⁵²European Space Astronomy Center, Camino Bajo del Castillo, s/n., 28692 Villanueva de la Cañada, Madrid, Spain

- ⁵³Universities Space Research Association, 7178 Columbia Gateway Drive, Columbia, MD 21046, USA
- ⁵⁴National Science Foundation, 4201 Wilson Blvd, Arlington, VA 22230, USA
- ⁵⁵Department of Electronic Information Systems, Shibaura Institute of Technology, 307 Fukasaku, Minuma-ku, Saitama, Saitama 337-8570, Japan
- ⁵⁶Department of Astronomy, University of Maryland, College Park, MD 20742, USA
- ⁵⁷Space Telescope Science Institute, 3700 San Martin Drive, Baltimore, MD 21218, USA
- ⁵⁸Institute of Physical and Chemical Research, 2-1 Hirosawa, Wako, Saitama 351-0198, Japan
- ⁵⁹Department of Physics, Tokyo University of Science, 1-3 Kagurazaka, Shinjuku-ku, Tokyo 162-8601, Japan
- ⁶⁰Department of Physics, University of Wisconsin, Madison, WI 53706, USA
- ⁶¹Department of Physics and Astronomy, University of Waterloo, 200 University Avenue West, Waterloo, Ontario, N2L 3G1, Canada
- ⁶²Department of Astronomy, University of Michigan, 1085 South University Avenue, Ann Arbor, MI 48109, USA
- ⁶³Okinawa Institute of Science and Technology Graduate University, 1919-1 Tancha, Onna-son, Kunigami-gun, Okinawa 904-0495, Japan
- ⁶⁴Hiroshima Astrophysical Science Center, Hiroshima University, 1-3-1 Kagamiyama, Higashi-Hiroshima, Hiroshima 739-8526, Japan
- ⁶⁵Faculty of Liberal Arts, Tohoku Gakuin University, 2-1-1 Tenjinzawa, Izumi-ku, Sendai, Miyagi 981-3193, Japan
- ⁶⁶Faculty of Science, Yamagata University, 1-4-12 Kojirakawa-machi, Yamagata, Yamagata 990-8560, Japan
- ⁶⁷Department of Physics, Nara Women's University, Kitauoyanishi-machi, Nara, Nara 630-8506, Japan
- ⁶⁸Department of Teacher Training and School Education, Nara University of Education, Takabatake-cho, Nara, Nara 630-8528, Japan
- ⁶⁹Frontier Research Institute for Interdisciplinary Sciences, Tohoku University, 6-3 Aramaki-zaaoba, Aoba-ku, Sendai, Miyagi 980-8578, Japan
- ⁷⁰Astronomical Institute, Tohoku University, 6-3 Aramaki-zaaoba, Aoba-ku, Sendai, Miyagi 980-8578, Japan
- ⁷¹Astrophysics Laboratory, Columbia University, 550 West 120th Street, New York, NY 10027, USA
- ⁷²Department of Physics and Astronomy, University of Manitoba, Winnipeg, MB R3T 2N2, Canada
- ⁷³Department of Physics and Mathematics, Aoyama Gakuin University, 5-10-1 Fuchinobe, Chuo-ku, Sagami-hara, Kanagawa 252-5258, Japan
- ⁷⁴Astronomical Observatory of Jagiellonian University, ul. Orla 171, 30-244 Kraków, Poland
- ⁷⁵RIKEN Nishina Center, 2-1 Hirosawa, Wako, Saitama 351-0198, Japan
- ⁷⁶Max-Planck-Institut für extraterrestrische Physik, Giessenbachstrasse 1, 85748 Garching, Germany
- ⁷⁷Department of Physics, Saitama University, 255 Shimo-Okubo, Sakura-ku, Saitama, Saitama 338-8570, Japan
- ⁷⁸Department of Physics, University of Rome "Tor Vergata", Via della Ricerca Scientifica 1, I-00133 Rome, Italy
- ⁷⁹Faculty of Education, Shizuoka University, 836 Ohya, Suruga-ku, Shizuoka, Shizuoka 422-8529, Japan
- ⁸⁰Faculty of Health Sciences, Nihon Fukushi University, 26-2 Higashi Haemi-cho, Handa, Aichi 475-0012, Japan
- ⁸¹MTA-Eötvös University Lendület Hot Universe Research Group, Pázmány Péter sétány 1/A, Budapest, 1117, Hungary
- ⁸²Department of Theoretical Physics and Astrophysics, Faculty of Science, Masaryk University, Kotlářská 2, Brno, 602 00, Czech Republic
- ⁸³Astronomical Institute "Anton Pannekoek", University of Amsterdam, Science Park 904, 1098 XH Amsterdam, The Netherlands

*Corresponding authors are Makoto Sawada, Liyi Gu, Jelle Kaastra, Randall K. Smith, Adam R. Foster, Gregory V. Brown, Hirokazu Odaka, Hiroki Akamatsu, and Takayuki Hayashi.

†E-mail: sawada@phys.aoyama.ac.jp; L.Gu@sron.nl

Received 2017 July 29; Accepted 2017 December 13

Abstract

The Hitomi Soft X-ray Spectrometer spectrum of the Perseus cluster, with ~ 5 eV resolution in the 2–9 keV band, offers an unprecedented benchmark of the atomic modeling and database for hot collisional plasmas. It reveals both successes and challenges of the current atomic data and models. The latest versions of AtomDB/APEC (3.0.8), SPEX (3.03.00), and CHIANTI (8.0) all provide reasonable fits to the broad-band spectrum, and are in close agreement on best-fit temperature, emission measure, and abundances of a few elements such as Ni. For the Fe abundance, the APEC and SPEX measurements differ by 16%, which is 17 times higher than the statistical uncertainty. This is mostly attributed to the differences in adopted collisional excitation and dielectronic recombination rates of the strongest emission lines. We further investigate and compare the sensitivity of the derived physical parameters to the astrophysical source modeling and instrumental effects. The Hitomi results show that accurate atomic data and models are as important as the astrophysical modeling and instrumental calibration aspects. Substantial updates of atomic databases and targeted laboratory measurements are needed to get the current data and models ready for the data from the next Hitomi-level mission.

Key words: instrumentation: spectrographs — methods: data analysis — X-rays: general

1 Introduction

Many major achievements in X-ray studies of clusters of galaxies were made possible by the advent of new X-ray spectroscopic instruments. The proportional counters on the Ariel V mission (spectral resolving power $R \equiv E/\Delta E \sim 6$) revealed the highly ionized Fe line emission near 7 keV in the Perseus cluster (Mitchell et al. 1976), establishing the thermal origin of cluster X-rays. The CCDs ($R = 10$ –60) on board the ASCA satellite further identified line emissions from O, Ne, Mg, Si, S, Ar, Ca, and Ni in the hot intracluster medium (ICM; Fukazawa et al. 1994; Mushotzky et al. 1996). The Reflection Grating Spectrometer (RGS; $R = 50$ –100 for spatially extended sources) on board XMM-Newton (Peterson et al. 2001; Tamura et al. 2001; Kaastra et al. 2001) discovered the lack of strong cooling flows in cool-core clusters. Most recently, the Soft X-ray Spectrometer (SXS; Kelley et al. 2016) on board the Hitomi satellite (Takahashi et al. 2016) disclosed the low energy density of turbulent motions in the central region of the Perseus cluster with a resolving power of $R \sim 1250$ (Hitomi Collaboration 2016). Each iteration of higher-resolution spectroscopy enhances our understanding of clusters and other cosmic objects.

As more high-resolution X-ray spectra become available, the X-ray community—including observers, theoreticians, and laboratory scientists—urgently needs accurate and complete atomic data and plasma models. As a first step in achieving this, we will compare the current data

and models (collectively called “codes” hereafter). The most used plasma codes in X-ray astronomy are AtomDB/APEC (Smith et al. 2001; Foster et al. 2012), SPEX (Kaastra et al. 1996), and CHIANTI (Dere et al. 1997; Del Zanna et al. 2015). The AtomDB code descends from the original work of Raymond and Smith (1977), SPEX started with Mewe (1972), and CHIANTI started with Landini and Monsignori Fossi (1970). All these codes have evolved significantly since their initial beginnings, often stimulated by the challenges imposed by new generations of instruments. It is clear that a comparison of these codes is strongly needed to verify their scientific output and to understand systematic uncertainties in the results originating from the codes and atomic databases. However, few code comparisons have been made (e.g., Audard et al. 2003), and in particular, so far there is no comparison based on high-resolution X-ray spectra of galaxy clusters.

The Hitomi X-ray observatory was launched on 2016 February 17. Among the main scientific instruments, the SXS has an unprecedented resolving power of $R \sim 1250$ at 6 keV over a 6×6 pixel array ($3' \times 3'$). It has a near-Gaussian energy response with FWHM = 4–6 eV over the 0.3–12 keV band (A. M. Leutenegger et al. in preparation). The X-ray mirror has an angular resolution with a half-power diameter of $1.2'$ (Maeda et al. 2018). A gate valve was in place for early observations to minimize the risk of contamination from out-gassing of the spacecraft (Tsujiimoto et al. 2016), which includes a Be window that absorbs most

X-rays below ~ 2 keV. As the SXS is a non-dispersive instrument (unlike gratings) it can be used to observe extended objects without a loss of spectral resolution. This makes the SXS the best instrument for high-resolution spectroscopic studies of galaxy clusters. The Perseus cluster was observed as the first-light target of the SXS, and the first paper showing its spectroscopic capabilities was focused on the turbulence in the Perseus cluster (Hitomi Collaboration 2016).

With these data, we can also measure abundances (Hitomi Collaboration 2017b, hereafter *Z paper*), temperature structure (Hitomi Collaboration 2018c, *T paper*), and resonance scattering (Hitomi Collaboration 2018b, *RS paper*). These quantities are essential to understanding the origin and evolution of galaxy clusters—see the review by Böhringer and Werner (2010). Metal abundances trace products of billions of supernovae explosions integrated over cosmic time, and the measurements are crucial for understanding chemical evolution of ICM as well as the evolutions and explosions of progenitor stars (Werner et al. 2008). Temperature structure or anisothermality gives an insight into thermodynamics in ICM, and is thus important for understanding the heating mechanism against effective radiative cooling in a dense core region (Peterson & Fabian 2006). Resonance scattering is another indirect tool to assess turbulence, one of the candidate mechanisms of ICM heating. The required precision for these quantities depends on the astrophysical objectives: for cosmic star-formation history the Ni-to-Fe abundance ratio needs to be measured to $\sim 10\%$, and for detection of resonance scattering with the Fe He α complex the forbidden-to-resonance (z-to-w) line ratio must be measured to within a few percent, for instance (see individual topical papers for details).

In this paper we focus on the atomic physics and modeling aspects of the Perseus spectrum with the Hitomi SXS. We show that this high-resolution spectrum offers a sensitive probe of several important aspects of cluster physics including turbulence, elemental abundance measurements, and structures in temperature and velocity (section 3). We investigate the sensitivity of the related derived physical parameters to various aspects of the spectroscopic codes (section 4) and their underlying atomic data (section 5), spectral (section 6) and astrophysical (sections 7 and 8) modelings, as well as fitting techniques (section 9). By consolidating these systematic factors and comparing them to statistical uncertainties as well as the systematic factors due to instrumental calibration effects (appendix 3), we can evaluate with what precisions the important quantities can be determined. This allows us to be optimally prepared for future high-resolution X-ray missions. We highlight the relative changes to each parameter by using different atomic modelings and so on, rather than the changes in fitting statistics, since the former is more funda-

mental for understanding the systematic uncertainties in the scientific results. The astrophysical interpretation of our derived parameters is not discussed in this paper, but will be in a series of separate papers focusing in greater detail on the relevant astrophysics, e.g., abundances (*Z paper*), temperature structure (*T paper*), resonance scattering (*RS paper*), velocity structure (Hitomi Collaboration 2018a, hereafter *V paper*), and the central active galactic nucleus (AGN) of the Perseus cluster (Hitomi Collaboration 2018d, *AGN paper*). Also, we do not examine combined effects of different types of systematic factors (e.g., plasma code dependence in the detailed astrophysical modeling like multi-temperature models), which will be separately discussed in the individual topical papers.

2 Data reduction

In this paper, the cleaned event data in the pipeline products version 03.01.005.005 are analyzed with the Hitomi software version 005a and the calibration database (CALDB) version 005 (Angelini et al. 2016).¹ There are four Hitomi observations of the Perseus cluster (name: sequence number = Obs 1: 100040010, Obs 2: 100040020, Obs 3: 100040030–100040050, and Obs 4: 100040060). The instrument had nearly reached thermal equilibrium by Obs 4 (Fujimoto et al. 2016), and the calibrations of Obs 2 and Obs 3 can be checked against Obs 4 because of their overlapping fields of view (FOVs), but the FOV of Obs 1 does not overlap the others and the instrument was most out of equilibrium during that pointing. Hence only Obs 2, 3, and 4 are used in this work.

Events registered during low-Earth elevation angles below two degrees and during passages of the South Atlantic Anomaly were already excluded by the pipeline processing which created the cleaned events file. Events coincident with the particle veto had also already been rejected. Data were further screened by criteria described as “recommended screening” in the Hitomi data reduction guide² to remove those with distorted pulse shapes or coincident events in any two pixels, which further reduces the background, although the difference is negligible given the surface brightness of the Perseus cluster. For all the three observations (Obs 2–4), only high-resolution primary events (an event with no pulse in the interval 69.2 ms before or after it) were extracted and used. This choice is fine because relative ratios are the same between different event types (Seta et al. 2012; Ishisaki et al. 2016).

The line broadening due to the spatial velocity gradient in the ICM is removed, since it is not relevant to the atomic

¹ For the SXS pipeline products and CALDB, these are identical to the latest ones (03.01.006.008 and 009, respectively).

² See (<https://heasarc.gsfc.nasa.gov/docs/hitomi/analysis/>).

study. To do this, we apply an additional energy scale correction (also used in Hitomi Collaboration 2016, 2017a), forcing the strong Fe-K lines to appear at the same energy in each pixel, aligned to the same redshift as the central AGN ($z = 0.01756$ or $cz = 5264 \text{ km s}^{-1}$; Ferruit et al. 1997). This also removes residual gain errors in the Fe-K band. The effect of the spatial velocity correction on the baseline-model fitting (section 3) is discussed in appendix 3. A recent measurement of NGC 1275 indicates an alternative redshift of 0.017284 ± 0.00005 (V paper). In this paper, we do not refer to the new value, since its impact on the other fitting parameters would be washed out by the non-linear energy-scale correction applied later (appendix 1) or by the redshift component included in the baseline model (section 3).

The large-size redistribution matrix files (RMFs) for high-primary events created by `sxsmkrmf` are used to take into account the main Gaussian component, the low-energy exponential tail, and escape peaks of the line spread function (A. M. Leutenegger et al. in preparation). We have also tested two different types of RMFs: one is the small-size RMFs, which include only the Gaussian core, and the other is the extra-large-size RMFs with all components in the large-size RMFs plus electron-loss continuum. The effect of changing the RMF type is discussed in appendix 3. The ancillary response files (ARFs) are generated separately for the diffuse emission and the point-source component. To enhance the precision of the diffuse ARFs, a background-subtracted Chandra image of the Perseus cluster in the 1.8–9.0 keV band, whose AGN core is replaced with the average value of the surrounding regions, is used to provide the spatial distribution of seed photons. Since the effective area is estimated based on the input image with a radius of $12'$, which is larger than the detector FOV ($3' \times 3'$), the measured spectral normalization reported in this paper is larger than the actual value. We do not correct this effect since this paper is focused on the relative uncertainties instead of the absolute values. We have further tested using the point-source ARF for both components, and show the effects in appendix 3.

The non-X-ray background (NXB) of the SXS is much lower than those of the X-ray CCDs thanks to the anti-coincidence screening, which reduces the NXB rate by a factor of ~ 10 (Kilbourne et al. 2018). We extract the NXB spectrum from Earth occultation data with `sxsnxbgen`, and screen it with the standard NXB criteria and with the same additional screening as the source events. The NXB spectrum is taken into account as a SPEX *file* model in the baseline analysis (section 3). Other background components, which include the cosmic X-ray background and Galactic foreground emission, are negligible for the Perseus data. The relative changes of the baseline parameters for a fitting in the absence of the NXB is shown in appendix 3.

The main remaining issue in the data analysis is that the planned calibration procedures were not fully available for these early observations. In particular, the contemporaneous calibration of the energy scale (or gain) for the detector array was not yet carried out. The previous Hitomi papers (Hitomi Collaboration 2016, 2017a) were focused on a relatively narrow energy range; however, in this work we study a wide energy band of 1.9–9.5 keV. This forces us to apply two additional corrections to the energy scale and effective area, as described in appendix 1.

3 Baseline model

The result of a spectral model fit is a list of parameters representing the source. These parameters depend on several factors, like the statistical quality of the data, instrument calibration, background subtraction method, fitting techniques, spectral model components, physical processes included in the spectral model, and atomic parameters. All of these factors contribute to the final set of source parameters that is derived. Apart from the statistical uncertainties, all other factors act like a kind of systematic uncertainty, and so by carefully analyzing each individual contribution we can assess its contribution to the final uncertainty.

We proceed as follows. Below, we define our baseline best-fit model and explain why we incorporate each component in the model. We then list the best-fit parameters with their statistical uncertainties. The effects of the different systematic factors are in general not excessively large, and therefore we list their impact showing by how much the best-fit parameters are increased or decreased due to these factors. Usually the statistical uncertainties on the best-fit parameters are very similar in all investigated cases, so we only list the statistical uncertainties of the baseline model.

We use the SPEX package (Kaastra et al. 1996) to define the baseline model because it allows us to test the system in a straightforward way. The version of SPEX that is used here is 3.03.00. It calculates all relevant rates, ion concentrations, level populations, and line emissivities on the fly (see subsection 4.1 for more details).

We use optimally binned spectra (using the SPEX *obin* command structure; see appendix 1.3) with the C-statistic (Cash 1979). This choice is elaborated later (section 9).

All abundances are relative to the Lodders and Palme (2009) proto-solar abundances with free values relative to those abundances for the relevant elements.

The dominant spectral component is a collisional ionization equilibrium (CIE) plasma, with a temperature of about 4 keV (Hitomi Collaboration 2016), modeled with the SPEX *cie* model. For the ionization balance we choose the Urdampilleta, Kaastra, and Mehdipour (2017, hereafter U17) ionization balance (for more details see

subsection 5.4). The electron temperature and abundances of Si, S, Ar, Ca, Cr, Mn, Fe, and Ni are free parameters; the abundances of all other metals (usually with no or very weak lines in the bandpass of the Hitomi SXS) are tied to the Fe abundance. In addition, we leave the turbulent velocity free: the value of this turbulent velocity has been discussed in detail in Hitomi Collaboration (2016). Although in SPEX the magnitude of turbulence is parametrized by a two-dimensional root-mean-square velocity v_{mic} assuming isotropic velocity distribution, we convert it into one-dimensional line-of-sight (LOS) velocity dispersion $\sigma_v (= v_{\text{mic}}/\sqrt{2})$ and use it throughout this paper to enable direct comparisons to the previous studies (Hitomi Collaboration 2016, 2017a).

The Hitomi SXS spectrum of the Perseus cluster shows clear signatures of resonance scattering (RS paper); in addition, we may expect absorption of He-like line emission by Li-like ions (Mehdipour et al. 2015). To account for both effects, we include the absorption from a CIE plasma as modeled by the SPEX *hot* model in our model. The *hot* model calculates the continuum and line absorption from a plasma with the temperature, chemical composition, turbulent velocity, and outflow velocity as free parameters. This absorption is applied to all emission components from the cluster. Because the FOV of the Hitomi SXS is relatively small compared to the size of the Perseus cluster, the effects of resonance scattering to the lowest order imply the removal of photons from the line of sight toward the cluster core: we do not observe the re-emitted photons further away from the nucleus. A more sophisticated resonance scattering model is discussed elsewhere (RS paper). In order not to over-constrain the model, we leave only the column density of the hot absorbing gas, $N_{\text{H,hot}}$, free, and tie the other parameters (electron temperature, abundances, turbulent and outflow velocities) to the values of the main 4 keV emission component (but see section 7).

Our spectrum also contains a contribution from the central AGN of NGC 1275. This is modeled by a power law (SPEX component *pow*) plus two Gaussians (*gaus*) for the neutral Fe $K\alpha$ lines. We use the power-law model which has a 2–10 keV luminosity of 2.4×10^{36} W or a flux of 3.5×10^{-14} W m $^{-2}$, almost one fifth of the total 2–10 keV luminosity of the observed field, and a photon index of 1.91. The Gaussian lines have rest-frame energies of 6.391 keV and 6.404 keV, an intrinsic FWHM of 25 eV, and a total luminosity of 5.6×10^{33} W or a total flux of 8.0×10^{-17} W m $^{-2}$. We have kept the parameters of the central AGN frozen in our fits to the above values. The above model and parameter values are from the initial evaluation for the AGN paper, which has later been updated. Updating the AGN spectrum modeling results in slightly different best-fit values of the baseline

model (subsection 8.3), but the changes are so small that relative differences in the ICM parameters due to other systematic factors are unchanged. Thus we use the original AGN model and parameters throughout this paper, except in subsection 8.3.

Further, we apply the cosmological redshift (SPEX *reds* component) to the model, but leave it as a free parameter for the baseline model to account for any residual systematic energy scale corrections (either of instrumental or astrophysical origin; this is not important for the present study).

The last spectral component applied to all spectra is another *hot* component to account for the interstellar absorption from our Galaxy; we have frozen the temperature at 0.5 eV (essentially a neutral plasma), with a column density of 1.38×10^{21} cm $^{-2}$, following the argument in Hitomi Collaboration (2017a). The abundances are frozen to the proto-solar abundances (Lodders & Palme 2009).

The model further contains a component of pure neutral Be and a correction factor for the effective area (see appendix 1.2): these serve purely as instrumental effective area corrections and are kept frozen for our modeling.

To summarize, the baseline model starts with thermal ICM and AGN components, self-absorbed, redshifted, absorbed again by the foreground, and corrected for instrumental effects. The free parameters of our model are then the emission measure Y and temperature kT of the hot gas, the turbulent velocity σ_v of the hot gas, the abundances of Si, S, Ar, Ca, Cr, Mn, Fe, and Ni, the effective absorption column of the hot cluster gas $N_{\text{H,hot}}$, and the overall redshift of the system z . This baseline model achieves a C-statistic value (C_{stat}) of 4926 for an expected value of 4876 ± 99 .

The best-fit parameters of our model are given in table 1. It is beyond the scope of this paper to discuss the astrophysical interpretation of the temperature, abundances, and resonance scattering; therefore, these are discussed in greater detail by the T, Z, and RS papers, respectively.

In the following sections, which form the core of our paper, we investigate in more detail the systematic effects that affect the best-fit parameters of this baseline model. We do so in table 1 by showing the difference in best-fit C-statistic and the best-fit model parameters, for different assumptions in our modeling. In several cases we also show the relative difference in the predicted model spectra.

We consider the following systematic effects: the plasma code that is used (section 4), the atomic database in the background (section 5), different choices for details of the plasma modeling (section 6), astrophysical modeling effects (section 7), the role of other spectral components apart from the main hot plasma (section 8), and spectral fitting techniques (section 9). Those due to instrumental calibration aspects are separately examined in appendix 3.

Table 1. Parameters of the reference model and sensitivity to model assumptions.*

Model	C_{stat}	Y^\dagger (10^{73} m^{-3})	kT^\dagger (keV)	σ_v^\dagger (km s^{-1})	Abundance (solar) [‡]								$N_{\text{H,hot}}^\dagger$ (10^{24} m^{-2})	cz^\dagger (km s^{-1})
					Si	S	Ar	Ca	Cr	Mn	Fe	Ni		
Baseline	4926.03 [§]	3.73	3.969	156	0.91	0.94	0.83	0.88	0.70	0.74	0.827	0.76	18.8	5264
Stat. error	—	0.01	0.017	3	0.05	0.03	0.04	0.04	0.10	0.15	0.008	0.05	1.3	2
<i>Plasma codes (section 4):</i>														
SPEX v2	1125.06	0.03	0.031	14	−0.13	−0.14	−0.05	−0.08	—	—	−0.026	0.11	−0.8	−6
SPEX v3.00	2372.33	−0.08	0.263	12	0.03	0.09	0.10	0.06	−0.11	−0.12	−0.243	−0.28	−18.8	−2
APEC v3.0.2	670.06	0.07	−0.039	−13	−0.24	−0.21	−0.15	−0.13	−0.24	−0.39	−0.047	−0.17	−2.7	1
APEC v3.0.8	22.27	0.03	0.071	−16	−0.10	−0.07	−0.05	−0.07	0.01	−0.05	−0.134	−0.05	−7.6	−6
CHIANTI v8.0	327.44	0.01	0.002	4	−0.17	−0.12	0.14	−0.08	—	—	0.011	−0.04	−1.8	8
Cloudy v13.04	21416.07	0.74	−0.370	−7	−0.54	−0.52	−0.53	−0.46	−0.43	−0.15	−0.399	0.14	−18.8	−8
<i>Atomic data (section 5):</i>														
Fe xxv triplet	−10.68	0.00	0.003	1	0.00	0.00	0.00	0.00	0.00	0.00	−0.007	0.00	−0.4	0
AR85 balance	104.80	0.13	0.017	−3	−0.02	−0.02	−0.03	−0.02	—	—	0.017	−0.02	2.4	1
AR92 balance	94.65	0.09	0.021	−4	−0.02	−0.02	−0.03	−0.02	—	—	0.021	−0.03	2.0	0
B09 balance	−18.62	−0.13	0.003	−2	0.00	0.01	0.00	0.00	−0.01	−0.01	0.029	0.01	1.1	0
<i>Plasma modeling (section 6):</i>														
Voigt profile	−8.28	0.01	−0.003	−4	−0.01	−0.01	0.00	0.00	0.01	0.00	−0.003	0.01	−1.2	1
g_{acc}	−0.54	−0.01	−0.005	0	0.00	0.00	0.00	0.00	0.00	0.00	0.006	0.00	−0.1	0
n_{max}	61.46	−0.01	0.006	−1	0.02	0.04	0.02	0.01	−0.01	−0.03	0.023	0.00	1.0	0
<i>Astrophysical modeling (section 7):</i>														
T_{ion} free	−0.02	0.00	0.000	−1	0.00	0.00	0.00	0.00	0.00	−0.01	0.000	0.00	−0.1	0
RT free	−3.26	−0.01	0.026	−1	−0.02	−0.02	−0.01	−0.01	−0.01	−0.02	0.001	−0.01	0.7	0
Ionizing	−5.46	−0.02	0.025	0	0.01	−0.01	−0.06	−0.06	−0.02	−0.04	0.000	−0.01	0.8	0
Recombining	−9.19	0.02	−0.036	2	−0.02	−0.02	−0.01	0.00	0.03	0.02	0.000	0.01	−1.5	0
σ_T free	−60.90	0.13	−0.139	2	−0.10	−0.10	−0.04	0.01	0.08	0.10	0.024	0.03	−2.3	0
He abund.	−0.07	−0.08	−0.001	0	0.02	0.03	0.02	0.02	0.02	0.01	0.025	0.02	−0.6	0
<i>Spectral components (section 8):</i>														
No RS	341.02	0.05	−0.015	13	−0.05	−0.04	−0.03	−0.02	0.04	0.01	−0.094	0.01	≡0	4
Hot comp. free	−1.40	0.00	0.000	2	0.00	0.00	0.00	0.00	0.00	0.00	0.003	0.00	1.3	0
CX	−13.34	0.00	0.018	−3	−0.02	−0.01	0.00	−0.01	−0.01	−0.02	−0.042	0.00	−1.4	−1
No AGN	624.54	0.68	0.523	4	−0.01	−0.05	−0.09	−0.14	−0.15	−0.12	−0.206	−0.16	12.8	3
New AGN	8.42	0.18	0.028	0	−0.03	−0.03	−0.03	−0.04	−0.04	−0.04	−0.041	−0.03	1.3	0
<i>Fitting techniques (section 9):</i>														
χ^2	54.69	−0.01	−0.045	−1	−0.03	−0.01	0.00	−0.01	0.03	0.01	0.007	0.02	−0.6	0
χ^2 , no binning	—	−0.01	−0.206	−1	−0.12	−0.07	−0.03	−0.01	0.09	0.14	0.027	0.02	−3.1	0
<i>Instrumental effects (appendix 3):</i>														
No vel. cor.	61.70	0.00	0	13	0.00	0.00	0.00	0.00	−0.02	−0.02	0.001	0.01	1.0	−23
Small RMF	−4.42	0.01	−0.023	0	−0.01	−0.02	−0.01	−0.01	−0.01	−0.02	−0.003	0.00	−0.2	0
XL RMF	12.36	−0.02	0.035	0	0.00	0.03	0.02	0.02	0.02	0.01	0.010	0.00	0.1	0
No NXB	8.78	0.00	0.017	0	0.00	0.00	0.00	0.00	−0.01	−0.01	−0.003	−0.01	0.3	0
PS ARF	29.54	0.02	−0.052	0	−0.04	−0.02	0.00	0.00	0.01	0.04	0.003	0.00	−0.7	0
No ARF cor.	38.48	0.05	−0.076	1	−0.03	−0.03	−0.03	−0.03	0.02	0.05	−0.006	−0.03	−0.6	2
Ground ARF	190.52	−0.16	−0.123	0	0.03	0.00	0.02	0.06	−0.04	0.02	0.017	0.04	−1.8	−1
Crab ARF	13.36	−0.11	0.066	1	0.02	0.01	0.00	0.02	0.05	0.08	0.031	0.03	0.0	0
New arfgen	−1.55	0.78	0.004	0	0.00	0.00	0.00	0.00	0.00	0.00	0.000	0.00	0.1	0
No gain cor.	626.73	0.01	0.003	4	−0.13	−0.06	−0.02	−0.01	−0.01	−0.01	−0.008	0.00	−0.5	14
<i>Improved model (section 10):</i>														
	−146.77	—	—	—	−0.14	−0.11	−0.01	0.05	0.08	0.06	—	0.05	−8.3	0

*The first two lines give the best-fit values with their 1σ statistical uncertainty. The next lines show the parameter differences of the tested models relative to the baseline model. Differences larger than 3σ statistical uncertainty are emphasized in bold.

[†]Emission measure Y , temperature kT , LOS velocity dispersion σ_v , column density of hot gas absorption $N_{\text{H,hot}}$, and redshift cz .

[‡]Elemental abundance relative to the proto-solar values of Lodders and Palme (2009).

[§]Expected value for the baseline model is 4876.

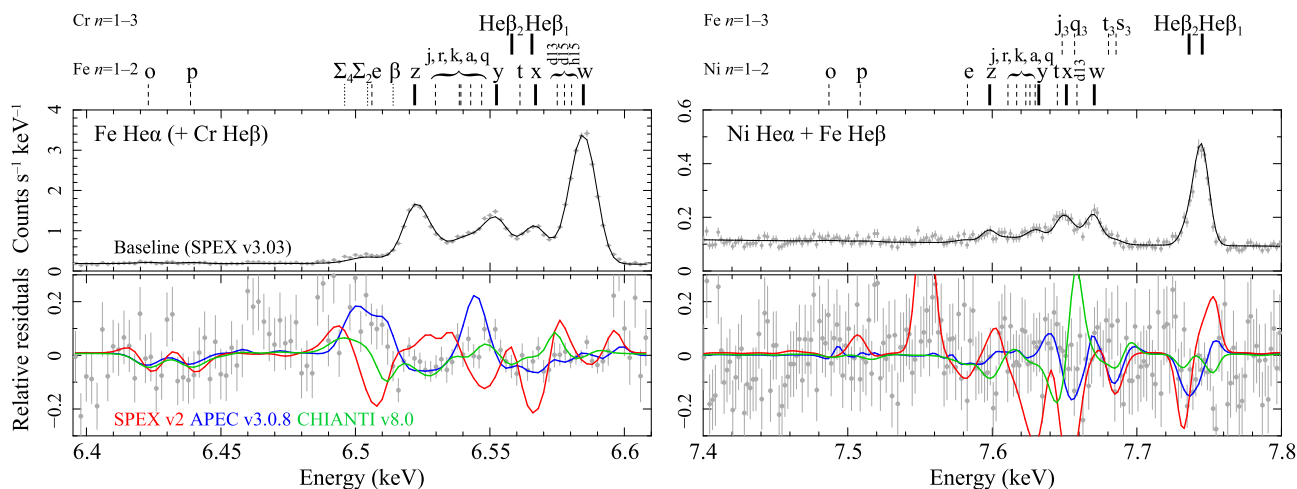


Fig. 1. Hitomi SXS spectrum in the Fe (left) and Ni (right) He α bands with the best-fit baseline model in the upper panels, and the residuals in the lower panels. Also in the lower panels are shown the relative differences between the baseline model and the best-fit models with various other plasma codes (SPEX v2 in red, APEC v3.0.8 in blue, and CHIANTI v8.0 in green). The solid bars above the upper panels show the energies of the main He α and He β lines, while the dashed and dotted ones are respectively of the Li-like and Be-like satellite lines. For the full-band results and line notations see appendices 4 and 5, respectively. (Color online)

4 Systematic factors affecting the derived source parameters: Plasma code

In this paper we consider SPEX version 3.03 (the baseline plasma model), as well as the old SPEX version 2/*Mekal* plasma model, the latest SPEX version before the launch of Hitomi (hereafter, the pre-launch version: SPEX version 3.00), as well as the pre-launch and the latest APEC/AtomDB versions 3.0.2 and 3.0.8 (Smith et al. 2001; Foster et al. 2012), respectively, CHIANTI version 8.0 (Dere et al. 1997; Del Zanna et al. 2015), and Cloudy version 13.04 (Ferland et al. 2013) plasma models. The best-fit models with these codes highlighting the Fe and Ni He α bands are compared in figure 1. The full-band results as well as the relevant atomic data are compared between these codes in appendices 4 and 5 (see also subsection 4.2).

4.1 SPEX versions 3.00 and 3.03

Version 3.00 of SPEX was released on 2016 January 29 as the pre-launch version for Hitomi data analysis. In SPEX version 2, line powers were calculated using the method of Mewe, Gronenschild, and van den Ord (1985), i.e., using a temperature-dependent parametrization of the line fluxes with empirical density corrections. Version 3.00 contains fully updated atomic data for the most highly ionized ions, solving directly the balance equations for the ion energy level populations and incorporating effects like density and radiation field, and uses these level populations to calculate the line power.

Triggered by the early work on the Hitomi SXS data of the Perseus cluster (Hitomi Collaboration 2016), and the

follow-up work as presented in this paper, several updates to version 3.00 were made leading to SPEX version 3.03, released in 2016 November, which is used for the present analysis. Below we list the most important updates for the present work relative to version 3.00.

- For Li-like ions, inner-shell transitions were extended from maximum principal quantum number $n = 6$ to $n = 15$ using the Flexible Atomic Code (FAC: Gu 2008) calculations.
- A numerical issue with Be-like ions related to metastable levels was resolved, allowing the full use of the new line calculations for these ions.
- Inner-shell energy levels, Auger rates, and radiative transitions for O-like Fe XIX to Be-like Fe XXIII were added using Palmeri et al. (2003a).
- A bug in the calculation of trielectronic recombination for Li-like ions was also removed; in the dielectronic capture from the He-like $1s2s$ level to Li-like $2s2p^2$ levels the relative population of the $1s2s$ level was ignored, leading to too high a population of these Li-like levels and subsequently to too strong stabilizing radiative transitions from these levels, and not in agreement with the Hitomi SXS data.
- The proper branching ratios for excitation and inner-shell ionization to excited levels that can auto-ionize are now taken into account, leading to improvements for some satellite lines.

To demonstrate the post-launch updates, we present the results of the Hitomi SXS spectral fitting with both versions 3.00 and 3.03 in table 1. The best-fit C-statistic value increases by 2372 from versions 3.03 to 3.00, and the

latter gives a 7% higher temperature, 8% higher turbulent velocity, and 30% lower Fe abundance than the former one. The other abundances also have 3% to 37% deviations. The effective column density of resonance scattering $N_{\text{H,hot}}$ becomes zero with version 3.00.

4.2 Using SPEX version 2 (the Mekal code)

The old *Mekal* code, or SPEX version 2 (Mewe et al. 1995), contained significantly fewer lines and chemical elements than the present version of SPEX. In addition, the atomic data (e.g., line energies) have been improved in the present SPEX version compared to the old *Mekal* model. This is evident from table 1, showing that the best-fit C-statistic value increases by 1125 if we replace the new code by the old code. A detailed comparison (figures 23–25 in appendix 4) shows that there are many differences. For instance, contrary to the old model, the new model includes Cr and Mn lines (in the 5–6 keV range). Also, updates in the line energies are visible as a sharp negative residual close to a sharp positive residual.

The old code yields almost the same temperature as the new code, but there are significant changes in the derived turbulent velocity and in the abundances. Small wavelength errors can be compensated for by adjusting the line broadening. Abundances are off by $2\text{--}4\sigma$ or up to 5%–15% of the values obtained from the baseline model.

This is only one example of a comparison between different models. In appendix 4 (figures 23–25), we show the full Hitomi SXS spectrum in 1.9–9.5 keV with our best-fit baseline model in the upper panels, and the residuals in the lower panels. In these lower panels we also show the relative differences between the baseline model and the best-fit models obtained with various other plasma codes.

The differences between these models can be divided into two classes: wavelength differences (leading to a positive residual next to a negative residual, e.g., the Ca XIX He β line near 4.51 keV has a different wavelength in the *Mekal* code compared to the baseline model), or flux differences (leading to a strict positive or negative residual in the relative residuals, e.g., the S XV forbidden line near 2.38 keV is stronger in the *Mekal* model compared to the baseline model).

In appendix 5 (tables 10 and 11) we list the line energies of the strongest lines in the spectrum. For comparison, the energies in SPEX are shown together with those in the APEC version 3.0.8 and CHIANTI version 8.0 codes. All the Lyman- and helium-series transitions with model line emissivities $\geq 10^{-26}$ photon $\text{m}^3 \text{s}^{-1}$ are listed, and for satellite lines of He-like, Li-like, and Be-like ions, the threshold is set to 10^{-25} photon $\text{m}^3 \text{s}^{-1}$. In addition, we show the Einstein coefficients and emissivities used in the three atomic codes.

4.3 APEC

APEC runs were conducted for both the pre-launch version, AtomDB version 3.0.2, and the latest version, AtomDB version 3.0.8. Since the launch of Hitomi, several updates have been made to the database to reflect the needs of the Hitomi data. These updates were not made to “fit” the Hitomi SXS data, but instead to reflect the priorities that analysis revealed. These changes were:

- The ionization and recombination rate calculation was switched from an interpolatable grid to a fit function, which has a few percent effect on several ion populations depending on the temperatures/ion involved.
- Wavelengths for higher- n transitions of the H- and He-like ions were changed to match Ritz values from the NIST Atomic Spectra Database.
- Wavelengths for valence shell transitions of Li-like ions were changed to match Ritz values from NIST.
- Fluorescence yields and wavelengths of inner shell lines were updated to the data of Palmeri et al. (2003a, 2003b, 2008, 2010, 2012) and Mendoza et al. (2004).
- Collisional excitation rates for He-like Fe were changed from an unpublished data set to that of Whiteford et al. (2001).
- Collisional excitation rates for H-like ions from Al to Ni were changed from FAC calculations to those of Li et al. (2015).

The spectral calculation is done with the *bvvapec* model in Xspec version 12.9.1 (Arnaud 1996), while the rebinning and fitting are carried out with SPEX version 3.03.00. The abundance standard (Lodders & Palme 2009) is applied to the APEC calculations. This allows a direct comparison between APEC and SPEX. The ionization balance calculation in APEC, on the other hand, is based on Bryans, Landi, and Savin (2009, hereafter B09), while U17 is used in SPEX. This difference is separately discussed in subsection 5.4.

The run with the pre-launch APEC version 3.0.2 gives a best-fit C-statistic which is larger than the baseline value by 670.

As shown in figure 1 and appendix 4 (figures 23–25), the relative difference between SPEX and APEC is usually within 10%, except for a few lines, including Cr XXIII He α , Mn XXIV He α , Fe XXIV satellite lines at 6.42 keV, 6.44 keV, 8.03 keV, and 8.04 keV, Ni XXVII He α blended with Ni XXVI and Fe XXIV satellite lines, and Fe XXV He β to He η lines. Many differences might be related to the rates used in level population calculation, e.g., collisional excitation and spontaneous emission rates (see section 5 for details). The line energy data in APEC version 3.0.8 are in general in good agreement with SPEX version 3.03 (see table 10 in appendix 5 for details).

As listed in table 1, the APEC code gives a similar best-fit temperature to the SPEX baseline model. The metal abundances obtained with APEC are lower by 5%–10% for Si, S, Ar, Ca, and Ni than the best-fit baseline values, while the Cr abundances obtained with the two codes agree within error bars. The largest difference is with the Fe abundance, which is 16% lower in the latest APEC/AtomDB (version 3.0.8) than SPEX. The best-fit turbulent velocity in σ_v (LOS dispersion) derived with the latest APEC code is 16 km s^{-1} lower than the SPEX result.

4.4 CHIANTI

Another atomic code/database widely used in the UV and X-ray spectroscopy for optically thin, collisionally dominated plasma is the CHIANTI code. Compared to the APEC and SPEX codes, CHIANTI is more focused on modeling the spectra from relatively cooler plasma in the solar and stellar atmosphere, while in this work we are testing it in the conditions of hot ICM emission. The latest version, 8.0 (Dere et al. 1997; Del Zanna et al. 2015), is used. The current CHIANTI database includes all the relevant H-like and He-like ions except for Cr and Mn, which means that these abundances cannot be estimated. We calculate the CIE spectrum using an IDL-version *isothermal* model, setting the ionization balance to B09, and change the solar abundance table to Lodders and Palme (2009) proto-solar values. To perform the fit to the data, the IDL calculation is implemented as an input to the *user* model in SPEX, and the fitting engine of SPEX repeatedly triggers the IDL run until a best fit is reached. Since the CHIANTI code does not provide line broadening information, we apply a multiplicative SPEX Gaussian broadening model *vgau* to the CHIANTI model. This is only a first-order approximation, since the thermal broadening should vary with the atomic number. A detailed comparison of the best-fit spectra shown in appendix 4 (figures 23–25) reveals several differences in emission features from the baseline model, at levels ranging from a few percent up to about 20%. Most of these differences are traced back to the different input atomic data, which can be found in appendix 5 (tables 10–11).

The C-statistic value increases by 327 when fitting with the CHIANTI code. The best-fit temperature, emission measure, turbulent velocity, and Fe abundance are roughly consistent with the baseline results, while the remaining abundances differ by 3%–19%. The required column density for resonance scattering is reduced by 10% with the CHIANTI model.

4.5 Cloudy

The Cloudy code has been developed as a tool to calculate photoionized plasmas, and it is principally used for

this application. It does, however, have a module for calculating CIE plasma spectra, so we have therefore fitted the Perseus spectrum with the coronal equilibrium model of Cloudy version 13.04. The abundance standard is set to Lodders and Palme (2009). Since the Cloudy code does not provide thermal and turbulent broadening, we again apply a multiplicative SPEX Gaussian broadening model *vgau* to the Cloudy calculations. As shown in table 1, the fit with Cloudy yields a large C-statistic. The most significant residuals appear at the Fe XXV He-series and Fe XXVI Ly α lines. The best-fit temperature agrees with the results of the other codes, but the abundance values differ strongly from those derived from the other codes. We again note that modeling of collisional plasmas is not Cloudy's main purpose.

5 Systematic factors affecting the derived source parameters: Atomic data

As shown in table 1, the atomic code uncertainty contributes the main uncertainty of many parameters, such as the Si, S, Ar, Ca, Mn, Fe, and Ni abundances, the hot absorption, and the turbulent velocity. The code uncertainty mainly comes from the input atomic data, for instance the ionization balance, collision excitation/de-excitation rates, recombination rates, and transition probabilities. In this section, we explore and describe the discrepancies between the current atomic data used in each code, and estimate the propagated errors on the fitted parameters.

5.1 Collisional excitation

5.1.1 H-like ions

In this section, we address the systematic uncertainties on the collisional excitation rates for H-like ions from the ground to the 2p levels. The radiative relaxation from the 2p levels back to the ground produces the Ly α lines. As shown in table 2, the effective collision strengths of Si XIV and Fe XXVI for a 4 keV plasma often differ by 10%–30% among atomic codes, which contributes an important uncertainty in the abundance measurement (table 1). The collision rates used in AtomDB version 3.0.2 and CHIANTI version 8.0 are systematically larger than those in SPEX version 3.03 and AtomDB version 3.0.8, while the latter two are roughly consistent with the calculations by FAC version 1.1.1, which can calculate both atomic structure and scattering data, and the relativistic effects are fully taken into account by the Dirac–Coulomb Hamiltonian. By solving the configuration-interaction wave functions in the Dirac–Fock–Slater central-field potential, it evaluates the radiative transitions and auto-ionization rates for the input atomic levels, and computes the effective collisional

Table 2. Electron effective collision strengths (10^{-3}) of the $\text{Ly}\alpha$ transitions for a CIE plasma at 4 keV temperature.

Ion	$\text{Ly}\alpha_1$ transition: $1s\ (^2S_{1/2})-2p\ (^2P_{3/2})$					Difference*
	SPEX v3.0.3	AtomDB v3.0.8	AtomDB v3.0.2	CHIANTI v8.0	FAC	
Si XIV	17.11	18.97	22.12	22.14	18.80	23%
S XVI	12.31	13.30	15.32	15.39	13.10	20%
Ar XVIII	9.29	9.74	11.07	8.08	9.59	27%
Ca XX	7.25	7.40	8.25	8.08	7.27	14%
Cr XXIV	4.61	4.68	5.00	—	4.56	11%
Mn XXV	4.17	4.24	4.47	—	4.12	10%
Fe XXVI	3.51	3.85	3.76	3.71	3.74	9%
Ni XXVIII	3.18	3.21	3.27	3.28	3.12	7%

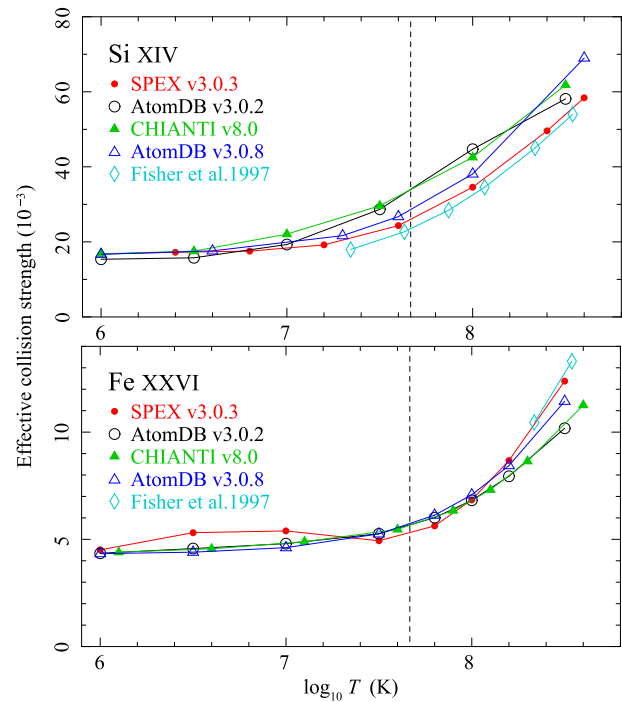
Ion	$\text{Ly}\alpha_2$ transition: $1s\ (^2S_{1/2})-2p\ (^2P_{1/2})$					Difference*
	SPEX v3.0.3	AtomDB v3.0.8	AtomDB v3.0.2	CHIANTI v8.0	FAC	
Si XIV	8.55	9.54	11.15	11.05	9.48	23%
S XVI	6.15	6.68	7.75	7.68	6.63	21%
Ar XVIII	4.64	4.92	5.62	4.57	4.86	19%
Ca XX	3.62	3.74	4.20	4.03	3.71	16%
Cr XXIV	2.30	2.38	2.57	—	2.34	13%
Mn XXV	2.09	2.16	2.31	—	2.13	13%
Fe XXVI	1.66	1.97	1.90	1.89	1.93	16%
Ni XXVIII	1.59	1.65	1.70	1.64	1.62	10%

*Relative differences between the codes defined as (maximum – minimum)/maximum.

strengths using a distorted-wave approximation. The FAC values shown are based on calculations with a default grid that contains six grid points. As a check, a calculation with a grid of 11 points has also been carried out. The values with the 11-point grid are about 5% lower than the values of the default grid calculation. Consistency between FAC and AtomDB version 3.0.8 is expected, since the AtomDB values are essentially taken from a FAC calculation by Li et al. (2015).

The differences in the effective collision strengths depend on the electron temperature. In figure 2, we compare five sets of calculations for Si XIV and Fe XXVI $\text{Ly}\alpha$ transitions. For Si XIV, SPEX uses an R-matrix calculation by Aggarwal and Kingston (1992), which is roughly consistent with the AtomDB and CHIANTI values within 8% at 10^6 K, but becomes lower by 30% at $10^{7.7}$ K than the CHIANTI data. This means that even for the simplest H-like ions, the atomic data for the collision process are not sufficiently converged to match the accuracy of the current observations. Since the Si abundance is mostly determined by the Si XIV $\text{Ly}\alpha$ for the Hitomi SXS data, the 30% uncertainty in the collision strength calculation indicates a roughly similar error in the abundance measurement.

For Fe XXVI, we compare two representative calculations using an R-matrix method, Ballance, Badnell, and Berrington (2002)—implemented in CHIANTI version 8.0

**Fig. 2.** Comparisons of effective collision strength as a function of balance temperature. The $\text{Ly}\alpha_1$ and $\text{Ly}\alpha_2$ transitions are combined. The vertical dashed lines mark a temperature of 4 keV. (Color online)

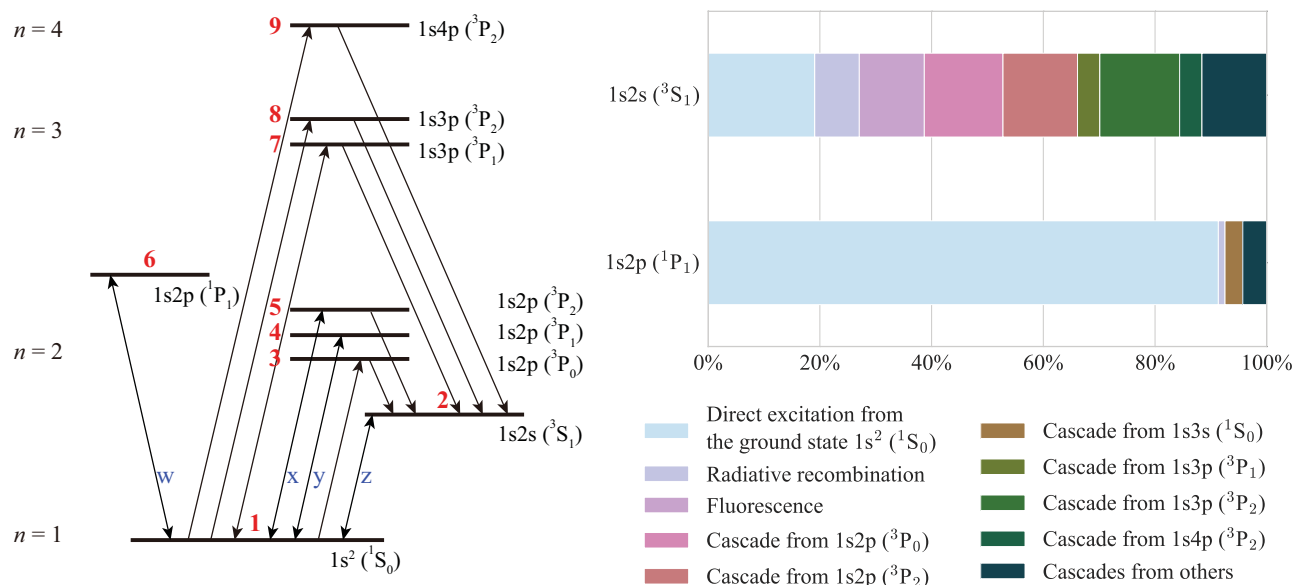


Fig. 3. Left: Grotrian diagram of the dominant Fe xxv levels to the triplet formation. The red numbers are used in table 3. The blue labels show transitions corresponding to the individual lines of the triplet. The 1s2s (1S₀) level is not shown here, as it does not contribute to line production but to continuum emission via two-photon decay (e.g., Nussbaumer & Schmutz 1984). Right: Relative contributions to the formations of 1s2s (3S₁) and 1s2p (1P₁) levels (upper levels of z and w, respectively). (Color online)

and AtomDB version 3.0.2—and Kisielius, Berrington, and Norrington (1996), used in SPEX version 3.03, and the FAC calculation in AtomDB version 3.0.8. The three results roughly agree with each other at 10⁶ K, while the calculations of Kisielius, Berrington, and Norrington (1996) are higher than the other two up to 10⁷ K, and decrease rapidly beyond this temperature, relative to the others. At the high temperature end (3×10^8 K), the difference between the Ballance, Badnell, and Berrington (2002) and Kisielius, Berrington, and Norrington (1996) values is about 30% for the 1s (2S_{1/2})–2p (2P_{3/2}) Ly α ₁ transition. According to Ballance, Badnell, and Berrington (2002), the differences at low and high energies are mainly caused by the treatment of radiation damping and by the high-energy approximation, respectively. This would contribute to a minor part of the uncertainty on the Fe abundance measured with the Hitomi SXS data; the main uncertainty comes from the He α transitions (sub-subsection 5.1.2).

5.1.2 He-like ions

We now turn to the He-like Fe-K multiplet as a test case to assess the flux errors on model lines by the input atomic data. First we define the range of related atomic levels and data in figure 3 and table 3. The most dominant populating process for the upper levels of the resonance and intercombination transitions is electron-impact excitation from the ground state, and the main loss process is radiative transition back to the ground state. The upper level of the x line

(2p 3P₂) has an 18% chance to form a two-step decay via an intermediate level.

Meanwhile, for a 4 keV plasma, the upper level of the Fe xxv forbidden transition (z) is populated almost equally: by excitation from the ground state; by cascades from the 2p (3P₀), 2p (3P₂), and 3p (3P₂) levels; and by radiative recombination from the continuum state. In addition, inner-shell ionization of Fe xxiv drives 8%, and radiative transitions from the 3p (3P₁) and 4p (3P₂) levels both provide 4% of the population. The metastable level can decay to the ground only via radiative transitions.

We compare the atomic data extracted from the SPEX, AtomDB, and CHIANTI databases, as well as the collision data from the Open-ADAS database,³ and the radiative transition data from the FAC calculation. The effective collision strengths used in SPEX, AtomDB version 3.0.2 and CHIANTI version 8.0, and AtomDB version 3.0.8 are taken from the published data in Zhang and Sampson (1987, distorted wave), A. D. Whiteford (2005,⁴ R-matrix), and Whiteford et al. (2001, R-matrix), respectively. The data from Open-ADAS is calculated with the distorted-wave approximation. We do not show the FAC results on the collisional excitation, since it does not explicitly provide the contributions from resonance excitation channels, which are incorporated in the other calculations.

³ ADF04, produced by Alessandra Giunta, 2012 September 14. See (<http://open.adas.ac.uk>).

⁴ Whiteford, A. D. 2005, ADF04 data set in the OPEN-ADAS database.

Table 3. Fe XXV He α multiplet formation for a CIE plasma at 4 keV temperature.

Transition*	Rel. contrib. [†]	Electron effective collision strength (10^{-3})					Difference [‡]
		SPEX v3.03	AtomDB v3.0.8	AtomDB v3.0.2	CHIANTI v8.0	Open-ADAS	
1 \rightarrow 2	19%	0.268	0.295	0.410	0.425	0.246	42%
1 \rightarrow 3	69%	0.138	0.143	0.144	0.146	0.135	8%
1 \rightarrow 4	77%	0.715	0.721	0.728	0.721	0.868	18%
1 \rightarrow 5	67%	0.692	0.703	0.714	0.740	0.695	6%
1 \rightarrow 6	91%	4.047	4.026	4.051	4.004	4.316	7%
1 \rightarrow 7	71%	0.161	0.163	0.162	0.162	0.166	3%
1 \rightarrow 8	63%	0.173	0.178	0.180	0.182	0.165	9%
1 \rightarrow 9	62%	0.071	0.069	0.071	0.072	0.073	5%

Transition*	Rel. contrib. [†]	Transition probability (s^{-1})					Difference [‡]
		SPEX v3.03	AtomDB v3.0.8	AtomDB v3.0.2	CHIANTI v8.0	FAC	
2 \rightarrow 1 (z)	100%	2.080×10^8	1.930×10^8	left	2.080×10^8	1.997×10^8	7%
4 \rightarrow 1 (y)	100%	4.260×10^{13}	3.720×10^{13}	left	4.350×10^{13}	4.196×10^{13}	14%
5 \rightarrow 1 (x)	82%	6.550×10^9	6.578×10^9	6.519×10^9	6.480×10^9	6.568×10^9	1%
6 \rightarrow 1 (w)	100%	4.565×10^{14}	4.670×10^{14}	left	4.610×10^{14}	4.679×10^{14}	2%
7 \rightarrow 1	63%	1.524×10^{13}	1.060×10^{13}	left	1.126×10^{13}	1.248×10^{13}	30%
3 \rightarrow 2	100%	3.820×10^8	2.770×10^8	left	3.740×10^8	3.743×10^8	27%
5 \rightarrow 2	18%	1.470×10^9	1.420×10^9	left	1.420×10^9	1.466×10^9	3%
7 \rightarrow 2	34%	8.078×10^{12}	7.990×10^{12}	left	7.861×10^{12}	8.057×10^{12}	3%
8 \rightarrow 2	100%	8.932×10^{12}	8.550×10^{12}	left	8.682×10^{12}	8.660×10^{12}	4%
9 \rightarrow 2	74%	3.957×10^{12}	3.550×10^{12}	left	3.642×10^{12}	3.769×10^{12}	10%

*Energy-level IDs correspond to the energy levels as denoted in figure 3.

[†]Relative contributions to the total gain or loss term of the level derived with SPEX v3.03.

[‡]Relative differences between the codes defined as (maximum–minimum)/maximum.

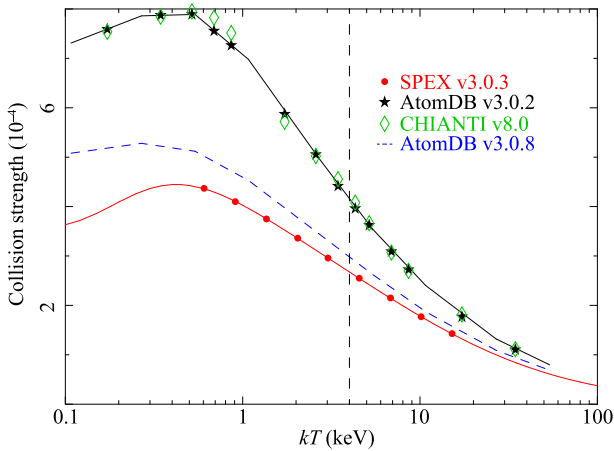


Fig. 4. Comparison of the effective collision strength from the ground to 1s.2s (3S_1) state. The vertical line shows a temperature of 4 keV. (Color online)

As shown in table 3, the collision data converge relatively well ($<18\%$) on the ground to 1P - and 3P -level transitions, but differ by up to 42% on the ground to 3S transition. As shown in figure 4, the effective collision strengths used in CHIANTI version 8.0/AtomDB version 3.0.2 are systematically larger than in SPEX version 3.03, by a factor of two at

1 keV and by about 40% at 10 keV. The values in AtomDB version 3.0.8 lie in the middle, about 10% higher than the SPEX values at 4 keV. It appears that the R-matrix calculations (AtomDB and CHIANTI) are systematically higher, by 10%–40%, than the distorted-wave calculations (SPEX and Open-ADAS). Since the forbidden transition from 3S to the ground gives a line intensity only second to the resonance line for a 4 keV plasma, while the latter is subject to resonance scattering (subsection 8.1), the uncertainty of the 3S excitation should contribute to a significant portion of the total error of the Fe abundance. The radiative transition data used in different codes agree within a 15% level for the He-like triplet lines. The transition rates from higher levels (e.g., $n = 3$ and 4) to the ground can have larger uncertainties up to 30%, which is discussed in more detail in subsection 5.2.

Assuming that the deviations between different data give a rough measure of the atomic process uncertainties, we carry out a Monte Carlo simulation to quantify the atomic uncertainties on the He-like triplet line ratios. We generate 1000 sets of collisional excitation rates by randomizing based on the five sets of collision data in table 3. The same is done for the transition probability. Then we run

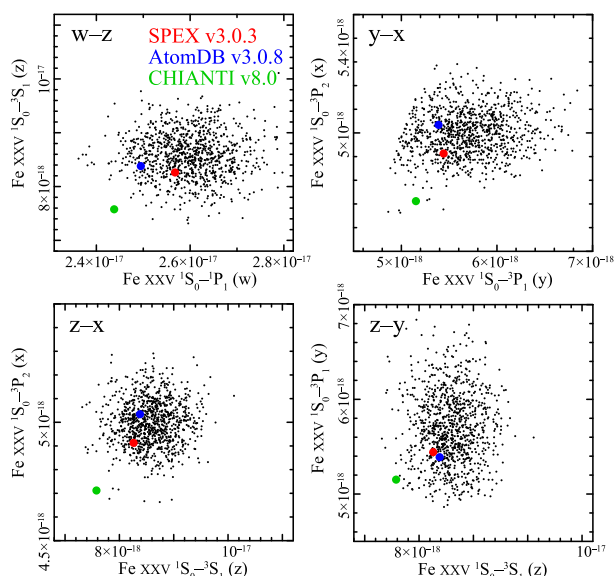


Fig. 5. Monte Carlo simulations on the four Fe xxv He α lines. The SPEX, AtomDB, and CHIANTI values are shown in red, blue, and green, respectively. The line intensities are given in units of photons cm² s⁻¹. (Color online)

the SPEX calculation repeatedly, each time with one set of randomized collision and radiative data, to determine the flux error on each individual line. There are two potential caveats: first, the Monte Carlo method assumes that all the rate errors are independent, which is not always true for the atomic calculations; second, the differences between SPEX and other codes on the atomic data of the recombination processes and the fluorescent yields, as well as those on the atomic structure such as the maximum principal quantum number, are not taken into account in the simulation. Therefore the error obtained in the simulation should be regarded as a lower limit.

The results of the 1000 simulations are shown in figure 5. The simulation predicts that the resonance (w), intercombination (x and y), and the forbidden (z) lines have uncertainties of $\sim 4\%$, 2% and 8% , and 6% , respectively. The y and z lines have larger atomic uncertainties than the other two, probably caused by the relatively large errors of the collision strengths and the complex formation of the 3P and 3S levels. The actual AtomDB version 3.0.8 and SPEX version 3.03 line intensities indicate similar uncertainties. The CHIANTI version 8.0 triplet line fluxes are systematically lower than the simulation results and the other two codes. This could be caused by the fact that CHIANTI has the lowest maximum principal quantum number, and hence possibly the lowest radiative decay contribution to the $n = 2$ levels, among the three atomic codes. When multiplying the CHIANTI fluxes by a factor of 1.05, they become well on a line with the simulation results.

5.1.3 Best fit with adjusted line ratios for the x and y lines

We have further tested the sensitivity of our results on the He-like Fe lines as follows. We made the intensity of the x and y lines relative to the forbidden line a free parameter. Technically, this was achieved by applying two line components to the x and y line. This model produces the transmission $T(E)$ in our case for an absorption or emission line as $T(E) = \exp[-\tau_0\phi(E)]$, with the Gaussian optical depth profile, $\phi(E)$. We have frozen the line energy of this absorption line to the energies of the x and y lines, respectively, and the width to the width of the emission line (using the best-fit thermal and turbulent broadening from the baseline model). Thus, the only two additional free parameters are the nominal optical depths τ_0 of both lines, positive values indicating lower flux, negative values higher flux. The best-fit parameters are $\tau_0 = 0.035 \pm 0.028$ for x and $\tau_0 = -0.068 \pm 0.025$ for y. From this we derive that for the best-fit model the flux of the x line should be lower by $3\% \pm 3\%$ and that of y should be higher by $8\% \pm 3\%$ compared to our SPEX plasma model in order to give the best agreement with the observed spectrum (table 1).

The atomic uncertainties on the x, y, and z lines are calculated using a Monte Carlo simulation in subsection 5.1.2. Based on the simulated data, we further estimate that the errors on the x and y lines relative to the forbidden line ratios are 6.2% and 9.2% , respectively. Hence the best-fit modifications to the x and y lines are well on a line with the expected atomic errors.

5.2 Transition probability

Alongside of the radiative transition data for the He-like triplet shown above, here we make a more systematic comparison of the transition probabilities among the atomic codes. The radiative data for selected strong lines are shown in appendix 5 (table 10). In figures 6 and 7, we demonstrate that the Einstein A values for H-like ions are consistent within a few percent among the codes, while for He-like ions, especially for transitions from $n = 3$ or more to the ground, the A values have larger uncertainties, up to 30% . The SPEX A values are systematically higher than those in AtomDB and CHIANTI. Partly owing to the difference in the transition data, the He β , He γ , and He δ line intensities calculated by SPEX are higher than the AtomDB and CHIANTI lines (see the details in table 10). These lines contribute to a minor role in the abundance measurements.

5.3 Satellite line emission

The line energies, radiative transitions, and emissions of the satellite lines for a 4 keV CIE plasma are compared in table 11 of appendix 5. The atomic-level-dependent Auger

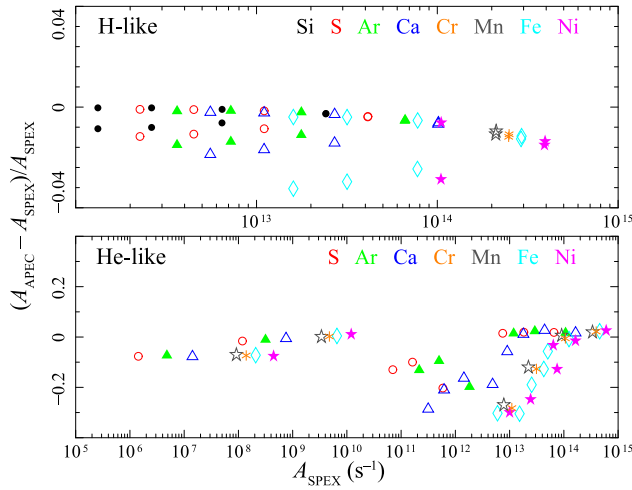


Fig. 6. Differences of Einstein A values of the strongest transitions (table 10) in SPEX v3.03 and AtomDB v3.0.8 for the H-like (upper) and He-like (lower) ions. The upper states are in the range of $n = 2-5$ for H-like and 2-4 for He-like ions. (Color online)

transition rates and radiative-to-total branching ratios are given in table 4, and the resulting line spectra for Fe are plotted in figure 8. The most noticeable issue is that APEC version 3.0.8 gives higher Fe XXIV fluxes at ~ 6.5 keV and 6.545 keV than the other two codes, driven by a recent update of APEC which incorporated the dielectronic recombination (DR) rates and branching ratios calculated in Palmeri et al. (2003a). This could partially explain the different Fe abundances with SPEX and APEC as shown in table 1.

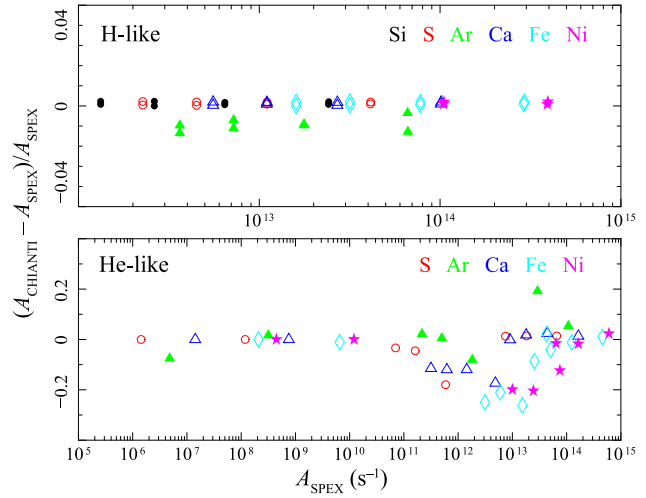


Fig. 7. Same as figure 6, but for comparisons between SPEX v3.03 and CHIANTI v8.0. (Color online)

5.4 Ionization equilibrium concentrations

Figure 9 shows relative ionic fractions of a 4 keV CIE plasma based on the SPEX and APEC calculations. In SPEX the ionization balance mode was set to U17, which allows the inclusion of inner-shell ionization contributions to the spectrum, while in APEC the balance from B09 was assumed. For He-like, H-like, and bare ions of Si-Cu, these two calculations agree with each other within 5%. For Li-like ions, they agree within 10%. For higher sequences, however, larger differences are seen as the APEC values are systematically larger, by up to 57%, than the SPEX values.

Table 4. Energies, Auger transition rates, and branching ratios of Fe XXIV.

Level	Energy*	Auger transition rate (s^{-1})		Branching ratio for radiative transition	
		SPEX v3.03	AtomDB v3.0.8	SPEX v3.03	AtomDB v3.0.8
1s.2s ²² S _{1/2}	6.60040	1.46×10^{14}	1.43×10^{14}	0.12	0.12
1s.2s.(³ S).2p ⁴ P _{1/2}	6.61369	7.79×10^{10}	1.33×10^{10}	0.98	1.00
1s.2s.(³ S).2p ⁴ P _{3/2}	6.61666	7.23×10^{11}	3.91×10^{11}	0.96	0.98
1s.2s.(³ S).2p ⁴ P _{5/2}	6.62781	3.53×10^4	1.97×10^9	1.00	0.76
1s.2s.(¹ S).2p ² P _{1/2}	6.65348	3.89×10^{13}	4.24×10^{13}	0.89	0.88
1s.2s.(³ S).2p ² P _{3/2}	6.66194	5.70×10^8	1.41×10^{11}	1.00	1.00
1s.2p ² ⁴ P _{1/2}	6.67097	2.41×10^{11}	3.37×10^{11}	0.99	0.99
1s.2s.(³ S).2p ² P _{1/2}	6.67644	8.18×10^{13}	6.77×10^{13}	0.69	0.73
1s.2s.(¹ S).2p ² P _{3/2}	6.67915	1.10×10^{14}	1.07×10^{14}	0.01	0.04
1s.2p ² ⁴ P _{3/2}	6.67928	8.46×10^{11}	9.66×10^{11}	0.92	0.92
1s.2p ² ⁴ P _{5/2}	6.68498	2.27×10^{13}	2.61×10^{13}	0.60	0.58
1s.2p ² ² D _{3/2}	6.70268	1.29×10^{14}	1.25×10^{14}	0.74	0.74
1s.2p ² ² P _{1/2}	6.70458	9.93×10^{11}	9.39×10^{11}	1.00	1.00
1s.2p ² ² D _{5/2}	6.70902	1.39×10^{14}	1.37×10^{14}	0.60	0.6
1s.2p ² ² D _{3/2}	6.72236	3.48×10^{13}	3.28×10^{13}	0.95	0.95
1s.2p ² ² S _{1/2}	6.74147	2.53×10^{13}	2.92×10^{13}	0.91	0.9

*Energy levels above the ground state in SPEX v3.03.

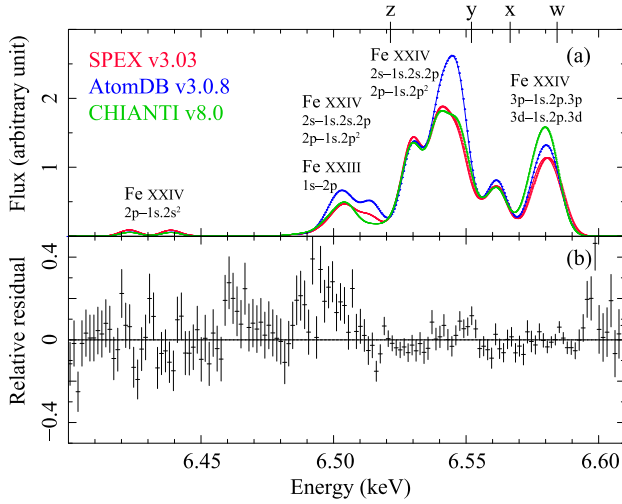


Fig. 8. (a) Li-like Fe XXIV and Be-like Fe XXIII lines of a 4 keV CIE plasma in the 6.4–6.61 keV band. The observed line broadening is taken into account. (b) Residual of the Hitomi SXS spectrum to the baseline fit in the same band. (Color online)

Here we assess the uncertainties on ionization concentration by replacing the baseline U17 balance with historical ones, namely Arnaud and Rothenflug (1985, hereafter AR85), Arnaud and Raymond (1992, hereafter AR92),⁵ and B09. It should be noted that the AR85 and AR92 balances do not include trace elements, such as Cr and Mn. As shown in table 1, the baseline model with the AR85 and AR92 ionization balances becomes much worse by δC_{stat} of about 100, and the best-fit temperature and abundances change by 1%–3%. The B09 balance provides an equally good fit to the U17 one, yielding almost the same parameters except for the Fe abundance, which increases by 4%. The N_{H} of the self-absorption component changes by 6%–13% for different balances. By comparing the values from the mostly used B09 and U17 balances, the systematic uncertainty on abundances from ionization concentration is 1%–4%.

A related issue is the uncertainty on the ratio of He-like ion to H-like ion. As shown in appendix 4 (figures 23–25), the He- and Ly-series are the dominant line features of the Perseus spectrum, and their ratios largely determine the temperature measurement. Here we examine the He-like to H-like ion ratios as a function of nuclear charge Z , which is expected in theory to be a perfectly smooth function. The calculation is based on SPEX version 3.03. As shown in figure 10, the He-like to H-like ion ratio indeed appears as a nearly linear function in logarithmic space, and the scatter is within 0.5%.

⁵ Because AR92 reported updates only on the Fe ionization concentration, the calculations of AR85 are utilized for the other elements.

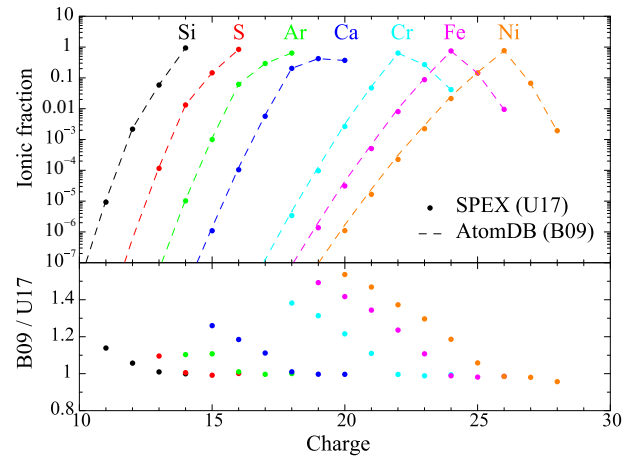


Fig. 9. Upper: Ionic fraction of a 4 keV CIE plasma in SPEX v3.03 (U17: dots) and APEC v3.0.8 (B09: curves). Lower: Ratios between the two. (Color online)

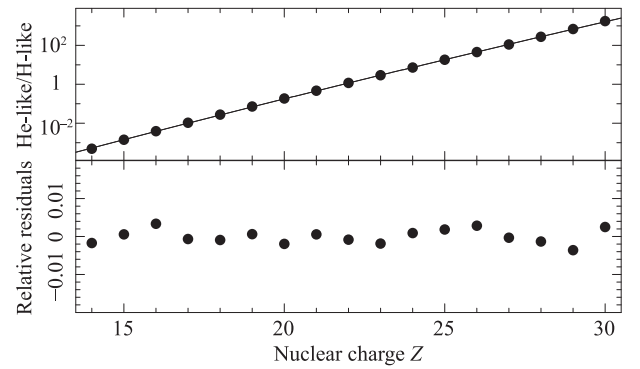


Fig. 10. Upper: He-like to H-like ion ratio as a function of nuclear charge Z for a 4 keV plasma. The solid line shows a polynomial fit in logarithmic space. Lower: Relative residuals of a polynomial fit. (Color online)

6 Systematic factors affecting the derived source parameters: Plasma modeling

Although it is in principle straightforward to calculate a spectrum from the atomic data, practically these calculations are based on a range of approximations, and usually include only limited physical processes—treatment of specific physical processes is limited or missing entirely. This section explores these technical issues in the plasma modeling and discusses their impacts on the fitted parameters.

6.1 Voigt profiles

In our baseline model we have approximated the line profiles using Doppler profiles (Gaussians). This gives a significant increase in speed in obtaining our spectral fits. However, the true profiles are Voigt profiles. We have tested the sensitivity of our results to these intrinsic line profile assumptions. The Lorentzian widths of the Voigt profiles are fixed to the natural widths in SPEX version

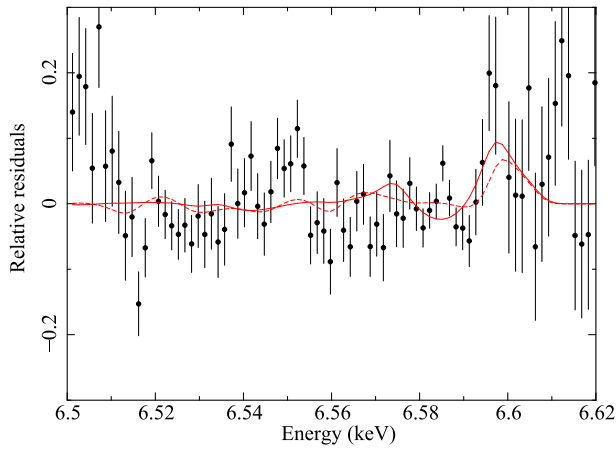


Fig. 11. Residuals of the baseline model near the He-like 1s–2p transitions. The dotted curve shows the predicted model change when instead of Doppler profiles Voigt profiles are chosen, but without altering the parameters of the baseline model. The solid curve shows the same but after refitting the spectrum. (Color online)

3.03. Figure 11 shows our results. The changes are substantial (5%–10%) near the Fe XXV resonance line observed at 6.60 keV. In all other parts of the spectrum the changes are smaller, due to the fact that the lines are weaker.

6.2 Continuum contributions from heavy elements

It is not only abundant elements like H, He, O, and Fe that contribute significantly to the continuum emission; the contributions of less abundant elements like Cr or Mn are also detectable. We discovered this by accident when we tested our baseline model with the old version of SPEX (version 2). In that old version only the most abundant 15 elements with a nuclear charge less than 30 were taken into account in the line emission, yet the model could produce some very crude constraints on the Cr and Mn abundance, while the line emission of both elements was not accounted for by the model.

What is the explanation for this? In figure 12 we show the relative contribution of each element to the continuum emission (including here also the AGN continuum). About 90% of the emission is due to H and He, about 10% is due to Fe, and all other elements contribute less than a few percent at most. In particular, for the elements between Si and Mn clearly the smooth two-photon emission bumps and the free-bound edges are visible.

The present spectrum has 487621 counts with a nominal uncertainty of 698 counts. Cr and Mn contribute 78 and 104 counts to the continuum, respectively. Therefore their contribution is small, but if the abundances had been off by a factor of 10, their continuum contribution with their

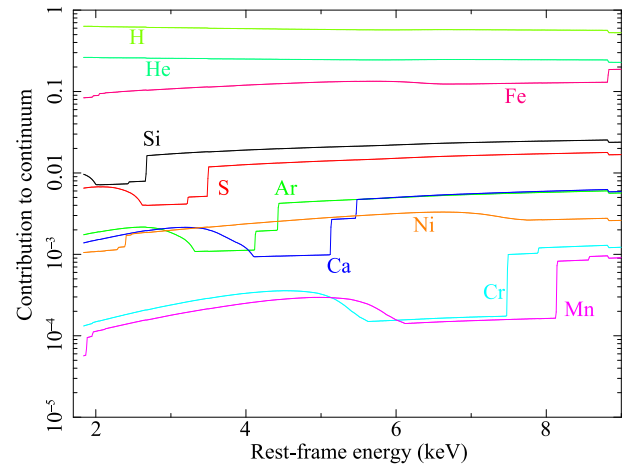


Fig. 12. Relative contribution of the different elements to the continuum emission of the main thermal component in the Perseus cluster. (Color online)

specific structure as shown in figure 12 would have allowed us to constrain their abundances.

In SPEX, all contributions to the radiative recombination (free-bound) continuum smaller than a threshold are omitted for computational efficiency (the free-bound continuum calculation takes most of the computing time for high-resolution spectra because of the large number of energy bins and atomic shells that need to be calculated). The threshold is controlled by the parameter “gacc” that can be set by the user. Its default value is 10^{-3} , but for figure 12 we have set it to 10^{-7} .

This same value is used in the entry g_{acc} listed in table 1. It can be seen that changing this parameter has only a very minor effect on the fit (improvement of C-statistic only 0.41), but the additional computational burden is heavy.

6.3 Maximum principal quantum number n in the calculations

Collisional excitation by thermal electrons mostly populates the inner shells of the atomic structure. Although the emission lines from outer shells are usually rather weak, some of them become visible in the Hitomi SXS spectrum (appendix 5; table 10). Here we test the impact on the obtained spectral parameters by limiting the maximum principal quantum number n in the calculation. As shown in table 1, when excluding the outer shells with $n > 5$, the fit with the baseline model gets poorer by $\delta C_{stat} \approx 61$, and the best-fit metal abundances become slightly larger by a few percent. This is because the outer shell population will also contribute to the inner shell (e.g., $Ly\alpha$, $Ly\beta$) transitions by radiative cascading. As shown in table 10, the Hitomi SXS data require the plasma code to calculate to at least $n = 10$ for the Fe XXV lines.

6.4 Hyperfine mediated transitions

The isotopic composition of Fe contains approximately 2% of ^{57}Fe , which has non-zero nuclear spin and thus might be expected to exhibit a hyperfine-mediated transition from $1s2p\ ^3P_0$ to ground, resulting in a weak third intercombination line. The transition rate has been calculated by Johnson, Cheng, and Plante (1997), who find that it is about 6% of the transition rate to the $1s2s\ ^3S_1$ state, so that the strength of the $1s2p\ ^3P_0$ transition to ground is negligible for Fe. The low branching ratio to ground can be attributed to the relatively weak magnetic moment of ^{57}Fe . We caution that all odd Z elements have non-zero nuclear magnetic moments, and for most of those ions in the Fe group, the hyperfinemediated decay channel to ground is actually dominant.

7 Systematic factors affecting the derived source parameters: Astrophysical model

The atomic data and plasma code are eventually integrated into the spectral models. To verify the spectral modeling with the Hitomi SXS data, it is important to test it in a proper astrophysical context. In this section, we incorporate several astrophysical effects, such as non-equilibrium and multi-temperature, examine their spectral features with the data, and calculate the related uncertainties on the fitted parameters. The physical implication of these effects will be discussed in other Hitomi Collaboration papers.

7.1 Ion temperature versus turbulence

The basic assumption made in our earlier paper on turbulence (Hitomi Collaboration 2016) is that the ion temperature of the cluster gas equals the electron temperature. Given the relatively high density in the core of the Perseus cluster ($\sim 0.05\text{ cm}^{-3}$; Zhuravleva et al. 2014) compared to the outskirts ($\sim 10^{-4}\text{ cm}^{-3}$; Urban et al. 2014), this assumption may be justified, but in other circumstances it may be different.

In order to test this, we have decoupled the ion temperature from the electron temperature in our model and refitted the spectrum. We get an insignificant improvement of our fit ($\delta C_{\text{stat}} = -0.02$), with the best-fit values of the ion temperature of $kT_{\text{ion}} = 4.1\text{ }(-2.3, +3.2)\text{ keV}$ and turbulent velocity $\sigma_v = 156\text{ }(-21, +13)\text{ km s}^{-1}$. However, there is a strong anti-correlation between both parameters. Without constraints on the ion temperature, σ_v can be anywhere between 134 and 168 km s^{-1} . The best-fit values of these parameters depend on details of the spectral analysis method, although the differences are smaller than the statistical errors. Such systematic effects are separately discussed

in the V paper. Note that for a fixed ion temperature, the uncertainty on the turbulent velocity is much smaller, i.e., only 3 km s^{-1} . We show the (minor) effects of a free ion temperature on the other parameters in table 1.

7.2 Deviations from collisional ionization equilibrium

The core of the Perseus cluster is a very dynamic environment, with a relatively high density and an active galactic nucleus at its center. Therefore, in principle one might expect non-equilibrium ionization (NEI) effects to play a role. We have tested this as follows.

The simplest test is to decouple the temperature used for the ionization balance calculations, T_{bal} , from the (electron) temperature T_{spec} used for the evaluation of the emitted spectrum for the set of ionic abundances obtained using T_{bal} . This can be achieved within the SPEX package by making the parameter $RT \equiv T_{\text{bal}}/T_{\text{spec}}$ a free parameter. We obtain a best fit for $RT = 0.980 \pm 0.011$, i.e., close to unity, with only a modest improvement in C-statistic of 3.26.

Alternatively, we can replace the basic CIE model by a genuine NEI model in SPEX. This model can mimic a plasma that suddenly changes its electron temperature from a value T_1 to a value T_2 . The spectrum is then evaluated after a time t , related to the measured relaxation timescale U by $U = \int n_e dt$, the electron density integrated over time from the instant that the temperature suddenly changes.

The first case we consider is an ionizing plasma $T_1 < T_2$ (labeled “Ionizing” in table 1), which has $T_1 = 1.5 \pm 0.4\text{ keV}$, $T_2 = 3.994 \pm 0.021\text{ keV}$, and $U = (1.4 \pm 0.3) \times 10^{18}\text{ m}^{-3}\text{ s}$. The ionizing plasma model improves the C-statistic by 5.46.

Further, we tested a recombining model by inverting the role of T_1 and T_2 (model labeled “Recombining”). Leaving T_1 free, it appears that it gets to a very high value. Therefore we choose to fix T_1 to a high value (100 keV), so we start essentially with a fully ionized plasma. We obtain $T_2 = 3.933 \pm 0.020\text{ keV}$, $U = (2.5 \pm 0.2) \times 10^{18}\text{ m}^{-3}\text{ s}$, and an improvement in C-statistic of 9.19.

The above may suggest that there are some significant, although minor, non-equilibrium effects. However, we cannot claim such effects here. First, nominally our fits are very close to equilibrium ($RT \approx 1$ or $U \approx 10^{19}\text{ m}^{-3}\text{ s}$). The best-fit value for RT may differ from unity at the 1.9σ confidence level, but the absolute difference is only 2.0%. It is likely true that the systematic uncertainties on the ionization and recombination rates are large enough to account for such a small deviation from equilibrium. For example, when we increase all ionization rates for iron ions arbitrarily by 5%, the peak concentration of Fe xxv for the baseline model would increase from 0.747 to 0.750; the lowering of

the temperature by 1% would have the same effect on the Fe XXV concentration.

Another issue is that introducing multi-temperature structure (subsection 7.4) gives much larger improvements to the fit. Clearly, the Perseus core region contains multiple-temperature components, and at such a level that weak non-equilibrium effects cannot be separated from it.

7.3 Effects of the spatial structure of the Perseus cluster

Up to now, we have treated the Perseus spectrum with relatively simple spectral models. In reality, Perseus shows temperature and abundance gradients. How do they affect our analysis? We investigate this through simulation. Our goal here is to estimate the systematic uncertainties on the derived parameters resulting from neglecting the spatial structure of Perseus.

We proceed as follows. We have taken the radial temperature and density profile derived from deprojected Chandra spectra as given by Zhuravleva et al. (2014, extended data figure 1). For the radial abundance profile we have adopted the average profile for a large sample of clusters based on XMM-Newton data (Mernier et al. 2016). We have not chosen their profile derived from the Perseus data alone, because that is noisier than the average profile for the full set of clusters. Mernier et al. (2016) show that in general the radial abundance profiles of individual clusters agree well with this average profile.

We have then integrated these three-dimensional profiles over the line of sight through the projected FOV of the Hitomi SXS for our present observations. We accounted for the different pointing position for Obs 2+3 compared to Obs 4 by weighting with the relative exposure times. In this way we have obtained the differential emission measure distribution (DEM) within the FOV of the Hitomi SXS. We have binned it in 0.1 keV-wide temperature bins. The total emission measure is $1.003 \times 10^{73} \text{ m}^{-3}$. Figure 13 shows this distribution (normalized to integral unity) as well as the average abundance for each temperature bin.

We see that the DEM is strongly peaked toward 3 keV, and decreases rapidly with higher temperatures. This peak corresponds to the coldest gas in the center of the cluster using the Zhuravleva et al. (2014) parameterization (we have assumed that the temperature remains constant for radii smaller than 10 kpc). The DEM then flattens near 5 keV and turns up again above 6.4 keV. This corresponds to the peak in the radial temperature distribution around 250 kpc. The abundance drops almost continuously from 0.82 in the center (at 3 keV) to 0.47 at 6.5 keV.

Thus, we are faced with an extremely skewed DEM distribution over a range of only a factor of two difference in

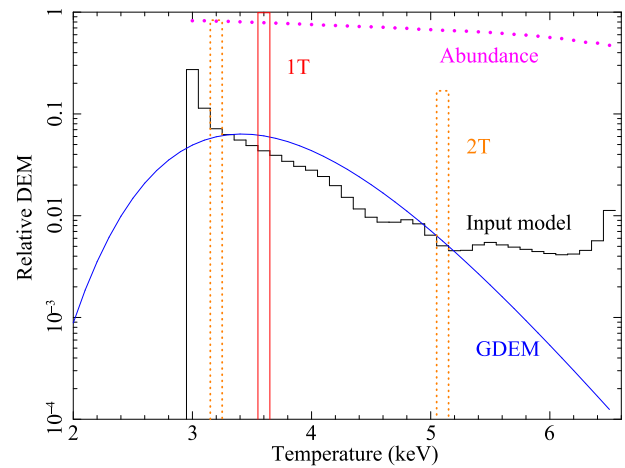


Fig. 13. Predicted DEM profile of the Perseus cluster within the FOV of the Hitomi SXS (black histogram) and the corresponding average abundance profile (relative to the proto-solar values of Lodders and Palme 2009; magenta dots). The best-fit isothermal (1T) and two-temperature (2T) models to this DEM are shown with the red and orange histograms, respectively, and the best-fit Gaussian DEM model with the blue curve. (Color online)

temperature, combined with a monotonic declining abundance pattern that also differs by a factor of two from low to high temperatures. How does this affect our modeling?

We have taken our baseline model, and replaced the main ~ 4 keV emission component with the 36 temperature components shown in figure 13. The abundances for the different temperature components are the ones shown in figure 13. For simplicity we assume that all elements have the same abundance. All other spectral components (absorption, AGN contribution, etc.) are taken to be exactly the same as in our best-fit baseline model. We then simulated this spectrum with the same exposure time as the observed Hitomi SXS spectrum, and fitted this simulated spectrum in the same way as our baseline model.

In order to avoid the overhead of having to simulate many different cases, we have turned the random noise in our simulations off. In this way, with a single simulation we get the best-fit parameters (and their uncertainties where needed). A perfect fit would then yield a formal C-statistic of 0.

We first fit this simulated spectrum with our baseline model, where the thermal emission is modeled as a single-temperature component (labeled as 1T). The best fit reaches a C-statistic value of 36.37, i.e., the isothermal approximation is poorer by 36.37 compared with the true underlying spectrum. This fit (table 5) shows some clear biases. First, the abundances of Si and S, with lines at the low-energy end of the spectrum, are too high by about 10% compared to the input model (the input model does not have a single abundance, but we list the emission-measure-weighted abundance for the input model in table 5). On

Table 5. Best-fit parameters of the simulated Perseus spectrum.

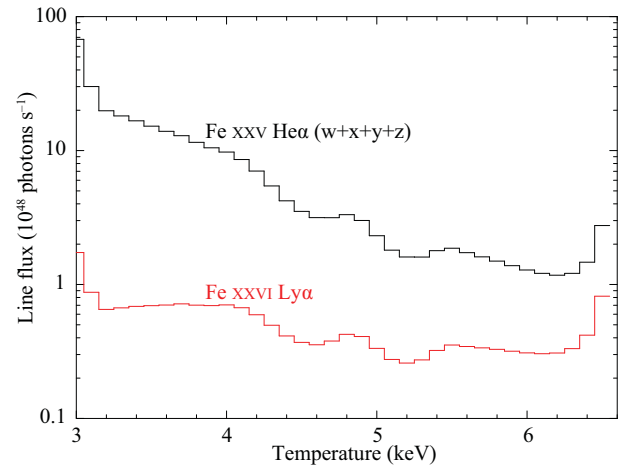
Parameter	1T	GDEM	2T	Input
C_{stat}	36.37	3.27	2.64	0
Y_1 (10^{72} m^{-3})	9.89	10.11	8.36	10.03
kT_1 (keV)	3.622	3.529	3.292	3.624
σ_T^*	—	0.112	—	—
Y_2 (10^{72} m^{-3})	—	—	1.69	—
kT_2 (keV)	—	—	5.12	—
Si	0.853	0.787	0.803	0.778
S	0.845	0.787	0.797	0.778
Ar	0.810	0.786	0.784	0.778
Ca	0.778	0.784	0.778	0.778
Cr	0.716	0.763	0.768	0.778
Mn	0.697	0.751	0.777	0.778
Fe	0.725	0.747	0.758	0.778
Ni	0.747	0.763	0.769	0.778

*A logarithmic temperature scale σ_T of the Gaussian DEM model.

the other hand, the Fe and Ni abundances are too low by 4%. As a result, the Si/Fe ratio is 15% off. This bias can be understood from the different temperature dependence of the Si/S lines compared to the Fe/Ni lines. Our model forces these lines to be formed at the same temperature, and the only way to get the line fluxes more or less right is to adjust the abundances.

Interestingly, the Cr and Mn abundances are even lower, by 8%–10%. This is due to the fact that the 1T model in the simulation under-predicts the true continuum near the dominant Cr and Mn lines by about 0.3%. As a result, the total simulated flux near these lines can be recovered only by reducing the abundances.

The temperature for this simulated 1T model (3.62 keV) is slightly lower than the temperature for the baseline model (4.05 keV). There may be various reasons for this. First, our spherically symmetric model for the Perseus cluster that we used may be too simplistic. For example, the Chandra intensity map of the Perseus cluster (Zhuravleva et al. 2014, figure 1) shows non-azimuthal fluctuations up to about 50% due to various structures within the Perseus core. Also, there are calibration uncertainties; for 4 keV plasmas, for instance Schellenberger et al. (2015) shows differences between temperatures derived from Chandra and from XMM-Newton that can easily reach 10%. It is not unfeasible that similar differences would exist between the Hitomi SXS temperature scale and that of Chandra. Finally, even with fully deprojected spectra, at the same distance from the cluster center multiple-temperature components may co-exist due to different cooling or different heating histories of different plasma elements (e.g., Kaastra et al. 2004).

**Fig. 14.** Predicted distribution of the line flux of the main $n = 1-2$ transitions of Fe XXV and Fe XXVI within the Hitomi SXS FOV. (Color online)

We then fit the simulated spectrum with the Gaussian DEM (GDEM) model, where the DEM is log-normally distributed (the blue curve in figure 13). This model gives a much better description of the simulated spectrum (table 5), with a C-statistic of only 3.27. The corresponding DEM is quite different from the DEM of our input model (the black histogram in figure 13), but because it has the same total emission measure, average temperature, and variance as the input DEM distribution, the corresponding spectra are very similar. Note that while the model parameter for the temperature of the GDEM model is 3.53 keV, its emission-measure-weighted temperature is 3.59 keV, which is very close to the emission-measure-weighted temperature of the input model (3.62 keV) or the 1T fit (3.62 keV). There is still a small bias in the derived abundances, but it is less than 4% for all elements.

The last model we fit to this simulated spectrum is a two-temperature-component model (2T) with the abundances of both components tied together. This provides a best fit (table 5) with a C-statistic value of only 2.64 and abundance bias smaller than 3%.

Finally, we have investigated the properties of the strongest lines in the spectrum. Defining line fluxes can be done in two ways: either taking the “pure” line flux, or also including other weak lines that are blended with the line of interest at the spectral resolution of the instrument. We have chosen the latter approach, and included the flux from all lines within ± 2 eV of the line of interest. Figure 14 shows the combined line flux of the four He α transitions w, x, y, and z of Fe XXV and the sum of both Ly α lines of Fe XXVI. No resonance scattering has been taken into account in these calculations. It can be seen that the Fe XXV emission is more concentrated toward lower temperatures (the emission-weighted temperature for this ion is 3.69 keV), while Fe XXVI has a much flatter distribution

(average temperature for this ion is 4.39 keV). Also, the ratio of the sum of the x, y, and z line fluxes to the w line flux changes significantly over this temperature range: from 0.79 at 3 keV to 0.63 at 6.5 keV.

7.4 Multi-temperature fitting of the Hitomi SXS data

As shown in subsection 7.3, the central region of the Perseus cluster contains multiple-temperature components. To evaluate the impact of the multi-temperature structure on the ICM parameters (e.g., turbulent velocity and abundances) for the real data, we carry out a multi-temperature fit to the Hitomi SXS spectrum. It is known that there is often more than one solution to fit a multi-temperature structure, since models with different combinations of temperatures and abundances might essentially yield a similar spectrum. Exploring these solutions is the focus of the [T paper](#). In this paper, we present three basic approximations for the temperature structure, and test them using the Hitomi SXS data.

First, we assume that the temperature distribution follows a GDEM form. As shown in subsection 7.3, the GDEM model provides a proper approximation to the radial temperature profile of the Perseus cluster as derived from Chandra data. In the fit, we adopt the peak temperature, Gaussian width of the DEM, abundances, and turbulent velocity as free parameters, and the remaining components (AGN and resonance scattering) are modeled in the same way as in the baseline model (section 3). The effective-area correction factor (appendix 1.2) is also left free, as the continuum of the GDEM model is slightly different from the single-temperature baseline model. The results of the GDEM fits are shown in table 6. The C-statistic improves by 61 compared to the baseline fit. The best-fit central temperature T is 3.83 ± 0.05 keV, and the Gaussian width

$\sigma_T = 0.13 \pm 0.01$, which indicates a significant deviation from isothermality. Note that σ_T is defined in units of $\log_{10}(T)$, hence the value of σ_T corresponds roughly to 35% of T or 1.3 keV. The GDEM fit gives lower Si, S, and Ar abundances, a similar Ca abundance, and slightly higher Cr, Mn, Fe, and Ni abundances than the single-temperature run. The abundance changes agree well with the prediction in table 5, indicating that the GDEM results are closer to the real values than the baseline results. The turbulent velocity remains intact in the new fit.

As a second approach, we apply a model with two discrete temperatures. First we assume that the two-temperature components have the same set of abundances and turbulent velocity, as well as the same foreground absorption with a column density of $1.38 \times 10^{21} \text{ cm}^{-2}$. This setting is called 2CIE_A. The other spectral components are inserted in the same way as the baseline model, and the effective area fudge factor is left free in the fitting. As shown in table 6, the C-statistic improves by 59 compared to the baseline fit. The best-fitting two temperatures are 3.36 ± 0.29 keV and 5.14 ± 0.30 keV, and the abundances and turbulent velocity agree well with those with the GDEM model. The two-temperature fit can be further improved by allowing the Fe abundances and turbulence of the two components to vary freely. This setting is then called 2CIE_B. This fitting improves the C statistic by 126 from the baseline fit.

The fitting result (figure 24 in appendix 4) shows positive residuals, about 10%–20% of the continuum level, at ~ 6.47 keV and 6.50 keV in the baseline fit. These residuals remain intact in the fittings with the GDEM or the two-temperature models. Assuming that these features are emitted at the rest frame of the Perseus cluster, they coincide with the Fe XXII and Fe XXIII DR lines, at 6.58 keV and 6.61 keV, respectively. As shown in figure 15, these Fe XXII and Fe XXIII lines are important in low-temperature (1–2 keV) plasma. Indeed, such a component was recently

Table 6. Parameters of the multi-temperature fits.

Model	C_{stat}^*	Y (10^{73} m^{-3})	kT (keV)	σ_v (km s^{-1})	Abundance (solar)								$N_{\text{H,hot}}$ (10^{24} m^2)
					Si	S	Ar	Ca	Cr	Mn	Fe	Ni	
Baseline [†]	4926.03	3.73	3.969	156	0.91	0.94	0.83	0.88	0.70	0.74	0.827	0.76	18.8
GDEM	4865.13	3.85	3.830, 0.130 [‡]	158	0.81	0.84	0.79	0.89	0.78	0.84	0.851	0.79	16.5
2CIE _A	4867.31	2.62, 1.22 [§]	3.360, 5.140 [§]	157	0.82	0.85	0.78	0.88	0.78	0.84	0.851	0.79	15.6
2CIE _B	4800.50	2.22, 1.53 [§]	3.142, 5.166 [§]	106, 215 [§]	0.81	0.85	0.80	0.90	0.80	0.84	1.041, 0.708 [§]	0.80	9.9
3CIE	4790.72	2.22, 1.26	3.578, 5.118	112, 234	0.78	0.84	0.82	0.92	0.78	0.81	0.916, 0.705	0.79	11.9

*Expected values for the baseline and multi-temperature models are 4876.

[†]The best-fit parameters of the baseline model adopted from table 1 for comparison.

[‡] σ_T of the GDEM model. It is a common logarithmic temperature scale.

[§]Parameters of the cool and hot ICM components of the 2CIE modeling.

^{||}The third component has a temperature of 1.9 keV and best fit $Y = 0.33 \times 10^{73} \text{ m}^{-3}$. The values of σ_v and Fe abundance are tied to those of the ~ 3.5 keV component.

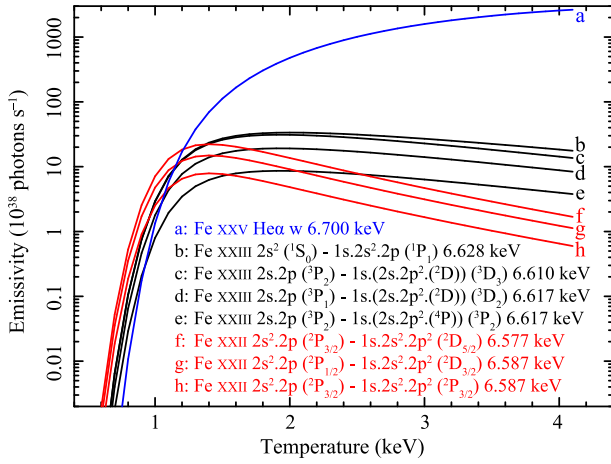


Fig. 15. Emissivities of B-like Fe XXII and Be-like Fe XXIII lines at around rest-frame energies of 6.58 and 6.61 keV, respectively, as a function of temperature. The Fe XXV He α w line is plotted as a reference. (Color online)

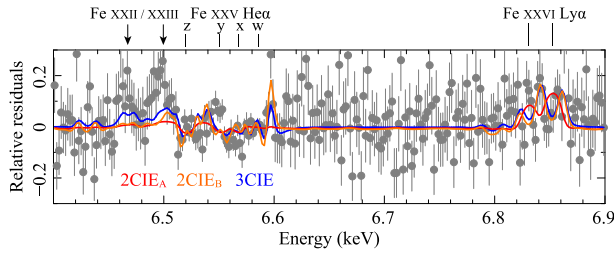


Fig. 16. Residuals of the baseline fit in the Fe band. The red, orange, and blue curves show the changes by the 2CIE_A, 2CIE_B, and 3CIE models, respectively. The black arrows indicate the redshifted energies of the Fe XXII and Fe XXIII DR line complex. (Color online)

reported to be associated with the He α -bright filaments in the Perseus cluster (Walker et al. 2015). Hence we extend the 2CIE_B model by adding a third CIE component. It becomes the 3CIE model shown in table 6. Since the third component cannot be determined well with the Hitomi SXS spectrum, we tie all of its parameters, except for the temperature and emission measure, to those of the ~ 3.5 keV component. The best-fit temperature and emission measure are 1.9 keV and $0.33 \times 10^{73} \text{ m}^{-3}$. The 3CIE model improves the C-statistic by 135 from the baseline fit, although the improvement from the 2CIE_B model is not significant ($\delta C_{\text{stat}} = 10$). As shown in figure 16, compared to the two-temperature fits, the 3CIE fit provides a better description of the Fe XXII and Fe XXIII complex at 6.47–6.50 keV.

7.5 Helium abundance

Helium is an interesting element. It does not have line transitions in the X-ray band, yet its continuum contribution relative to hydrogen varies by $\sim 5\%$ over the Hitomi SXS band, and therefore our results are affected by the adopted

He abundance. It has been discussed that the He abundance in cluster cores may be enhanced by a factor of two or more due to sedimentation (Fabian & Pringle 1977; Gilfanov & Syunyaev 1984; Qin & Wu 2000; Chuzhoy & Nusser 2003; Ettori & Fabian 2006; Medvedev et al. 2014; Berlok & Pessah 2016). However, the magnitude of the effect is hard to predict due to the role of the magnetic topology, plasma instabilities, gas mixing by mergers and turbulence, and the formation of a cool core.

We have tested the effects of an enhanced He abundance on our baseline model by enhancing the He abundance to 1.1 times its original value. The effects are shown in table 1. The main effect is an enhancement of the abundances of all metals by 0.02–0.03.

8 Systematic factors affecting the derived source parameters: Spectral components

Besides the (near-)thermal emission from the ICM, the Hitomi SXS spectrum might contain additional spectral components, such as resonance scattering and the charge exchange between hot and cold matter. Are these components properly modeled in the current atomic codes? We investigate the additional spectral components and calculate the induced uncertainties on the derived properties of the main thermal component.

8.1 Self-absorption by hot gas

As indicated in section 3, we have included a simple model to account for the absorption of photons through the cluster gas itself. In table 7 we show the transitions with strong line absorptions in the Hitomi SXS band, including the band that would have been observed if the gate valve had been opened. The optical depth τ_0 at line center is derived by assuming the best-fit baseline parameters of the column density of the hot gas $N_{\text{H,hot}}$, abundances, and velocity dispersion σ_v (table 1). The transitions with optical depths larger than 0.005 are listed. We also list the oscillator strength f and the total transition probability A from the upper level of the line that is used in these calculations (Voigt absorption profiles are being used).

Clearly, the Fe XXV resonance line (He α w) has the greatest optical depth, but we see significant contributions from the other lines of the same Rydberg series, as well as for other ions of Fe and other elements. Also, the optical depth of the Fe XXIV lines that block part of the He-like intercombination line (Mehdipour et al. 2015) is up to 2%, a level that is detectable (for the intercombination line, the statistical uncertainty of the spectrum over one instrumental FWHM of 5 eV is about 3%).

Table 7. Strongest absorption lines in the Perseus spectrum.*

Line	E (keV)	τ_0	f	A (10^{12} s^{-1})
O VIII Ly α_2	0.6535	0.017	0.139	2.6
O VIII Ly α_1	0.6537	0.033	0.277	2.6
Ne X Ly α_2	1.0215	0.010	0.139	6.3
Ne X Ly α_1	1.0220	0.020	0.277	6.3
Mg XII Ly α_2	1.4717	0.008	0.139	13
Mg XII Ly α_1	1.4726	0.016	0.277	13
Fe XXIII L β	1.1251	0.007	0.256	4.7
Fe XXIII L β	1.1290	0.011	0.410	7.6
Fe XXIV L β	1.1627	0.036	0.126	7.4
Fe XXIV L β	1.1674	0.070	0.243	7.2
Fe XXIV L γ	1.5505	0.007	0.032	3.3
Fe XXIV L γ	1.5525	0.013	0.062	3.2
Fe XXIV L δ	1.7304	0.005	0.026	1.7
Si XIV Ly α_2	2.0043	0.018	0.139	24
Si XIV Ly α_1	2.0061	0.037	0.277	24
Si XIV Ly β_1	2.3766	0.006	0.053	6.5
S XV He α w	2.4606	0.008	0.767	67
S XVI Ly α_2	2.6197	0.016	0.139	41
S XVI Ly α_1	2.6227	0.031	0.277	41
Ar XVII He α w	3.1398	0.005	0.775	111
Ar XVIII Ly α_1	3.3230	0.010	0.277	66
Ca XIX He α w	3.9023	0.011	0.782	172
Ca XX Ly α_1	4.1075	0.008	0.277	101
Fe XXIV r †	6.6533	0.008	0.157	343
Fe XXIV q †	6.6619	0.025	0.489	471
Fe XXV He α w	6.7004	0.338	0.798	518
Fe XXV He β_1	7.8810	0.056	0.156	140
Fe XXV He δ_1	8.2955	0.020	0.058	58
Fe XXV He γ_1	8.4874	0.009	0.028	29
Fe XXVI Ly α_2	6.9517	0.011	0.139	291
Fe XXVI Ly α_1	6.9732	0.021	0.277	292
Ni XXVII He α w	7.8051	0.013	0.683	602

*Data based on SPEX v3.03; the rest-frame energy E , optical depth τ_0 at line center with the best-fit parameters of the baseline model, oscillator strength f , and transition probability A .

† DR satellite transitions of 2s–1s.2s.2p. See table 11.

In our baseline model, we have coupled the turbulent velocity, the Doppler velocity, and the temperature to the corresponding parameters of the dominant thermal emission component. We have also tested a model where we have decoupled these quantities. We obtain an insignificant improvement of our model (see table 1) with a temperature of $3.8 \pm 0.6 \text{ keV}$ for the absorbing gas, a velocity relative to the hot gas of $10 \pm 30 \text{ km s}^{-1}$, a LOS turbulent velocity dispersion of $191 \pm 35 \text{ km s}^{-1}$, and a column density of $(20.1 \pm 2.2) \times 10^{24} \text{ m}^{-2}$. All these parameters are fully consistent with the parameters of the emission component within the uncertainties of those emission parameters, but obviously we cannot exclude that the properties of the

absorbing gas are, on average, within the range indicated by the above uncertainties.

Our model substitutes a simple absorption model for resonance scattering effects. It assumes a common hydrogen-equivalent column density for all the transitions listed in table 7, ignoring the spatial structure of the ICM. The model also ignores the re-emission process after absorption, which possibly results in lower estimation of optical depths. A more accurate characterization of resonance scattering requires radiative simulations, which will be separately presented in the RS paper.

8.2 Charge exchange contributions

Charge exchange (CX) happens when a neutral atom collides with a sufficiently charged ion, which recombines with the electron(s) captured from the atom. The product ion often has a highly excited state with a large principal quantum number n , and thereafter the decay of the excited electron(s) will fill the inner-shell vacancies through line emission. Therefore, the most characteristic features of CX emission in X-rays are the transitions from high- n shells to the ground, which are much stronger than those in the CIE case. The CX spectrum also exhibits higher Ly β -to-Ly α and forbidden-to-resonance (z-to-w) ratios, although these features can be achieved by other atomic processes (Gu et al. 2016b).

In this section we examine the CX contributions to the ICM emission of the Perseus cluster with the Hitomi SXS spectrum. The CX component adopted here is described in Gu, Kaastra, and Raassen (2016a). It uses velocity-dependent, n L-resolved (He-like) or n -resolved (H-like) reaction cross-sections, based primarily on the multi-channel Landau–Zener calculations (Mullen et al. 2016). The low-energy weight function [equation (4) of Gu et al. 2016a] is applied to the H-like data in which the l -distribution cannot be obtained by the Landau–Zener calculations. For the Li-like and Be-like sequences, it includes velocity- and n L-resolved cross-sections, which are derived from an empirical scaling relation presented in Gu, Kaastra, and Raassen (2016a). In this model, only the atomic component of the cold gas is considered, although in reality the molecular gas also contributes. The collision velocity is set to 200 km s^{-1} (Conselice et al. 2001), and the ionization temperature and abundances of the CX ions are fixed to the best-fit values of the ICM thermal component. As shown in table 1, a new baseline run including the CX component results in a minor C-statistic improvement ($\delta C_{\text{stat}} = 13$).

The fit prefers that the CX lines are more broadened than the CIE lines, with a turbulent velocity $v_{\text{mic}} \gtrsim 600 \text{ km s}^{-1}$ (or $\sigma_v \gtrsim 400 \text{ km s}^{-1}$). Since the actual line profile cannot be determined by the current data, we fix the turbulent velocity

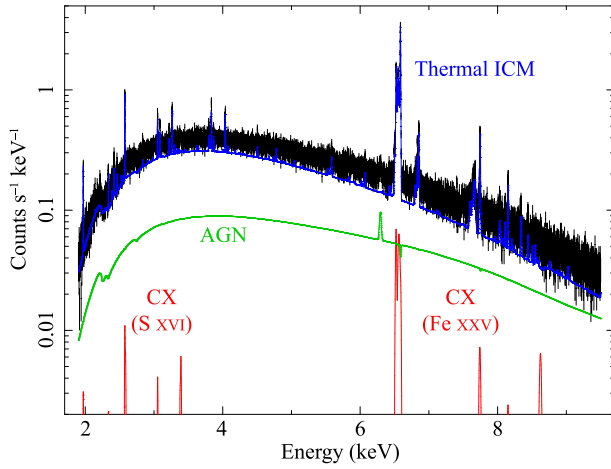


Fig. 17. Best-fit result with the CX emission. Each X-ray emission component is shown: thermal ICM in blue, AGN in green, and CX in red. (Color online)

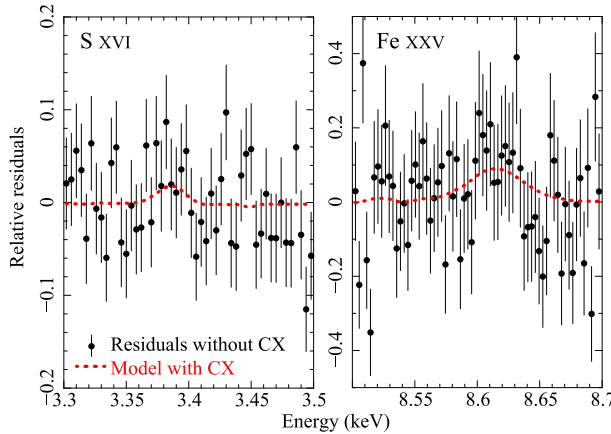


Fig. 18. Residuals of the baseline fit in the S XVI 3.2–3.6 keV (left) and Fe XXV 8.3–8.8 keV (right) bands. The red curve in each panel shows the model change by including the CX component. (Color online)

of the CX component at $v_{\text{mic}} = 800 \text{ km s}^{-1}$, corresponding to σ_v of 566 km s^{-1} , which is the upper limit of the neutral atomic line width of the molecular cloud near NGC 1275 as reported in, e.g., Salomé et al. (2011). The large line width might be caused by a combined effect: it can be partially contributed by the kinematics of the neutral cloud and the ICM, and partially from the atomic uncertainty of the capture state (Gu et al. 2016a), as the CX lines from $n \geq 10$ levels are often blended. Changing the turbulent velocity to a larger value (e.g., 1000 km s^{-1}) has a negligible effect on the fit.

As shown in figures 17 and 18, the CX model predicts that the most promising high- n transitions are seen in the S XVI band, which has been reported by Hitomi Collaboration (2017a), as well as the Fe XXV band. The CX lines contribute to $\sim 1\%$ of the continuum for S XVI at $\sim 3.4 \text{ keV}$,

and $\sim 3\%$ for Fe XXV at $\sim 8.6 \text{ keV}$. To measure the statistical uncertainties, we replace the CX model with two Gaussian lines at the energies of the S XVI and Fe XXV high- n transitions. The Gaussian FWHM is set free for each line. The S XVI and Fe XXV CX lines have 1.6σ and 2.4σ significances, respectively. However, it is premature to claim the detection of CX with the current data, since the uncertainty from the effective area/gain calibration is large and energy dependent, as discussed by Hitomi Collaboration (2017a). For the remaining ions, the high- n transitions are negligible, either due to the low abundances, or to blending with strong thermal lines.

As shown in table 1, inclusion of the CX component has minor effects on the ICM temperature, emission measure, and turbulent velocity. The Fe and Si abundances are reduced by $\sim 5\%$ and 2% , respectively, and the S, Cr, Mn, and Ni are affected by 1% – 3% . Since the CX emission has a larger forbidden-to-resonance (z-to-w) ratio than the thermal emission, the equivalent $N_{\text{H,hot}}$ for the possible resonance scattering is reduced by about 7% . The effect on the resonance scattering study will be further discussed in the RS paper.

8.3 AGN contribution

To assess the uncertainty from the AGN flux, here we first consider an extreme condition: the central AGN is quite dim and its power-law emission is negligible. As shown in table 1, the non-AGN run gives a much worse fit ($\delta C_{\text{stat}} = 625$) than the original baseline fit, and the best-fit temperature shifts by 0.5 keV . The abundances are systematically lower by 0.01 – 0.21 solar.

Next we examine a more realistic case for possible systematic uncertainty related to the detailed AGN modeling. The AGN spectrum in the baseline model was established in the early study for the AGN paper with the PSF photometry. The technique is essentially unchanged in the final analysis, but the energy band is extended up to 20 keV with the `sxsextend` tool. The broader-band spectrum requires a slightly flatter photon index and an $\sim 20\%$ lower flux in 2 – 10 keV (see the AGN paper for details). Another notable update is the RMF type, which has been changed from the large size (also used in our baseline model) to the extra-large size to include electron-loss continuum. As we examine the effect of using different types of RMF separately (subsection 3.2), we use the new AGN model derived by the same method as in the AGN paper but with the large-size RMF for a straightforward comparison with the baseline model. Therefore, slightly different parameter values from the AGN paper are adopted in our test: the photon index of 1.85 and the 2 – 10 keV flux of $2.9 \times 10^{-14} \text{ W m}^{-2}$ (H. Noda & Y. Fukazawa 2017 private communication).

The new AGN model run gives a slightly poorer fit ($\delta C_{\text{stat}} = 11$) than the original baseline model. The lower AGN flux requires a significant rise of the ICM continuum by 6%, which results in 3%–4% lower abundances. The change in the ICM gas temperature becomes insignificant, unlike the no-AGN case.

9 Systematic factors affecting the derived source parameters: Fitting techniques

In this section we discuss the effects of applying different fitting techniques on the derived parameters of the baseline model.

9.1 Comparison of χ^2 -statistics versus the default C-statistics

It is well known that the use of χ^2 -statistics in spectral fitting can give a bias in the estimated parameters (e.g., Nousek & Shue 1989; Mighell 1999). The proper way to resolve this is to use the C-statistic (Cash 1979), and we have done so for our baseline model. We use the modification of the C-statistic as proposed by Castor (see the Xspec manual,⁶ Arnaud 1996). This modification is the standard in the Xspec and SPEX packages. Our present Hitomi SXS spectrum offers an excellent opportunity to demonstrate the bias that one gets when using χ^2 -statistics. We have taken the baseline model and replaced the C-statistic with the χ^2 -statistic in the spectral fit. The best-fit model has $\chi^2 = 6192$ for 5790 degrees of freedom. The value of the C-statistic that corresponds to this χ^2 -optimized fit is 88 higher than for the baseline model. We show the relative difference between both models in figure 19.

It can be seen that the continuum for the χ^2 fits is about 1% lower than for the baseline model, while some of the stronger emission lines have similar fluxes for both cases. This 1% bias is caused by the well-known effect that χ^2 fits tend to give lower fluxes by giving relatively more weight to the data points that by chance have a flux below the expected value than to the data points that have a flux above it. Our present spectrum has typically 100 counts in most continuum bins, and according to Mighell (1999) this would give a bias of about 1 count, in remarkable good agreement with our findings here. Note that for typically 100 counts per bin, the Poissonian error bars are about 10 counts, hence much larger than the differences between the models. This shows that biased fits are easily overlooked if plotted at full resolution. Only rebinning the best fit drastically (with a factor of at least 100 or so) would show the bias.

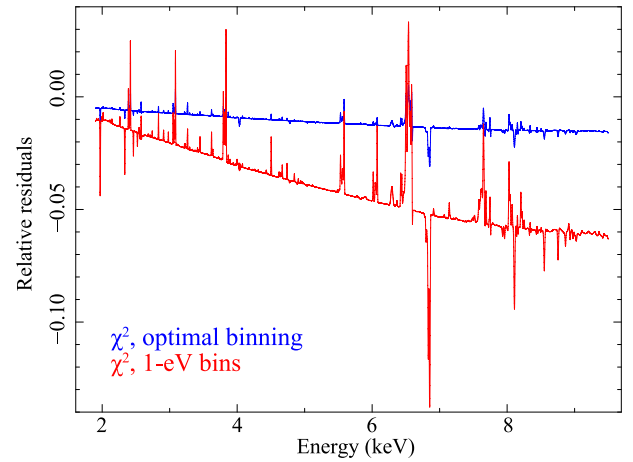


Fig. 19. Relative differences between a χ^2 fit and a C-statistic fit (blue curve) for the baseline model. The red curve shows the same, but with 1 eV bins instead of optimal binning. (Color online)

The bias becomes even stronger if in addition to using χ^2 -statistics we drop the optimal binning and use 1-eV bins (see the red curve in figure 19). In addition to a lower flux, there is now also a significant bias in the temperature, leading to a different overall slope of the spectrum. The bias is even 6% at the highest energies.

9.2 Optimal binning versus other binning

We have also tested how our results depend on the adopted bin size. When we use the C-statistic, we find no difference at all for the parameters shown in table 1 when comparing our optimal binning with a uniform binning of 1 eV. This is easily understood by noting that our optimal binning already gives a bin size of 1–2 eV for all bins (see appendix 1.3), and that it is more the order of magnitude of the bins rather than the precise bin size that matters for the sensitivity of statistical tests (Kaastra & Bleeker 2016, see figure C3).

Note that when χ^2 is being used, binning is important, but as we demonstrate in subsection 9.1, the use of χ^2 -statistics should be avoided.

9.3 Local fit versus global fit

Astrophysical spectroscopic analysis in the radio through ultraviolet bands often relies upon precise measurements of selected strong emission lines (e.g., H I 21 cm, Fe II 1.257 μm , and [O III] 5007 Å) whose atomic and diagnostic properties are well understood. This can also be done with X-ray spectroscopy (Hitomi Collaboration 2016), but both the physics of X-ray-emitting plasmas and the availability of high-resolution spectrometers create significant challenges.

⁶ (<https://heasarc.gsfc.nasa.gov/xanadu/xspec/manual/>).

The Hitomi SXS spectrum of Perseus presents a clear combination of emission lines with a continuum, implying it can be completely understood via fits with the sum of a simple continuum plus a series of Gaussian emission lines, with astrophysical parameters derived from positions, widths, and flux ratios of the Gaussian parameters. An advantage of this approach is that it requires a relatively small amount of reliable atomic data, enabling the use of experimentally verified and theoretically understood features. For example, the ratio of the line intensity of the Ly α line to its resolved DR satellites depends critically on the electron temperature; therefore, advanced line diagnostics using multiple DR satellite lines even test whether the underlying plasma is in thermal equilibrium (Gabriel & Phillips 1979; Kaastra et al. 2009).

Although elegant, and without doubt useful for obtaining an approximate description, this approach will miss details resulting from a self-consistent fit of the full spectrum. Three key problems occur with X-ray spectral analysis via purely local line fits:

- (1) Unlike other spectral bands, the line emission and continuum emission arise from the same plasma. Therefore, simplifying the continuum to a spline fit or even bremsstrahlung emission independent of the line components ensures that the resulting analysis will miss features. The X-ray continuum, even in strict collisional ionization equilibrium, contains significant contributions from radiative recombination continua and two-photon emission (see, e.g., figure 8 in Kaastra et al. 2008). While these components can be included in the fit, e.g., the APEC No-Line model used in Plucinsky et al. (2017), separating line from continuum emission makes finding a self-consistent model all but impossible.
- (2) X-ray spectrometers, even the SXS, have only limited resolution, while the X-ray bandpass has a plethora of strong lines, making line blending an ongoing problem. Table 10 in appendix 5 shows several instances of lines from different elements separated by less than the instrumental resolution. Worse, the narrow bandpasses of often-used diagnostic lines such as the He α complex include a multitude of DR satellite lines together with the strong “triplet” (actually a quartet) lines. Many of the lines have multiple excitation channels, all of which must be known in order to fit the complex reliably. This is especially true of the forbidden line (z), as discussed earlier. For the SXS spectrum, Gaussian lines were used to determine the turbulent motion (Hitomi Collaboration 2016), but a local form of the global fit is required to extract the maximum amount of information even from a relatively small bandwidth. At a minimum, when applying line ratio diagnostics it must be clear both in

the model and in the data whether these contaminants have been taken into account.

- (3) Few, if any, sources in the Universe will be in perfect equilibrium, either collisional or photo-ionized. The present spectrum of the Perseus cluster is a good example of such complexities. While dominated by a 4 keV temperature component, the possibility of multiple temperatures cannot be eliminated based on the data (subsection 7.4), and is certainly expected theoretically. Depending upon their excitation mechanism, each emission line will be affected differently by these effects, rendering the use of just one or two diagnostic ratios precise but quite inaccurate. Using many lines, including upper limits to non-detections, will avoid this problem, but at some point the distinction between a many-line fit vs. a global fit will become blurred.

Despite the above issues, line ratios may be preferred over global fits either when the source spectrum is too complex to be fully understood, or when calibration uncertainties dominate the broad-band spectra. Of course, the accuracy of the physical parameters derived from global fits also relies upon complete and accurate atomic databases. In the case of completeness, global models contain potentially millions of atomic transitions, most of which have not been experimentally verified. While “spot” checks do exist, in most cases the accuracy of the data is not well known, i.e., estimates of uncertainties are determined by comparing results from different theoretical calculations, or by using uncertainties from portions where experimental results do exist.

In our case, we have shown that the calibration and completeness of the spectral models are not perfect but good enough to yield a very good description of the Perseus spectrum. Ultimately, local and global fits must be used in a complementary way. The broad bandwidth coupled with the high spectral resolution of the SXS makes it possible to take advantage of the strengths of both methods, improving the reliability of the derived physical parameters of the source.

10 An improved model

To fit the Perseus spectrum, we introduced a baseline model (section 3) which mainly consists of an ~ 4 keV CIE plasma and an AGN component. Obviously, the baseline model is merely a simple approximation (subsection 7.4), even though it already achieves a satisfactory fit based on the current Hitomi SXS data. Throughout the paper, we have tested a variety of plasma codes, atomic data calculations, plasma and astrophysical modelings, additional spectral components, and instrumental effects, and compared them

with the original baseline fit. By properly incorporating some of the atomic and astrophysical effects into the baseline model, we are able to achieve a more advanced physical model of the Perseus spectrum.

We construct an improved model as follows. Following the baseline model, SPEX version 3.03 is used, the abundance standard is the Lodders and Palme (2009) proto-solar values, and the ionization balance is set to U17. The thermal emission is modeled now by the sum of three CIE components, with temperatures of about 2 keV, 3.5 keV, and 5 keV (subsection 7.4). The three-temperature model is chosen since it gives the best fit of all multi-temperature modelings (table 6). The three components have the same Si, S, Ar, Ca, Cr, Mn, and Ni abundances, while the Fe abundance and turbulent velocity are left free for the 3.5 keV and 5 keV components. For the 2 keV component, the Fe abundance and turbulent velocity are tied to those of the 3.5 keV component (subsection 7.4). The AGN contribution, resonance scattering, and Galactic absorption components are added in the same way as for the baseline model. The possible CX component (subsection 8.2) is included in the improved model. Following subsection 6.1, the Voigt function is used to describe the line profiles. We refit the effective area correction factor in the same way as described in appendix 1.2, and show the best-fit model in figure 22a.

The improved model achieves a best-so-far C_{stat} , 4779 for an expected value of 4876 ± 99 , which is significantly better than the baseline fit ($C\text{-statistic} = 4926$). The best-fit model is plotted in appendix 4 (figures 23–25), and the stacked residual diagram is shown in figure 20. The residual diagram is calculated by adding a *line* component, with the central energy moving from 1.9 keV to 9.5 keV with a

step of 3 eV, on the best-fit baseline and improved models. Compared to the baseline run, the residuals at $>2\sigma$ are greatly suppressed by the improved fit, and the diagram follows well the expected Gaussian distribution. As shown in table 1, the new model essentially reproduces the best-fit results of the three-temperature model (subsection 7.4). The best-fit temperatures are 1.92 ± 0.21 keV, 3.61 ± 0.33 keV, and 5.43 ± 0.38 keV for the three components. Note that the values are sensitive to the detail of the spectral modeling as well as the calibration of the instrumental response (see the T paper for further details). All the Si, S, Ar, Cr, Mn, and Ni abundances become roughly 0.8 solar, which are much more uniform than the baseline results. The Ca abundance remains about 0.9 solar. The best-fit Fe abundances are 0.91 ± 0.05 solar and 0.64 ± 0.05 solar for the 3.5 keV and 5 keV components, respectively. The turbulent velocities become $\sigma_v = 117 \pm 11$ km s $^{-1}$ for the 3.5 keV component and $\sigma_v = 223 \pm 27$ km s $^{-1}$ for the 5 keV component. This may suggest that the cooler ICM tends to have a lower level of turbulence than the hotter one, but the results depend on the assumed temperature structure and are sensitive to the continuum modeling including the effective area calibration. The further details are discussed in the V paper. Moreover, the improved model gives a self-absorption column density of $(1.05 \pm 0.15) \times 10^{25}$ m $^{-2}$. The column density of Fe xxv is thus $(2.18 \pm 0.23) \times 10^{20}$ m $^{-2}$, in good agreement with the value that we derive from the simulated spectra in subsection 7.3 (4.02×10^{20} m $^{-2}$ for the semicolumn of a line through the core; 2.64×10^{20} m $^{-2}$ for the semicolumn averaged over the Hitomi SXS FOV). Details on the derived resonance scattering are discussed in the RS paper.

11 Discussion

11.1 Important factors

We have shown in this paper the dependencies of several, astrophysically interesting parameters, mainly focusing on the plasma modeling, i.e., plasma codes and atomic databases. We have also investigated the dependencies on astrophysical modeling as well as spectral fitting techniques. For a proper astrophysical modeling of the present Perseus cluster spectra, as presented here but discussed in greater detail in a set of other papers (Hitomi Collaboration 2016, 2017a, Z, T, RS, V, and AGN papers), it is crucial to understand the possible systematic biases on the derived parameters. Table 1 provides a comprehensive list of the estimated biases, which enables us to inter-compare various aspects of systematic uncertainty. The effects of some of the plasma modeling factors are comparable to, or even larger than, the statistical or instrumental uncertainty (appendix 3). Because this is the only high-quality high-resolution X-ray spectrum

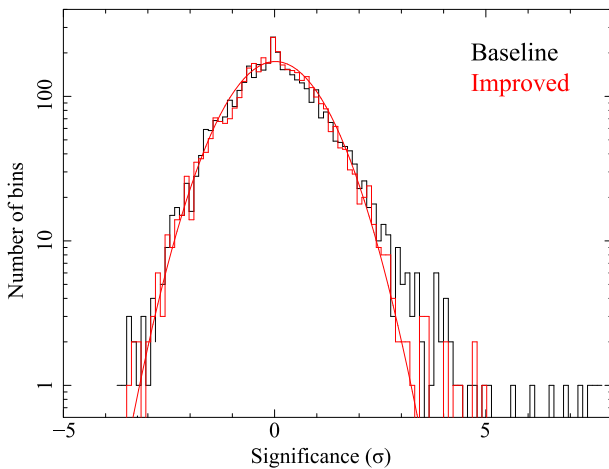


Fig. 20. Diagrams showing the significance of an additional *line* model on top of the best-fit baseline model (black) and improved model (red), with the central energy moving across the entire band. The red curve shows a $\sigma = 1$ Gaussian function that fits the diagram of the improved model. (Color online)

of a spatially extended thermal X-ray source up to now, it is also important for the preparation of future X-ray missions, in the sense that priorities in calibration, astrophysical modeling, or data analysis can be set.

11.1.1 Emission measure

The emission measure Y of the cluster ICM is a good representative of the absolute flux of the hot cluster gas. First, it is clear that we need to use the latest `aharfgen` to obtain an accurate emission measure (see appendix 3.4.5). Although the emission measures are uniformly underestimated by 20% for the other cases with the older software, hereafter we ignore the difference and compare the relative values to find out which parameter affects Y .

The main contributor to the systematic uncertainty on Y is the adopted flux of the central AGN. Ignoring the AGN completely would give a 20% higher emission measure as well as 12% higher temperature for the hot gas. In fact, the AGN contribution affects almost all parameters of the hot cluster gas. Because we are not completely ignorant about the AGN flux, the true uncertainties are smaller than described above. One example of more realistic estimation is the difference in updating the AGN model with the broader-band spectroscopy, which gives a 6% higher emission measure.

Other important factors for Y are the effective area correction (up to 4%), the ionization balance (3%), and the assumption of isothermality (σ_T free, 3%). The differences between the plasma codes, for which we consider here SPEX version 3.03 and AtomDB version 3.0.8 (SPEX and AtomDB briefly hereafter) to be the most sophisticated, are not very important for the emission measure: differences are less than 1%.

11.1.2 Temperature

Ignoring from now on the AGN contribution uncertainty, the most important factor affecting the temperature of the dominant 4 keV component is the fitting techniques. Using unbinned spectra and χ^2 statistics biases the temperature by 5%. Forcing isothermality (i.e., putting σ_T to be zero) gives a 3.5% bias. Using the official effective area correction based on the on-ground calibration, instead of the additional effective area correction using a thinner Be-filter and `knak` gives a 3% bias (appendix 1.2). Both plasma codes (SPEX and AtomDB) agree relatively well in their derived temperature (better than 2%).

11.1.3 Turbulent velocity

While the temperature agreement between the plasma codes is good, they result in a 10% difference in the derived amount of turbulence in the plasma. This uncertainty is almost as large as the uncertainty introduced by

ignoring completely the resonance scattering or ignoring the position-dependent bulk velocity field (both 9%).

11.1.4 Cluster velocity

This bulk velocity field obviously also affects the derived velocity centroid of the cluster (23 km s^{-1}). Obviously, the gain correction is also important (14 km s^{-1}). Finally, the use of SPEX or AtomDB also results in a difference of 6 km s^{-1} .

11.1.5 Resonance scattering

The plasma codes result in an even bigger difference of 40% in the derived column density of the resonantly scattering plasma, six times larger than the statistical uncertainty on this quantity. This relatively large difference is likely associated with the systematic uncertainties in the line emissivities, because in comparison we use the same resonance scattering model (the SPEX *hot* model). However, precise modeling of the temperature structure (see our improved model) is also important: this can also produce a difference of 35%.

11.1.6 Abundances

Finally, we discuss here the uncertainties on the abundances. The most striking is the difference in the Fe abundance associated with the plasma code: AtomDB gives a 16% lower abundance than SPEX. This is 17 times higher than the small statistical uncertainty on the Fe abundance. The differences can be attributed mostly to differences in the adopted collisional excitation and DR rates of the strongest spectral lines (subsections 5.1 and 5.3). Other factors affecting the Fe abundance are the inclusion of resonance scattering (11%) and CX (5%). On the other hand, the Ni abundance is almost biasfree between the latest SPEX and APEC/AtomDB (at least within its 7% statistical uncertainty; however, the bias between SPEX versions 2 and 3 is still significant. See also the [Z paper](#).). This is not the case for other elements. The Si and S abundance can be biased by 6%–14% depending on each of the following four factors: the plasma code, the isothermality assumption, the gain correction, and the fitting method (χ^2 fitting on unbinned data). For Ar and Ca, the main systematic uncertainties are associated with the plasma model (6%–8%). Finally, for Cr and Mn, both the isothermality assumption and the fitting method are the main sources of systematic uncertainty.

11.1.7 Implications for other observations

So far we have reviewed the state-of-the-art knowledge, mostly on the K-shell transitions, for modeling the hot (several keV) tenuous plasma in collisional ionization equilibrium. We caution that the atomic uncertainties derived from the Perseus data cannot simply be copied to observations

of other sources, as the accuracy of atomic data depends strongly on the types of transitions (tables 2 and 3), as well as on the plasma conditions, such as electron temperature (figures 2 and 4) and ion charge states (figures 6 and 7). For instance, X-ray emission from a stellar corona (or an elliptical galaxy) is dominated by transitions in the Fe-L complex, which are known to be computationally more intricate than those in the Fe-K (e.g., Bernitt et al. 2012), and hence less accurate (e.g., de Plaa et al. 2012).

A more important issue is to discuss the atomic uncertainties in the science cases. The Doppler measurement of line-of-sight velocities would be subject to the reference-wavelength accuracy of the dominant transitions, except for the cases with large bulk velocities, for example in young supernova remnants (SNRs). The precise characterization of turbulence velocity structures, i.e., search for non-Gaussianity, would primarily be limited by the accuracy of the atomic and astrophysical modeling of the RS effect. This could be avoided by making use of local fits of optically thin emission lines, and in this case relative line energies and emissivities of satellite lines as well as the calibration of the line spread function are the dominant source of uncertainty. The detection of a small departure from CIE (e.g., for merger clusters; Inoue et al. 2016) would mainly be limited by the uncertainties in the charge-state distribution calculation, and thus ionization and recombination rates adopted therein (subsection 7.2). Revealing the detailed time evolution of NEI plasma by measuring the charge-state distribution (e.g., for recombining plasma in SNRs; Sawada & Koyama 2012) would require an even higher level of accuracy for these transition rates, including multiple ionization due to inner-shell processes followed by Auger ejections. The elemental abundance measurement is affected mostly by the errors of the line excitations and branching ratios for individual transitions, including those for the satellite lines, although only the error of the total emissivity of a line complex (e.g., He α) would matter in a system with a large intrinsic line broadening (~ 100 eV) like young SNRs where the ion temperature is considerably high (\sim MeV).

The atomic uncertainty in each science case can be evaluated by the Monte Carlo approach introduced in subsubsection 5.1.2. Ultimately, the atomic error calculation should be implemented as a standard analysis procedure in the spectral modeling packages. This would require substantial work in the code development by assessing the accuracy of detailed atomic data.

11.2 Atomic data needs

As shown throughout this paper, the reliability of a spectral modeling package lies not only in the accuracy and completeness of its atomic data, but also in its ability to properly

synthesize the atomic data as a function of physical parameters, i.e., the plasma conditions, such as temperature and density. Synthesizing the data is tedious and computationally taxing owing to the fact that the databases employed are large, containing millions of data points, including transition energies, excitation and ionization cross sections, resonant (multi-electronic) and non-resonant (radiative) recombination cross sections, and non-thermal processes, such as CX recombination. Different models use atomic databases of varying levels of completeness and accuracy, as well as different synthesis methods, in their calculations. Estimates of a model's accuracy are often given by comparison to other models. However, a true measure of a model's accuracy can only be determined by comparison with laboratory benchmark measurements.

Benchmark measurements, generally, come in two forms: as isolated experiments, where a single ionic species or atomic process is studied, or as integrated experiments, where emission or absorption is measured from several simultaneous ions and atomic processes as a function of temperature or density. Isolated experiments include those conducted at electron beam ion traps, advanced light sources, or storage rings. Integrated experiments include experiments using, for example, tokamaks or laser-produced plasmas. Isolated experiments generally test portions of atomic databases, and integrated experiments test synthesis models. Examples of isolated experiments include measurements of absolute electron-impact excitation cross-sections as a function of electron energy, transition energies, natural line widths, and oscillator strengths (Beiersdorfer et al. 1992; Brown et al. 2006; Rudolph et al. 2013). Examples of integrated experiments include the spectral signature of the He α complex as a function of electron temperature (Bitter et al. 2008; Gu et al. 2012; Rosen et al. 2014; Rice et al. 2015), or full Fe-K and Fe-L shell spectral signatures as a function of temperature and density.

Providing laboratory benchmarks for the atomic database in all physical regimes for all astrophysically relevant ions is not tractable. Hence, models are tested by comparison with measurements where available. Typically, models agree with measurements at the 10%–20% level in the cases of excitation and ionization processes. Transition energies, however, are of much higher accuracy. In the case of H- and He-like ions, measurements of the transition energies have tested theory at the level of a few to a few tens of parts per million (Johnson & Soff 1985; Beiersdorfer 2009; Beiersdorfer & Brown 2015). In the case of ions with more bound electrons, i.e., L-shell ions, the accuracy of the models is not as well known, as experimental benchmarks are more sparse and an agreement with theory varies.

The inability of the standard X-ray astrophysics models to accurately fit a significant fraction of the lines in the

SXS Perseus spectrum (Hitomi Collaboration 2016) not only uncovered some of the limits of SPEX and APEC, but it also showed the limits of the high-accuracy laboratory measurements. For example, laboratory measurements of relative line intensities in the Fe He α complex, in particular the strength of the forbidden line (z), still introduce a limit to our ability to take full advantage of the line complex's diagnostic power. The high-quality SXS Perseus spectrum gives the impetus to more complete and higher-accuracy calculations and systematic measurements of all the processes involved in exciting, not only the forbidden line (z), but all of the lines found in the He α complex, and not only for He-like Fe XXV, but also for other astrophysically relevant He-like ions. Measurements such as these will be paramount in interpreting the high-resolution spectra to be returned by future high-resolution X-ray spectroscopy missions (see subsection 11.3). Largely driven by their large bandwidths, high energy resolution, and large collecting areas, high-accuracy measurements of a plethora of atomic parameters will be required.

While providing a complete list of required measurements is beyond the scope of this paper, a few necessary measurements, in addition to the studies of He α , should be mentioned. For example, a more complete study of the excitation cross-sections and spectral signatures of CX recombination should be completed. Many CX studies have been completed; however, at present, theory has not been matured to a point of consistently predicting experimental results, and hence the diagnostic capability of CX emission is limited. Absolute cross-section measurements for electron-impact excitation followed by cascades, especially in the case of high- n transitions, with an accuracy of the order of 5%–10%, should also be a high priority as they determine the line strengths and, in turn, relative ion abundances (ionic fractions) and elemental abundances from a variety of celestial sources. High-accuracy measurements of DR-resonance strengths and of ionization cross-sections should also be pursued. Similar laboratory measurements of photo-excitation and ionization processes should also be conducted, as these are the basis for determining column densities and scattering effects (RS paper).

One of the most sought-after and challenging integrated laboratory experiments is an accurate measurement of the ion charge balance as a function of electron temperature and density. This is a universal goal throughout plasma physics, spanning nearly all temperature and density regimes. Integrated experiments such as these are challenging because it is hard to know with high accuracy what the systematics are of the source plasma, i.e., it is often hard to quantify or experimentally discount gradient and non-uniformity effects. Regardless of these challenges, integrated experiments where the plasma parameters have been

independently well diagnosed have been successfully conducted (Rosen et al. 2014).

11.3 Prospects for XARM, Athena, and other missions

The Hitomi SXS observation of Perseus, with its high-resolution spectrum in the 1.9–9.5 keV band, showed both the strengths and weaknesses of existing plasma codes. Pre-launch versions of both SPEX and AtomDB codes provided generally plausible fits to the observation, matching the continuum and many of the strong lines well. While neither fit was formally statistically acceptable (see table 1), the two codes agreed (to within ± 0.3 keV) on the best-fit temperature, and to within ± 0.2 on elemental abundances. At CCD resolution, these discrepancies could easily be understood as calibration issues or inadequacies of the collisional isothermal model; only at the resolution of the SXS were apparent the clear problems with both codes. As described above, many of these disagreements could be addressed by updating wavelengths and cross-sections for a few weaker lines and by fixing minor code bugs. As a result, both SPEX and AtomDB are in close agreement about the emission from a 4 keV collisional plasma in 1.9–9.5 keV.

That an SXS observation was required to discover and address these problems may seem odd, as gratings on both Chandra and XMM-Newton have provided high-resolution X-ray spectra of point sources since 1999. Unfortunately, most X-ray point sources have intrinsically complex and variable spectra: stellar coronae include plasmas with a broad range of temperatures, while any model of the absorbed photo-ionized spectra of X-ray binaries and AGNs must include a range of different geometries and source spectra. The only truly simple point-source spectra are isolated neutron stars or white dwarfs, which have no features in the X-ray band and are therefore used as calibration sources. As a result, few grating observations could be used to test details of the plasma models beyond the strong lines, since any differences in weaker features could reasonably be due to issues in the source model and not the code.

Substantial work therefore remains to ensure that current plasma codes will be ready to face the challenges of data from the X-ray Astronomy Recovery Mission (XARM), ESA's Athena mission, and proposed missions such as the Arcus grating spectrometer or the Lynx observatory. These missions will have resolutions similar to, or better than, the Hitomi SXS, and will observe a large range of sources, including collisional plasmas with temperatures in the range 10^4 – 10^9 K and photo-ionized plasmas with a similarly broad range of source flux, either in ionization equilibrium or non-equilibrium. These missions will

cover a bandpass of ~ 0.1 – 10 keV, a range that includes strong lines from Fe L-shell ions (Fe XVII–Fe XXIV) as well as M-shell lines from many abundant elements.

The Hitomi SXS data have shown that accurate atomic models are just as important as calibration. Preparing for these missions will require a multifaceted approach of plasma-code testing, theoretical calculations, and laboratory measurements. The process will begin with systematic testing of existing atomic models against (1) each other, to determine where discrepancies exist, (2) laboratory measurements from electron beam ion traps and synchrotrons, and (3) deep-targeted observations with existing observatories. When areas of unresolvable disagreement are identified, new theoretical calculations may be required or targeted laboratory measurements made. The plasma-code community has already begun this work, starting with a set of agreed-upon standard tests developed at a meeting at the Lorentz Center.⁷ However, a consistent and continuous effort will be required to ensure that the community is ready for this next generation of high-resolution X-ray spectra.

Author contributions

M. Sawada, L. Gu, and J. Kaastra led this study and wrote the final manuscript along with R. K. Smith, A. R. Foster, G. V. Brown, H. Odaka, H. Akamatsu, and T. Hayashi. L. Gu, J. Kaastra, and M. Sawada performed the final SXS data reduction and spectral analysis. A. R. Foster and R. K. Smith, A. J. J. Raassen, and G. V. Brown provided inputs on APEC/AtomDB, FAC calculations, and discussion on the atomic data needs, respectively. L. Gu performed the Monte Carlo simulations for the evaluations of the systematics of the atomic data. C. A. Kilbourne contributed to the estimation of the SXS energy-scale uncertainty. R. K. Smith contributed to the discussion on the future prospects. N. Ota and M. A. Leutenegger respectively contributed to the estimations of the atomic data and plasma modeling systematics. H. Akamatsu and S. Nakashima contributed to the systematics on astrophysical models. K. Sato, H. Noda, and Y. Fukazawa contributed to the estimations of non-ICM components. S. Nakashima and M. Tsujimoto provided the data for the evaluations of the effective-area systematics. T. Hayashi confirmed the in-orbit calibration and performance of the X-ray mirrors of the SXS. N. Hell, M. Tsujimoto, and R. F. Mushotzky contributed to valuable comments on the manuscript.

The science goals of Hitomi were discussed and developed over more than ten years by the ASTRO-H Science Working Group, all members of which are authors of this manuscript. All the instruments were prepared by

joint efforts of the team. The manuscript was subject to an internal collaboration-wide review process. All authors reviewed and approved the final version of the manuscript.

Note added in proof (2018 January 23)

A new version of AtomDB (3.0.9) fixes some problems with Fe XXIV including the satellite line emissivities, and it brings the results of both codes (AtomDB and SPEX) more in line. Also, there has been released a new version of SPEX (3.04.00), although the updates have no impact on the Fe-K spectrum at the temperature range for the Perseus cluster (≈ 4 keV).

Acknowledgments

We acknowledge reviewer Paul Bryans for constructive comments and advice. We are grateful for the support from the JSPS Core-to-Core Program. We acknowledge all the JAXA members who have contributed to the ASTRO-H (Hitomi) project. All US members gratefully acknowledge support through the NASA Science Mission Directorate. Stanford and SLAC members acknowledge support via DoE contract to SLAC National Accelerator Laboratory DE-AC3-76SF00515. Part of this work was performed under the auspices of the US DoE by LLNL under Contract DE-AC52-07NA27344. Support from the European Space Agency is gratefully acknowledged. French members acknowledge support from CNES, the Centre National d'Études Spatiales. SRON is supported by NWO, the Netherlands Organization for Scientific Research. The Swiss team acknowledges the support of the Swiss Secretariat for Education, Research and Innovation (SERI). The Canadian Space Agency is acknowledged for the support of Canadian members. We acknowledge support from JSPS/MEXT KAKENHI grant numbers JP15H00773, JP15H00785, JP15H02070, JP15H02090, JP15H03639, JP15H03641, JP15H03642, JP15H05438, JP15H06896, JP15K05107, JP15K17610, JP15K17657, JP16H00949, JP16H03983, JP16H06342, JP16J02333, JP16K05295, JP16K05296, JP16K05300, JP16K05309, JP16K13787, JP16K17667, JP16K17672, JP16K17673, JP17H02864, JP17K05393, JP21659292, JP23340055, JP23340071, JP23540280, JP24105007, JP24540232, JP25105516, JP25109004, JP25247028, JP25287042, JP25400236, JP25800119, JP26109506, JP26220703, JP26400228, JP26610047, and JP26800102. The following NASA grants are acknowledged: NNX15AC76G, NNX15AE16G, NNX15AK71G, NNX15AU54G, NNX15AW94G, and NNG15PP48P to Eureka Scientific. This work was partly supported by Leading Initiative for Excellent Young Researchers, MEXT, Japan, and also by the Research Fellowship of JSPS for Young Scientists. H. Akamatsu acknowledges the support of NWO via a Veni grant. C. Done acknowledges STFC funding under grant ST/L00075X/1. A. Fabian and C. Pinto acknowledge ERC Advanced Grant 340442. P. Gandhi acknowledges JAXA International Top Young Fellowship and UK Science and Technology Funding Council (STFC) grant ST/J003697/2. Y. Ichinohe and K. Nobukawa are supported by the Research Fellow of JSPS for Young Scientists. N. Kawai is supported by the Grant-in-Aid for Scientific Research on Innovative Areas “New Developments in Astrophysics Through Multi-Messenger

⁷ See (<https://lorentzcenter.nl/lc/web/2016/830/report.pdf>).

Observations of Gravitational Wave Sources.” S. Kitamoto is partially supported by the MEXT Supported Program for the Strategic Research Foundation at Private Universities, 2014–2018. B. McNamara and S. Safi-Harb acknowledge support from NSERC. T. Dotani, T. Takahashi, T. Tamagawa, M. Tsujimoto, and Y. Uchiyama acknowledge support from the Grant-in-Aid for Scientific Research on Innovative Areas “Nuclear Matter in Neutron Stars Investigated by Experiments and Astronomical Observations.” N. Werner is supported by the Lendület LP2016-11 grant from the Hungarian Academy of Sciences. D. Wilkins is supported by NASA through Einstein Fellowship grant number PF6-170160, awarded by the Chandra X-ray Center, operated by the Smithsonian Astrophysical Observatory for NASA under contract NAS8-03060.

We acknowledge the contributions by many companies, including in particular, NEC, Mitsubishi Heavy Industries, Sumitomo Heavy Industries, and Japan Aviation Electronics Industry. Finally, we acknowledge strong support from the following engineers. JAXA/ISAS: Chris Baluta, Nobutaka Bando, Atsushi Harayama, Kazuyuki Hirose, Kosei Ishimura, Naoko Iwata, Taro Kawano, Shigeo Kawasaki, Kenji Minesugi, Chikara Natsukari, Hiroyuki Ogawa, Mina Ogawa, Masayuki Ohta, Tsuyoshi Okazaki, Shin-ichiro Sakai, Yasuko Shibano, Maki Shida, Takanobu Shimada, Atsushi Wada, and Takahiro Yamada; JAXA/TKSC: Atsushi Okamoto, Yoichi Sato, Keisuke Shinozaki, and Hiroyuki Sugita; Chubu Univ.: Yoshiharu Namba; Ehime Univ.: Keiji Ogi; Kochi Univ. of Technology: Tatsuro Kosaka; Miyazaki Univ.: Yusuke Nishioka; Nagoya Univ.: Housei Nagano; NASA/GSFC: Thomas Bialas, Kevin Boyce, Edgar Canavan, Michael DiPirro, Mark Kimball, Candace Masters, Daniel McGuinness, Joseph Miko, Theodore Muench, James Pontius, Peter Shirron, Cynthia Simmons, Gary Sneiderman, and Tomomi Watanabe; ADNET Systems: Michael Witthoef, Kristin Rutkowski, Robert S. Hill, and Joseph Eggen; Wyle Information Systems: Andrew Sargent and Michael Dutka; Noqsi Aerospace Ltd: John Doty; Stanford U/KIPAC: Makoto Asai and Kirk Gilmore; ESA (Netherlands): Chris Jewell; SRON: Daniel Haas, Martin Frericks, Philippe Laubert, and Paul Lowes; Univ. of Geneva: Philipp Azzarello; CSA: Alex Koujelev and Franco Moroso.

Appendix 1. Empirical corrections in energy scale and effective area, and data binning

A.1.1. Energy-scale correction

To obtain the energy-dependent residual energy-scale errors, we fit the strongest emission lines in the 1.9–9.5 keV band. For each line, we define an adjacent band with a width of 0.1–0.2 keV, and perform a local fit of the Hitomi SXS spectrum. Table 8 lists the principal lines for the individual bands. A collisional ionization equilibrium (CIE) model affected by redshift is used to fit the astronomical lines, whereas a redshifted double-Gaussian model is used for the instrumental Si $K\alpha$ lines. For the CIE model, the temperature is fixed to 4 keV, while the abundance, turbulent velocity, and redshift are left free. The redshift obtained from the fit is then compared with the known Perseus redshift ($z = 0.01756$ or $cz = 5264 \text{ km s}^{-1}$; Ferruit et al. 1997) to obtain the best-fit energy shifts. The rest-frame reference energies implemented in the CIE model in SPEX version

3.03 are calculated values, except for Ar XVII He α , each retrieved from the references shown in table 8. Some are not the most commonly used calculations or measurements for calibration, but the differences are usually much smaller than the statistical uncertainties in the present analysis and thus do not affect the correction results. Detailed comparisons of the reference energies are given in appendix 2 (table 9). For the instrumental Si lines, the relative normalization of the double Gaussians is fixed at the known value (Scofield 1974), and the obtained redshift is directly converted to the energy shift. As shown in figure 21 and table 8, these shifts appear to be $-(1-3) \text{ eV}$ below 4 keV and above 7 keV, and $+(0-2) \text{ eV}$ in 4–7 keV. These differences cannot be justified by an astrophysical model—the $\sim 2 \text{ eV}$ differences between the Si Ly α and Fe He α lines correspond to 300 km s^{-1} , while they are partially formed at similar temperatures. More importantly, at the high-energy side, there is several eV difference in the Rydberg series of Fe XXV, which is even harder to explain with a realistic astrophysical model. Furthermore, the energy-scale shifts at the instrumental Si $K\alpha$ lines are in good agreement with the parabolic trend of the astrophysical lines, providing further support for a non-astrophysical explanation.

The behavior of these deviations is consistent with calibration issues (M. Eckart et al. in preparation). As shown in figure 21, we perform an empirical fit using a parabolic function to the observed deviations (δE). The correction to the original energy E (keV) is given as

$$c_1 \cdot (E - E_0) + c_2 \cdot (E - E_0)^2 \text{ eV.} \quad (\text{A1})$$

E_0 is the original energy at the Fe He α line, where the shift is fixed at zero as it has already been corrected by removal of the spatial velocity gradient. The best-fit values of the coefficients are $(c_1, c_2) = (0.4062, 0.2281)$, $(0.4882, 0.2360)$, and $(0.6525, 0.2793)$ for Obs 2, 3, and 4, respectively. Similar corrections have been applied in other Hitomi Collaboration papers (Z, T, AGN, and RS papers).

We caution that this empirical correction is not to be used outside of the range of the fit or trusted at the extremes of that range. Because there is no mechanism for an offset in the energy scale, the error must eventually tend to 0 at the lowest energies.

A.1.2. Effective-area correction factor

To identify and remove any possible residual calibration errors on the effective area, which affects mostly the continuum spectrum, we incorporate two correction functions in the broad-band spectral analysis. One represents uncertainty in the thickness of the Be window of the gate valve, another the uncertainty in the effective area of the

Table 8. Emission lines used for energy-scale correction.

Ion	Principal line		Reference energy (eV)		Observed shift δE (eV)			Ref.*
	Name	Transition	Rest frame	Observer frame	Obs 2	Obs 3	Obs 4	
.....Instrumental.....								
Si I	K α_1	2p ⁻¹ (² P _{3/2})-1s ⁻¹ (² S _{1/2}) [†]	1739.99	1739.99	-2.41	-2.49	-2.22	1
.....Astronomical.....								
Si XIV	Ly α_1	1s (² S _{1/2})-2p (² P _{3/2})	2006.08	1971.44	-2.96	-2.57	-2.32	2
Si XIV	Ly β_1	1s (² S _{1/2})-3p (² P _{3/2})	2376.62	2335.58	-2.99	-2.17	-2.13	2
S XV	He α w	1s ² (¹ S ₀)-1s.2p (¹ P ₁)	2460.63	2418.14	-3.44	-1.32	-1.74	3
Si XIV	Ly γ_1	1s (² S _{1/2})-4p (² P _{3/2})	2506.37	2463.09	-0.63	-2.46	-3.37	2
S XVI	Ly α_1	1s (² S _{1/2})-2p (² P _{3/2})	2622.69	2577.40	-2.07	-1.95	-1.94	2
S XVI	Ly β_1	1s (² S _{1/2})-3p (² P _{3/2})	3106.74	3053.10	-2.13	-1.62	-2.02	2
Ar XVII	He α w	1s ² (¹ S ₀)-1s.2p (¹ P ₁)	3139.77	3085.56	-1.38	-1.60	-1.85	4
S XVI	Ly γ_1	1s (² S _{1/2})-4p (² P _{3/2})	3276.26	3219.69	-0.89	-0.38	+0.14	2
Ar XVIII	Ly α_1	1s (² S _{1/2})-2p (² P _{3/2})	3322.98	3265.60	-0.97	-0.88	-1.51	2
S XVI	Ly δ_1	1s (² S _{1/2})-5p (² P _{3/2})	3354.73	3296.81	-1.46	+0.20	-2.44	2
Ca XIX	He α w	1s ² (¹ S ₀)-1s.2p (¹ P ₁)	3902.26	3834.88	-0.48	-0.24	+0.11	5
Ar XVIII	Ly β_1	1s (² S _{1/2})-3p (² P _{3/2})	3935.71	3867.75	-0.22	-1.71	— [‡]	2
Ca XX	Ly α_1	1s (² S _{1/2})-2p (² P _{3/2})	4107.48	4036.56	+0.34	-0.34	+1.92	2
Ca XIX	He β_1	1s ² (¹ S ₀)-1s.3p (¹ P ₁)	4582.81	4503.68	+1.22	+1.86	-0.31	5
Ca XX	Ly β_1	1s (² S _{1/2})-3p (² P _{3/2})	4864.08	4780.09	+0.33	-0.64	+0.99	2
Cr XXIII	He α w	1s ² (¹ S ₀)-1s.2p (¹ P ₁)	5682.05	5583.94	+0.42	+0.73	+3.53	6
Fe XXV	He α w	1s ² (¹ S ₀)-1s.2p (¹ P ₁)	6700.42	6584.73		0 [§]		6
Fe XXVI	Ly α_1	1s (² S _{1/2})-2p (² P _{3/2})	6973.07	6852.67	-0.32	+0.60	+0.64	2
Fe XXIV	j ₃	2p (² P _{3/2})-1s.2p(³ P).3p (² D _{5/2})	7782.52	7648.14	-1.39	-2.23	-3.34	7
Ni XXVII	He α w	1s ² (¹ S ₀)-1s.2p (¹ P ₁)	7805.14	7670.37	+0.58	+0.94	-1.93	5
Fe XXV	He β_1	1s ² (¹ S ₀)-1s.3p (¹ P ₁)	7881.12	7745.04	-0.94	-1.18	-1.21	5
Fe XXV	He γ_1	1s ² (¹ S ₀)-1s.4p (¹ P ₁)	8295.39	8152.16	-1.09	-0.65	-1.54	5
Fe XXV	He δ_1	1s ² (¹ S ₀)-1s.5p (¹ P ₁)	8487.22	8340.67	-2.22	-4.77	-1.03	5

*References: (1) Bearden (1967); (2) Erickson (1977); (3) Kaufman and Martin (1993); (4) Kelly (1987); (5) Sugar and Corliss (1985); (6) Shirai et al. (2000); (7) Calculations with the Flexible Atomic Code (Gu 2008), A. J. J. Raassen (2017 private communication).

[†]A vacancy is denoted as a negative index of the electron configurations.

[‡]Poor fit. Ignored in derivation of the correction curve.

[§]The energy shift at Fe XXV He α is assumed to be zero as it is already adjusted by the removal of the spatial velocity gradient.

^{||}The 1s-3p analogous to the 1s-2p dielectronic satellite line, j: 2p (²P_{3/2})-1s.2p² (²D_{5/2}), labeled by Phillips (2008).

X-ray mirrors of the SXS. To estimate the size of these factors, the Hitomi SXS spectrum is rebinned into 100 eV bins to enhance the continuum features. We then fit it with the baseline model described in section 3 incorporating a *knak* component which determines the correction function using piecewise power laws in the energy-correction factor space, together with a neutral-Be absorption model.

By making several iterations between a fit with 100 eV-wide bins and a fit with the optimal binning (see appendix 1.3), the best-fit corrections and Be model are determined as shown with the solid curve in figure 22a. The fit prefers a negative absorption column of the Be model, which indicates that the actual thickness of the Be window might be slightly lower than the value (262 μ m) used in the current calibration. The correction, however,

approaches unity with a more realistic spectral modeling of the ICM (an improved model; see section 10), as shown with the dashed curve in figure 22a. Therefore the thinner Be window preferred with the baseline model is most likely due to incomplete modeling of the ICM emission.

The best-fit effective-area correction function is consistent with unity at ≤ 7 keV, and decreases to 0.9 at ~ 9 keV. This means that the current calibration might be underestimated by $\leq 10\%$ at the high-energy end of the standard SXS bandpass. This correction above 7 keV is more significant with an improved model. We discuss the effective-area corrections in more detail in subsection 3.4. Note that the sharp change at 7 keV is caused by the model grids: changing the grids has a negligible effect on the fitted parameters.

Table 9. Comparison of energies of emission lines used in the energy-scale correction.

Ion	Principal line	Rest-frame energy (eV)*			Deviation from SPEX (eV)			$\sigma_{\text{SXS}}^{\dagger}$ (eV)	References [‡]	
		NIST v5		Others	NIST v5		Others		NIST v5	Others
Name	Transition	Meas.	Calc.	Meas.	Meas.	Calc.	Meas.	Calc.	M, C	M, C
Si XIV	$1s\ (^2S_{1/2})-2p\ (^2P_{3/2})$	—	—	—	—	—	—	0.00	—	—, (1)
Si XIV	$1s\ (^2S_{1/2})-3p\ (^2P_{3/2})$	—	—	—	—	—	—	—	—	—, (1)
S XV	$1s^2\ (^1S_0)-1s2p\ (^1P_1)$	2460.66	2460.62	2460.63	0.03	-0.01	0.00	0.00	(2), (3)	(4), (5)
Si XIV	$1s\ (^2S_{1/2})-4p\ (^2P_{3/2})$	—	—	—	—	—	—	—	—	—, (1)
S XVI	$1s\ (^2S_{1/2})-2p\ (^2P_{3/2})$	2622.69	2622.7	2622.704	-0.1	0.0	0.01	0.0	(2), (6)	(4), (1)
S XVI	$1s\ (^2S_{1/2})-3p\ (^2P_{3/2})$	3106.74	3106.75	—	—	—	—	—	(7)	—, (1)
Ar XVII	$1s^2\ (^1S_0)-1s2p\ (^1P_1)$	3139.77	3139.585	3139.58	-0.19	-0.19	-0.19	-0.19	(8), (9)	(4), (5)
S XVI	$1s\ (^2S_{1/2})-4p\ (^2P_{3/2})$	3276.26	3276.27	—	—	—	—	—	(7)	—, (1)
Ar XVIII	$1s\ (^2S_{1/2})-2p\ (^2P_{3/2})$	3322.98	3322.993	3322.993	0.01	0.01	0.01	0.01	(10), (1)	(4), (11)
S XVI	$1s\ (^2S_{1/2})-5p\ (^2P_{3/2})$	3354.73	3354.736	—	—	—	—	—	(7)	—, (1)
Ca XIX	$1s^2\ (^1S_0)-1s2p\ (^1P_1)$	3902.26	—	3902.2	—	—	0.1	0.12	—	(12), (5)
Ar XVIII	$1s\ (^2S_{1/2})-3p\ (^2P_{3/2})$	3935.71	3935.722	—	—	—	—	—	(13)	—, (1)
Ca XX	$1s\ (^2S_{1/2})-2p\ (^2P_{3/2})$	4107.48	—	4107.5	—	—	0.0	0.0	—	(12), (1)
Ca XIX	$1s^2\ (^1S_0)-1s3p\ (^1P_1)$	4582.81	—	—	—	—	—	—	—	—, (1)
Ca XX	$1s\ (^2S_{1/2})-3p\ (^2P_{3/2})$	4864.08	—	—	—	—	—	—	—	—, (1)
Cr XXIII	$1s^2\ (^1S_0)-1s2p\ (^1P_1)$	5682.05	5681.9	5682.32	—	-0.2	0.27	0.02	(9)	(14), (5)
Fe XXV	$1s^2\ (^1S_0)-1s2p\ (^1P_1)$	6700.42	6700.0	6700.55	—	-0.4	0.13	0.02	(9)	(15), (5)
Fe XXVI	$1s\ (^2S_{1/2})-2p\ (^2P_{3/2})$	6973.07	6973.179	6972.7348	—	0.11	-0.34	0.11	(16)	(17), (1)
Fe XXIV	$2p\ (^2P_{3/2})-1s2p\ (^2P_{3/2}).3p\ (^2D_{5/2})$	7782.52	—	7781.6	—	—	-0.9	0.1	(18)	(18), (18)
Ni XXVIII	$1s^2\ (^1S_0)-1s2p\ (^1P_1)$	7805.14	—	7804.6	—	—	-0.5	0.0	(9)	(19), (20)
Fe XXV	$1s^2\ (^1S_0)-1s3p\ (^1P_1)$	7881.12	7881.17	7880.67	—	0.05	-0.45	-0.1	(16)	(18), (18)
Fe XXV	$1s^2\ (^1S_0)-1s4p\ (^1P_1)$	8295.39	8295.48	8295.64	—	0.09	0.25	—	(16)	(21), (1)
Fe XXV	$1s^2\ (^1S_0)-1s5p\ (^1P_1)$	8487.22	8487.3	8487.36	—	0.1	0.14	—	(16)	(14), (1)

*Line energies in SPEX v3.03 and measured and calculated values in the NIST Atomic Spectra Database v5.3⁷ and those in other calibration standards.[†]Statistical errors in line energy shift measurements with the Hitomi SXS. Those of the three observations (Obs 2, 3, and 4) are averaged by taking root mean squares.[‡]References for the measured (M) and calculated (C) values in NIST v5 and those in other results: (1) Johnson and Soff (1985); (2) Schlenker et al. (1982); (3) Aglitsky et al. (1988); (4) Kubiček et al. (2014); (5) Arsenyev et al. (2005); (6) Aglitskii et al. (1974); (7) Kaufman and Martin (1993); (8) Bruhns et al. (2007); (9) NIST Atomic Spectra Database⁷; (10) Beyer et al. (1985); (11) Yerokhin and Shabaev (2015); (12) Rice et al. (2014); (13) Erickson (1977); (14) Beiersdorfer et al. (1989); (15) Rudolph et al. (2013); (16) Shirai et al. (2000); (17) Chantler et al. (2007); (18) Smith et al. (1993); (19) Bombarda et al. (1988); (20) Natarajan and Kadrekar (2013); (21) Indelicato et al. (1986).[§]For the references for the line energies in SPEX version 3.03, see table 8.^{||}The 1s–3p analogous to the 1s–2p DR satellite line, i; 2p ($^2P_{3/2}$) – 1s ($2p^2\ (^2D_{5/2})$), labeled by Phillips (2008).

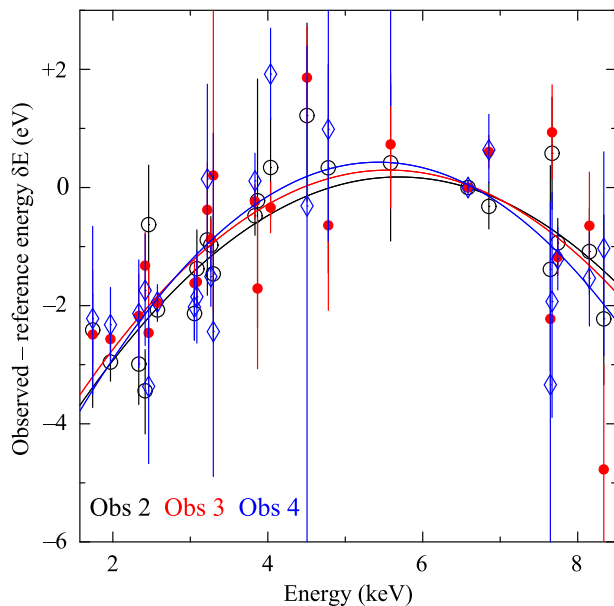


Fig. 21. The differences between measured and reference energies of the brightest lines (see table 8 for details). The curves show the best-fit parabolic functions of the three observations. (Color online)

A.1.3. Binning of the data

For the binning of our X-ray data, we have followed the approach of Kaastra and Bleeker (2016) for optimal binning. The optimal bin size depends on the spectral resolution, number of resolution bins, and local intensity of the spectrum, and is different for each energy. It is achieved by issuing the *obin* command in SPEX. Since we started with a spectrum with a 0.5 eV resolution bin, our optimal bin size is a multiple of 0.5 eV. In practice, for most energies below 8.2 keV we use a bin size of 1.5 eV, and for higher energies 2 eV. The exceptions are near the SXV He α complex, where we use 1 eV, and near the high- n transition lines of Fe xxv, including He γ , He δ , and He ϵ lines, where we also use 1.5 eV data bins.

Appendix 2. Reference line energies for the energy-scale correction

Table 9 compares the reference energies of emission lines in SPEX used in the SXS energy-scale correction (appendix 1.1) to the NIST Atomic Spectra Database version 5.3⁸ and other available measurements and calculations.

In the case of hydrogenic ions, we use the calculations of Erickson (1977). This is in contrast to Hitomi Collaboration (2016), where for H-like Fe xxvi the calculations of Johnson and Soff (1985) were used. The up-to-date

⁸ Kramida, A., Ralchenko, Y., Reader, J., and NIST ASD Team. 2015, NIST Atomic Spectra Database (<http://physics.nist.gov/asd>).

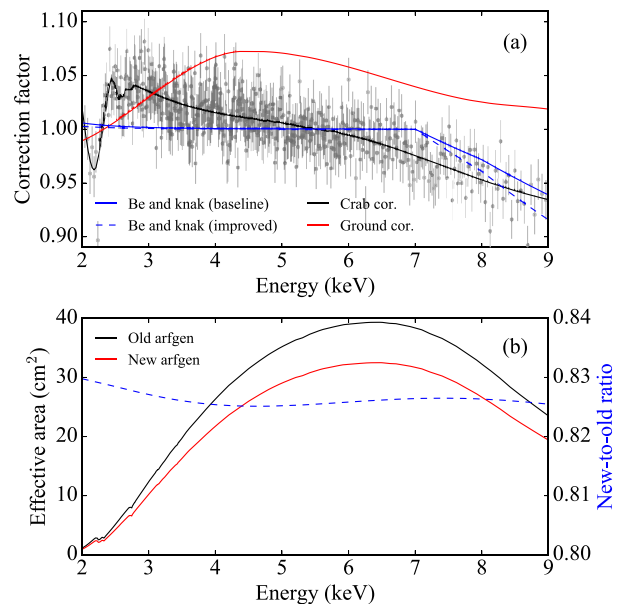


Fig. 22. (a) Comparison of effective area correction factors: the original correction (blue) for each of the baseline and improved models respectively in solid and dashed curves, the on-ground calibration correction (red), and the Crab correction (black) derived by smoothing the SXS-to-canonical ratio (gray crosses: M. Tsujimoto 2017 private communication). For the Crab analysis, high-primary as well as mid-primary grade events are used. (b) Effective area with the old and the new *arfgen* in black and red, respectively, as well as the ratio of the two calculations with the dashed blue curve. (Color online)

calculations of Yerokhin and Shabaev (2015) agree well with Johnson and Soff (1985). Although Johnson and Soff (1985) are the accepted standard for $n = 2$ to 1 transitions in H-like ions (Ly α) and have been well tested (Beiersdorfer 2009), they do not include transitions from higher Rydberg states with $n \geq 3$. The calculations are in good agreement between Erickson (1977) and Johnson and Soff (1985) within 0.02 eV for $Z \leq 20$. For Ly α_1 of Fe xxvi, Erickson (1977) is 0.11 eV less. For consistency, we use the values from Erickson (1977).

For $n = 2$ to 1 transitions in He-like ions (He α) of Cr and Fe, Ca and Ni, and S, we respectively use the calculated values of Shirai et al. (2000), Sugar and Corliss (1985), and Kaufman and Martin (1993). For Ar He α , we use the measurement of Kelly (1987). These values are in good agreement within 0.2 eV with the calculations of Artemyev et al. (2005), as well as Cheng et al. (1994). An exception is found in the Ni He α line, whose deviation is +0.47 eV. A recent update by Natarajan and Kadrekar (2013) gives a better agreement for Ni He α with the SPEX value. These calculations have also been compared to many measured values (Beiersdorfer & Brown 2015), and good agreement is found. We also note the work of Drake (1988), which has often been used as a calibration standard.

For the 1s–3p transitions of Fe XXV (He β_1) and Fe XXIV (j_3 satellite in Phillips 2008), we respectively use the calculation of Sugar and Corliss (1985) and a FAC calculation (A. J. J. Raassen 2017 private communication). Smith et al. (1993) performed both calculations and measurements of these 1s–3p lines of Fe ions. The calculated values are in good agreement with those used in SPEX within 0.1 eV. On the other hand, the measured values have relatively large deviations (−0.45 and −0.9 eV, respectively) from the calculations, which may be due to the limited wavelength calibration of the crystal spectrometer, as noted in Smith et al. (1993).

For the other high- n Rydberg series (Ca XIX He β and Fe XXV He β – δ), we use the calculated values from Sugar and Corliss (1985). Measurements of the high- n lines of He-like Fe XXV have been conducted by Indelicato et al. (1986) and Beiersdorfer et al. (1989), respectively. These agree well with the SPEX values within the measurement errors (± 0.15 eV for He γ_1 and ± 0.22 eV for He δ_1).

Appendix 3. Systematic factors due to instrumental effects

In this section we discuss the effects of several aspects of the instrumental calibrations on the derived parameters.

A.3.1. Velocity-gradient correction

The line broadening due to spatial bulk velocity of the ICM is removed by applying an energy-scale correction to each pixel (section 2). Without this correction, the C-statistic obtained with the baseline model increases by $\delta C_{\text{stat}} = 62$, and the LOS turbulent velocity dispersion becomes larger by 13 km s^{-1} (“No vel. cor.” in table 1). The best-fit line center shifts toward shorter wavelength by 23 km s^{-1} .

A.3.2. Response matrices

We also test how much the fit changes by using a small RMF with only the Gaussian core component, as well as by using an extra-large RMF with the electron-loss continuum.⁹ As shown in table 1, a small RMF improves the baseline fit by $\delta C_{\text{stat}} = 4$, while an extra-large RMF (listed as “XL RMF”) gives instead a poorer fit with $\delta C_{\text{stat}} = 12$. The changes on the best-fit temperature and abundances by the RMF-type selection are 1%–2%.

⁹ The current version of SPEX (3.03) is not fully compatible with the extra-large-size RMF because of its complexity. Here we apply a local fix to the incompatibility, which will be publicly available in the next release (version 3.04 or later).

A.3.3. Non-X-ray background

The NXB rate depends on the orbital history of the satellite. Although this effect is already taken into account in `sxsnxbgen`, the systematic uncertainty could be large if the orbital history is biased. In the case of the Perseus observations (Obs 2–4), this systematic is expected to be small as the on-source time (≈ 290 ks) is much longer than the satellite orbital period. Indeed, the estimated NXB rate is $3.0 \times 10^{-2} \text{ counts s}^{-1} \text{ cm}^{-2}$ in 1.0–10 keV, consistent with the orbit-averaged value (Kilbourne et al. 2018). This converts to 0.4% of the total count rate of the source events in 1.9–9.5 keV. Here, we consider an extreme case where we completely ignore the NXB contribution. As shown in table 1, the baseline run without the NXB component gives a larger C-statistic value ($\delta C_{\text{stat}} = 9$) than the original run, and the impact on the fitting parameters is minor, $\leq 1\%$ on temperature and abundances.

A.3.4. Effective area

A.3.4.1. Point-source ARFs

The spatial extent of the target has an impact on the instrumental response. As shown in table 1 (labeled as “PS ARF”), the use of the point-source ARFs not only on the AGN component but also on the ICM component of the Perseus cluster gives a larger C-statistic value ($\delta C_{\text{stat}} = 30$) than the original baseline fit. The improper ARF would lead to a 1% bias on temperature and up to 5% biases on abundances.

A.3.4.2. No effective-area correction factor

The correction factor (appendix 1.2) is included to remove potential calibration uncertainties on the effective area. As shown in table 1 (labeled as “No ARF cor.”), ignoring the correction factor yields a poorer fit ($\delta C_{\text{stat}} = 38$). The temperature shifts by 0.08 keV from the original value, and several abundances are underestimated by 0.03 times solar. The emission measure changes by 1.3%, larger than the statistical error by a factor of five. This indicates that the correction factor, despite being small, is still needed for the current calibration.

A.3.4.3. Correction factor based on on-ground calibration

The baseline effective area correction is done with the SPEX model *knak*. Alternatively, the correction can be achieved by setting `auxtransfile=CALDB` in the `aharfgen` run, which applies an additional empirical transmission on the original ARFs. With this correction, the discrepancy in the mirror effective area between on-ground calibration measurements and ray-tracing simulations is removed. We hence rerun the baseline fit by including the new correction factor while turning off the *knak* and Be-filter



Fig. 23. XXS spectrum of the Perseus cluster in 1.9–4.7 keV fitted with different models. Panels in each subfigure show (upper) fit to the data with the baseline model, (middle) relative difference between the baseline model and the best-fit models with APEC v3.0.8 in blue, SPEX v2 in red, and CHIANTI v8.0 in green, and (lower) significances in σ of an additional *line* model at each energy on top of the baseline model in black and improved model in gray. (Color online)



Fig. 24. Same as figure 23, but in 4.7–7.4 keV. (Color online)

Table 10. Comparisons of energies, transition probabilities, and emissivities of Lyman- and helium-series lines for flux calculation.

Name	E (keV)*				f_E^\dagger	$\log_{10} A$ (s $^{-1}$)*			f_A^\dagger	ε (10 $^{-23}$ m 3 s $^{-1}$)*			f_ε^\dagger
	S3	A	S2	C	(%)	S3	A	C	(%)	S3	A	C	(%)
Si xiv Ly α_2	2.00432	2.00432	2.00395	2.00434	0.008	13.3827	13.3811	13.3831	0.2	0.905	0.856	1.140	12.8
Si xiv Ly α_1	2.00608	2.00608	2.00589	2.00609	0.004	13.3836	13.3822	13.3845	0.2	1.808	1.706	2.270	12.7
Si xiv Ly β_2	2.37610	2.37610	2.37518	2.37609	0.017	12.8096	12.8061	12.8098	0.4	0.147	0.132	0.150	5.5
Si xiv Ly β_1	2.37662	2.37662	(2.37518)	2.37663	0.026	12.8099	12.8094	12.8106	0.1	0.294	0.264	0.300	5.5
Si xiv Ly γ_2	2.50615	2.50615	2.50473	2.50615	0.025	12.4201	12.4156	12.4201	0.5	0.054	0.044	0.048	8.4
Si xiv Ly γ_1	2.50637	2.50637	(2.50473)	2.50635	0.028	12.4200	12.4198	12.4209	0.1	0.108	0.089	0.095	8.1
Si xiv Ly δ_2	2.56632	2.56632	2.56696	2.56632	0.011	12.1225	12.1176	12.1229	0.6	0.026	0.020	0.021	11.8
Si xiv Ly δ_1	2.56643	2.56643	(2.56696)	2.56643	0.009	12.1225	12.1222	12.1235	0.1	0.052	0.041	0.043	10.6
Si xiv Ly ε_2	2.59899	2.59899	2.59925	—	0.005	11.8815	11.8764	—	0.6	0.013	0.011	—	8.3
Si xiv Ly ε_1	2.59905	2.59906	(2.59925)	—	0.004	11.8815	11.8812	—	0.0	0.026	0.022	—	8.3
Si xiv Ly ζ_2	2.61868	2.61869	—	—	0.000	11.6759	11.6732	—	0.3	0.008	0.007	—	6.7
Si xiv Ly ζ_1	2.61872	2.61873	—	—	0.000	11.6760	11.6781	—	0.2	0.016	0.013	—	10.3
P xv Ly α_2	2.30165	2.30165	—	2.30163	0.000	13.5030	13.4991	13.5032	0.4	0.009	0.009	0.011	9.8
P xv Ly α_1	2.30396	2.30396	—	2.30394	0.000	13.5039	13.5005	13.5047	0.4	0.019	0.018	0.022	8.6
S xvi Ly α_2	2.61969	2.61969	2.61957	2.61968	0.002	13.6153	13.6110	13.6157	0.5	0.580	0.524	0.684	11.1
S xvi Ly α_1	2.62269	2.62269	2.62179	2.62267	0.015	13.6165	13.6125	13.6173	0.5	1.160	1.044	1.370	11.3
S xvi Ly β_2	3.10585	3.10585	3.10737	3.10582	0.021	13.0422	13.3365	13.0426	34.5	0.091	0.079	0.089	6.1
S xvi Ly β_1	3.10674	3.10674	(3.10737)	3.10675	0.009	13.0426	13.3387	13.0434	34.7	0.183	0.158	0.179	6.3
S xvi Ly γ_2	3.27589	3.27589	3.28001	3.27584	0.055	12.6527	12.6376	12.6528	1.6	0.032	0.026	0.028	8.7
S xvi Ly γ_1	3.27626	3.27626	(3.28001)	3.27628	0.049	12.6527	12.6377	12.6536	1.7	0.065	0.053	0.057	8.6
S xvi Ly δ_2	3.35454	3.35454	3.35093	3.35455	0.047	12.3553	12.6419	12.3555	33.6	0.016	0.012	0.013	12.4
S xvi Ly δ_1	3.35473	3.35473	(3.35093)	3.35473	0.049	12.3553	12.3328	12.3562	2.5	0.032	0.024	0.025	13.2
S xvi Ly ε_2	3.39724	3.39731	3.39683	—	0.006	12.1143	12.0824	—	3.7	0.008	0.006	—	14.3
S xvi Ly ε_1	3.39724	3.39742	(3.39683)	—	0.007	12.1143	12.0824	—	3.7	0.016	0.013	—	10.3
S xvi Ly ζ_2	3.42298	3.42305	—	—	0.001	11.9076	11.8666	—	4.7	0.005	0.004	—	11.1
S xvi Ly ζ_1	3.42298	3.42312	—	—	0.002	11.9077	11.8666	—	4.7	0.010	0.008	—	11.1
Cl xvii Ly α_2	2.95851	2.95853	—	2.95849	0.001	13.7210	13.7159	13.7214	0.6	0.008	0.014	0.009	25.4
Cl xvii Ly α_1	2.96234	2.96235	—	2.96230	0.001	13.7223	13.7177	13.7231	0.6	0.016	0.027	0.018	23.5
Cl xvii Ly β_2	3.50770	3.50771	—	3.50773	0.000	13.1480	13.4411	13.1483	34.4	0.001	0.002	0.001	35.4
Cl xvii Ly β_1	3.50884	3.50884	—	3.50882	0.000	13.1483	13.4437	13.1489	34.6	0.003	0.004	0.002	27.2
Ar xviii Ly α_2	3.31816	3.31816	3.31775	3.31775	0.006	13.8207	13.8149	13.8191	0.6	0.160	0.148	0.150	3.4
Ar xviii Ly α_1	3.32298	3.32298	3.32308	3.32308	0.002	13.8221	13.8168	13.8165	0.6	0.320	0.294	0.270	6.9
Ar xviii Ly β_2	3.93428	3.93428	3.93601	3.93426	0.019	13.2475	13.5397	13.2435	34.5	0.024	0.022	0.018	11.7
Ar xviii Ly β_1	3.93571	3.93571	(3.93601)	3.93576	0.003	13.2480	13.5427	13.2438	34.8	0.049	0.044	0.036	12.5
Ar xviii Ly γ_2	4.14973	4.14973	—	4.14968	0.001	12.8581	12.8387	12.8532	1.9	0.008	0.007	0.006	11.7
Ar xviii Ly γ_1	4.15033	4.15033	—	4.15038	0.001	12.8581	12.8388	12.8550	1.9	0.017	0.015	0.011	17.4
Ar xviii Ly δ_2	4.24936	4.24936	—	4.24938	0.000	12.5606	12.5319	12.5547	2.8	0.004	0.003	0.003	14.1
Ar xviii Ly δ_1	4.24967	4.24967	—	4.24967	0.000	12.5607	12.5319	12.5565	2.9	0.008	0.007	0.005	18.7
K xix Ly α_2	3.69868	3.69869	—	3.69870	0.000	13.9150	13.9084	13.9152	0.7	0.006	0.006	0.007	7.4
K xix Ly α_1	3.70466	3.70468	—	3.70467	0.000	13.9165	13.9105	13.9173	0.7	0.013	0.012	0.014	6.3
Ca xx Ly α_2	4.10012	4.10012	4.10069	4.10014	0.006	14.0043	13.9971	14.0048	0.8	0.095	0.089	0.103	6.0
Ca xx Ly α_1	4.10748	4.10748	4.10748	4.10748	0.000	14.0060	13.9994	14.0069	0.8	0.190	0.177	0.206	6.2
Ca xx Ly β_2	4.86190	4.86190	4.88127	4.86193	0.172	13.4315	13.7214	13.4317	34.0	0.014	0.013	0.013	3.5
Ca xx Ly β_1	4.86408	4.86408	(4.88127)	4.86403	0.153	13.4320	13.7250	13.4328	34.3	0.028	0.026	0.027	3.0
Ca xx Ly γ_2	5.12822	5.12822	5.16601	5.12819	0.319	13.0418	13.0179	13.0422	2.6	0.005	0.004	0.004	10.9
Ca xx Ly γ_1	5.12914	5.12914	(5.16601)	5.12925	0.310	13.0422	13.0179	13.0430	2.7	0.009	0.008	0.008	5.7
Ca xx Ly δ_2	5.25136	5.25136	5.39062	5.25134	1.141	12.7445	12.7087	12.7447	3.8	0.002	0.002	0.002	0.0
Ca xx Ly δ_1	5.25183	5.25183	(5.39062)	5.25179	1.137	12.7446	12.7088	12.7455	3.9	0.005	0.004	0.004	10.9
Ti xxii Ly α_2	4.96605	4.96609	—	—	0.000	14.1708	14.1617	—	1.1	0.002	0.002	—	0.0
Ti xxii Ly α_1	4.97685	4.97689	—	—	0.000	14.1729	14.1647	—	0.9	0.005	0.004	—	11.1
Cr xxiv Ly α_2	5.91644	5.91650	—	—	0.001	14.3230	14.3120	—	1.3	0.005	0.005	—	0.0
Cr xxiv Ly α_1	5.93178	5.93185	—	—	0.001	14.3253	14.3153	—	1.1	0.011	0.009	—	10.0

Table 10. (Continued)

Name	E (keV)*				f_E^\dagger	$\log_{10} A$ (s $^{-1}$)*			f_A^\dagger	ε (10 $^{-23}$ m 3 s $^{-1}$)*			f_ε^\dagger
	S3	A	S2	C	(%)	S3	A	C	(%)	S3	A	C	(%)
Mn xxv Ly α_2	6.42349	6.42356	—	—	0.001	14.3945	14.3824	—	1.4	0.002	0.001	—	33.3
Mn xxv Ly α_1	6.44159	6.44166	—	—	0.001	14.3971	14.3860	—	1.3	0.004	0.003	—	14.3
Fe xxvi Ly α_2	6.95186	6.95186	6.95186	6.95212	0.002	14.4630	14.4499	14.4634	1.4	0.100	0.099	0.114	6.6
Fe xxvi Ly α_1	6.97307	6.97307	6.97307	6.97324	0.001	14.4658	14.4538	14.4667	1.4	0.209	0.194	0.212	3.8
Fe xxvi Ly β_2	8.24629	8.24629	8.25051	8.24637	0.022	13.8904	14.1720	13.8906	33.0	0.012	0.013	0.015	9.4
Fe xxvi Ly β_1	8.25258	8.25258	(8.25051)	8.25241	0.011	13.8911	14.1781	13.8919	33.6	0.023	0.025	0.027	6.5
Fe xxvi Ly γ_2	8.69847	8.69847	8.70004	8.69881	0.007	13.5009	13.4589	13.5011	4.5	0.004	0.004	0.004	0.0
Fe xxvi Ly γ_1	8.70112	8.70113	(8.70004)	8.70126	0.006	13.5011	13.4592	13.5020	4.5	0.008	0.008	0.008	0.0
Fe xxvi Ly δ_2	8.90740	8.90740	8.90831	8.90755	0.004	13.2036	13.4651	13.2036	30.5	0.002	0.002	0.002	0.0
Fe xxvi Ly δ_1	8.90876	8.90876	(8.90831)	8.90883	0.002	13.2036	13.1411	13.2044	6.7	0.005	0.004	0.004	10.9
Fe xxvi Ly ε_2	9.02074	9.02104	9.02076	—	0.002	12.9624	12.8740	—	10.1	0.001	0.001	—	0.0
Fe xxvi Ly ε_1	9.02076	9.02182	(9.02076)	—	0.006	12.9624	12.8739	—	10.2	0.002	0.002	—	0.0
Fe xxvi Ly ζ_2	9.08901	9.08931	—	—	0.002	12.7490	12.6348	—	13.1	0.001	0.001	—	0.0
Fe xxvi Ly ζ_1	9.08902	9.08980	—	—	0.004	12.7490	12.6347	—	13.1	0.001	0.001	—	0.0
Ni xxviii Ly α_2	8.07296	8.07420	8.07296	8.07294	0.007	14.5930	14.5775	14.5933	1.7	0.002	0.002	0.002	0.0
Ni xxviii Ly α_1	8.10160	8.10160	8.10160	8.10195	0.002	14.5962	14.5821	14.5970	1.6	0.004	0.003	0.004	12.9
Ni xxviii Ly β_2	9.57743	9.57743	9.58359	9.57777	0.027	14.0204	14.2986	14.0208	32.6	0.0002	0.0002	0.0002	0.0
Ni xxviii Ly β_1	9.58592	9.58592	(9.58359)	9.58591	0.011	14.0212	13.9916	14.0220	3.2	0.0005	0.0004	0.0005	10.1
S xv He α z	2.43035	2.43035	2.42631	2.43035	0.072	6.1553	6.1206	6.1553	3.7	0.084	0.083	0.061	14.0
S xv He α y	2.44714	2.44714	2.44704	2.44714	0.002	11.7686	11.6702	11.6826	10.4	0.026	0.026	0.021	9.7
S xv He α x	2.44876	2.44876	—	2.44878	0.000	8.0755	8.0682	8.0755	0.8	0.012	0.012	0.010	8.3
S xv He α w	2.46063	2.46063	2.46054	2.46064	0.002	13.8180	13.8261	13.8242	0.8	0.294	0.255	0.269	5.9
S xv He β_2	2.88022	2.88022	2.87667	2.88021	0.053	11.2098	11.1644	11.1898	4.3	0.0010	0.0010	0.0006	21.8
S xv He β_1	2.88392	2.88403	(2.87667)	2.88396	0.110	13.2591	13.2672	13.2651	0.8	0.047	0.044	0.043	3.8
S xv He γ_2	3.03099	3.03099	3.02401	3.03095	0.100	10.8455	10.7853	10.8307	5.8	0.0002	0.0002	0.0002	0.0
S xv He γ_1	3.03251	3.03266	(3.02401)	3.03251	0.122	12.8721	12.8785	12.8779	0.7	0.017	0.016	0.015	5.1
Ar xvii He α z	3.10435	3.10414	3.107374	3.10426	0.044	6.6812	6.6484	6.6473	3.7	0.051	0.050	0.041	9.5
Ar xvii He α y	3.12374	3.12353	3.12303	3.12374	0.009	12.2601	12.1644	12.2235	9.0	0.019	0.018	0.016	7.1
Ar xvii He α x	3.12647	3.12628	—	3.12673	0.006	8.4997	8.4940	8.5068	1.2	0.013	0.013	0.011	7.6
Ar xvii He α w	3.13977	3.13958	3.13884	3.13940	0.011	14.0302	14.0374	14.0527	2.2	0.178	0.161	0.166	4.2
Ar xvii He β_2	3.67961	3.67943	3.70102	3.67938	0.253	11.6984	11.6551	11.7005	4.7	0.0010	0.0010	0.0007	15.7
Ar xvii He β_1	3.68404	3.68452	(3.70102)	3.68233	0.205	13.4642	13.4742	13.5406	8.0	0.027	0.026	0.025	3.1
Ar xvii He γ_2	3.87301	3.87301	—	3.87305	0.000	11.3328	11.2718	11.3422	7.0	0.0003	0.0002	0.0002	20.2
Ar xvii He γ_1	3.87504	3.87451	—	3.87487	0.006	13.0730	13.0792	13.2443	19.3	0.010	0.009	0.008	9.1
K xviii He α z	3.47218	3.47229	—	3.47217	0.002	6.9229	6.8899	6.9188	3.3	0.003	0.004	0.002	27.2
K xviii He α y	3.49297	3.49302	—	3.49301	0.001	12.4800	12.3874	12.4806	9.7	0.0010	0.0010	0.0008	10.1
K xviii He α x	3.49646	3.49654	—	3.49645	0.001	8.6940	8.6890	8.6923	0.5	0.0010	0.0010	0.0006	21.8
K xviii He α w	3.51036	3.51051	—	3.51031	0.002	14.1258	14.1335	14.1294	0.7	0.011	0.010	0.010	4.6
Ca xix He α z	3.86114	3.86120	3.85871	3.86111	0.027	7.1523	7.1173	7.1523	3.7	0.066	0.069	0.058	7.2
Ca xix He α y	3.88332	3.88331	3.88118	3.88336	0.024	12.6848	12.5944	12.6022	9.7	0.028	0.038	0.037	13.1
Ca xix He α x	3.88770	3.88775	3.88544	3.88775	0.026	8.8779	8.8736	8.8779	0.5	0.024	0.027	0.025	4.9
Ca xix He α w	3.90226	3.90237	3.90219	3.90243	0.002	14.2156	14.2227	14.2214	0.7	0.226	0.236	0.241	2.7
Ca xix He β_2	4.57753	4.57753	4.59201	4.57760	0.137	12.1565	12.0792	12.1014	7.6	0.002	0.002	0.002	0.0
Ca xix He β_1	4.58281	4.58352	(4.59201)	4.58284	0.085	13.6437	13.6551	13.6542	1.2	0.033	0.038	0.038	6.5
Ca xix He γ_2	4.81941	4.81941	4.76863	4.81941	0.457	11.7916	11.6893	11.7362	9.7	0.0010	0.0010	0.0005	28.3
Ca xix He γ_1	4.82158	4.82241	(4.76863)	4.82166	0.480	13.2529	13.2577	13.2608	0.8	0.011	0.012	0.012	4.0
Ca xix He δ_2	4.93107	4.93107	4.95937	4.93116	0.248	11.4986	11.3522	11.4456	13.6	0.0003	0.0002	0.0002	20.2
Ca xix He δ_1	4.93217	4.93175	(4.95937)	4.93214	0.240	12.9553	12.9294	12.9549	2.8	0.005	0.005	0.005	0.0
Ti xxi He α z	4.70196	4.70196	—	—	0.000	7.5755	7.5428	—	3.8	0.003	0.003	—	0.0
Ti xxi He α y	4.72693	4.72693	—	—	0.000	13.0326	12.9657	—	7.7	0.002	0.002	—	0.0
Ti xxi He α x	4.73379	4.73379	—	—	0.000	9.2193	9.2159	—	0.4	0.002	0.001	—	33.3
Ti xxi He α w	4.74963	4.74963	—	—	0.000	14.3798	14.3874	—	0.9	0.012	0.010	—	9.1
Cr xxiii He α z	5.62691	5.62691	—	—	0.000	7.9622	7.9304	—	3.7	0.017	0.019	—	5.6

Table 10. (Continued)

Name	E (keV)*				f_E^\dagger (%)	$\log_{10} A$ (s ⁻¹)*			f_A^\dagger (%)	ε (10 ⁻²³ m ³ s ⁻¹)*			f_ε^\dagger (%)
	S3	A	S2	C		S3	A	C		S3	A	C	
Cr XXIII He α y	5.65484	5.65484	—	—	0.000	13.3458	13.2900	—	6.4	0.010	0.009	—	5.3
Cr XXIII He α x	5.66506	5.66506	—	—	0.000	9.5306	9.5278	—	0.3	0.009	0.009	—	0.0
Cr XXIII He α w	5.68205	5.68205	—	—	0.000	14.5271	14.5353	—	0.9	0.056	0.049	—	6.7
Cr XXIII He β_2	6.67313	6.67313	—	—	0.000	12.8927	12.7559	—	15.6	0.001	0.001	—	0.0
Cr XXIII He β_1	6.68077	6.68077	—	—	0.000	13.9577	13.9600	—	0.3	0.008	0.007	—	6.7
Mn XXIV He α z	6.12105	6.12113	—	—	0.001	8.1436	8.1106	—	3.8	0.011	0.008	—	15.8
Mn XXIV He α y	6.15071	6.15057	—	—	0.001	13.4933	13.4346	—	6.8	0.007	0.004	—	27.3
Mn XXIV He α x	6.16284	6.16290	—	—	0.000	9.6765	9.6739	—	0.3	0.006	0.004	—	20.0
Mn XXIV He α w	6.18019	6.18044	—	—	0.002	14.5949	14.6042	—	1.1	0.034	0.022	—	21.4
Mn XXIV He β_2	7.25981	7.25983	—	—	0.000	13.0406	12.8965	—	16.4	0.001	0.000	—	17.6
Mn XXIV He β_1	7.26822	7.26826	—	—	0.000	14.0278	14.0253	—	0.3	0.004	0.003	—	14.3
Fe XXV He α z	6.63660	6.63658	6.63652	6.63656	0.000	8.3181	8.2856	8.3181	3.5	0.826	0.737	0.758	4.9
Fe XXV He α y	6.66757	6.66755	6.66777	6.66761	0.001	13.6294	13.5705	13.6385	6.8	0.544	0.474	0.516	5.6
Fe XXV He α x	6.68233	6.68230	6.68220	6.68234	0.001	9.8162	9.8142	9.8116	0.4	0.491	0.442	0.472	4.3
Fe XXV He α w	6.70042	6.70040	6.70011	6.70076	0.003	14.6594	14.6693	14.6637	0.9	2.568	2.197	2.440	6.4
Fe XXV He β_2	7.87185	7.87202	7.88112	7.87201	0.050	13.1830	13.0253	13.0515	16.6	0.062	0.047	0.051	11.9
Fe XXV He β_1	7.88112	7.88152	(7.88112)	7.88102	0.002	14.0934	14.0899	14.0885	0.5	0.328	0.293	0.316	4.6
Fe XXV He γ_2	8.29154	8.29160	8.29539	8.29159	0.020	12.7757	12.6191	12.6732	15.3	0.019	0.014	0.015	13.5
Fe XXV He γ_1	8.29539	8.29548	(8.29539)	8.29548	0.001	13.7029	13.6776	13.6845	2.5	0.102	0.092	0.099	4.3
Fe XXV He δ_2	8.48526	8.48510	8.48722	8.48509	0.011	12.4947	12.2430	12.3698	23.4	0.008	0.006	0.006	14.1
Fe XXV He δ_1	8.48722	8.48742	(8.48722)	8.48742	0.001	13.4052	13.3139	13.3662	8.5	0.045	0.041	0.043	3.8
Fe XXV He ε_2	8.59032	8.58733	—	—	0.017	12.2492	12.1199	—	14.8	0.004	0.004	—	0.0
Fe XXV He ε_1	8.59145	8.58848	—	—	0.017	13.2188	13.1086	—	12.6	0.024	0.024	—	0.0
Fe XXV He ζ_2	8.65361	8.65058	—	—	0.018	12.0558	11.8927	—	18.6	0.003	0.002	—	20.0
Fe XXV He ζ_1	8.65433	8.65130	—	—	0.018	13.0166	12.8733	—	16.4	0.015	0.014	—	3.4
Fe XXV He η_2	8.69451	8.69158	—	—	0.017	11.8935	11.6734	—	24.8	0.002	0.001	—	33.3
Fe XXV He η_1	8.69499	8.69206	—	—	0.017	12.8416	12.6465	—	22.1	0.010	0.009	—	5.3
Fe XXV He θ_2	8.72260	8.71967	—	—	0.017	11.7612	11.4252	—	36.9	0.001	0.001	—	0.0
Fe XXV He θ_1	8.72294	8.72001	—	—	0.017	12.6870	12.3902	—	32.9	0.006	0.006	—	0.0
Fe XXV He ι_2	8.74267	8.73975	—	—	0.017	11.6770	10.9255	—	69.9	0.001	0.001	—	0.0
Fe XXV He ι_1	8.74292	8.73999	—	—	0.017	12.5488	11.8781	—	64.8	0.004	0.004	—	0.0
Co XXVI He α z	7.17332	7.18465	—	—	0.079	8.4864	8.4533	—	3.8	0.002	—	—	—
Co XXVI He α y	7.20619	7.21658	—	—	0.072	13.7560	13.6972	—	6.8	0.001	—	—	—
Co XXVI He α x	7.22341	7.23461	—	—	0.077	9.9498	9.9490	—	0.1	0.001	—	—	—
Co XXVI He α w	7.24173	7.25408	—	—	0.085	14.7208	14.7308	—	1.1	0.006	—	—	—
Ni XXVII He α z	7.73153	7.73161	7.73162	7.73162	0.000	8.6484	8.6138	8.6484	3.7	0.031	0.032	0.029	4.1
Ni XXVII He α y	7.76605	7.76567	7.77867	7.76600	0.071	13.8745	13.8149	13.8171	6.5	0.022	0.021	0.022	2.2
Ni XXVII He α x	7.78637	7.78642	—	7.78649	0.001	10.0792	10.0788	10.0792	0.0	0.020	0.019	0.020	2.4
Ni XXVII He α w	7.80514	7.80556	7.80511	7.80511	0.002	14.7795	14.7903	14.7893	1.1	0.091	0.081	0.088	4.8
Ni XXVII He β_2	9.17227	9.17043	9.18358	9.17246	0.057	13.3863	13.2625	13.2869	12.7	0.003	0.002	0.002	20.2
Ni XXVII He β_1	9.18359	9.18402	(9.18358)	9.18333	0.003	14.2135	14.2068	14.2057	0.8	0.011	0.010	0.011	4.4
Ni XXVII He γ_2	9.66241	9.66362	9.66712	9.66211	0.021	12.9997	12.8451	12.9032	14.9	0.0008	0.0006	0.0006	14.1
Ni XXVII He γ_1	9.66711	9.66362	(9.66712)	9.66738	0.016	13.8048	13.7903	13.7979	1.4	0.003	0.003	0.003	0.0

*Energies E , Einstein A values, and emissivities ε in SPEX v3.03 (S3), AtomDB/APEC v3.0.8 (A), SPEX v2 (S2), and CHIANTI v8.0 (C).[†]Coefficient of variation (standard deviation divided by the mean) on energies E , A values, and emissivities ε .

fine-tuning (appendix 1.2). The original and new correction factors are respectively shown with the blue and red curves in figure 22a. A poorer fit ($\delta C_{\text{stat}} = 191$; “Ground ARF” in table 1) is obtained with the new correction, and the best-fit CIE emission measure changes by 4%. The temperature decreases by 0.12 keV and the

abundances changes by ≤ 0.06 solar from the original values.

A.3.4.4. Correction using the Crab observation

The third method to evaluate and correct systematic uncertainty in effective area is to use standard candles. The Crab

Table 11. Same as table 10, but for satellite lines.

Line		E (keV)*				f_E^\dagger	$\log_{10} A$ (s ⁻¹)*			f_A^\dagger	ε (10 ⁻²³ m ³ s ⁻¹)*			f_ε^\dagger
Transition	Key [‡]	S3	A	S2	C	(%)	S3	A	C	(%)	S3	A	C	(%)
<i>L-shell lines</i>														
..... He-like Fe XXV														
1s.2s ³ S ₁ -1s.5p ³ P ₂		1.84960	1.84966	—	1.84971	0.002	12.2967	12.1875	12.2487	10.2	0.014	0.011	0.011	11.8
..... Li-like Fe XXIV														
2p ² P _{3/2} -7s ² S _{1/2}		1.81905	1.81893	—	1.81990	0.024	11.1216	11.1216	10.8681	24.4	0.012	0.009	—	14.3
2p ² P _{3/2} -7d ² D _{5/2}		1.82117	1.82679	—	1.82107	0.147	12.0434	12.0430	12.0043	4.2	0.028	0.030	0.006	51.0
2s ² S _{1/2} -6p ² P _{1/2}		1.82640	1.82634	1.82625	1.82641	0.003	11.9879	11.9993	11.9330	6.5	0.039	0.033	0.006	55.2
2s ² S _{1/2} -6p ² P _{3/2}		1.82698	1.82116	1.82706	1.82700	0.139	11.9882	11.9952	11.9335	6.2	0.078	0.066	0.013	54.0
2p ² P _{1/2} -7d ² D _{3/2}		1.83703	1.83626	—	1.83716	0.022	11.9721	11.9721	11.9360	3.9	0.016	0.016	0.003	52.5
2s ² S _{1/2} -7p ² P _{1/2}		1.88463	1.88470	—	1.88540	0.018	11.7868	11.8027	11.6875	11.2	0.021	0.018	—	7.7
2s ² S _{1/2} -7p ² P _{3/2}		1.88500	1.88506	—	1.88580	0.019	11.7871	11.7991	11.6875	11.0	0.042	0.036	—	7.7
..... Li-like Ni XXVI														
2s ² S _{1/2} -4p ² P _{1/2}		1.81758	1.81758	—	1.81760	0.001	12.6517	12.6222	12.6312	2.9	0.019	0.018	0.019	2.5
2s ² S _{1/2} -4p ² P _{3/2}		1.82033	1.82033	1.82062	1.82035	0.007	12.6537	12.6232	12.6334	2.9	0.037	0.037	0.038	1.3
2s ² S _{1/2} -5p ² P _{3/2}		2.02916	2.02916	2.02589	2.02920	0.070	12.3649	12.2765	12.3292	8.3	0.012	0.012	0.012	0.0
<i>K-shell lines</i>														
..... He-like S XV														
1s.2p ¹ P ₁ -2p ² ¹ D ₂	J	2.59113	2.59121	2.59148	—	0.006	13.8773	13.8876	—	1.2	0.013	0.013	—	0.0
..... He-like Fe XXV														
1s.2p ¹ P ₁ -2p ² ¹ D ₂	J	6.91876	6.91876	6.91992	—	0.008	14.6230	14.6365	—	1.5	0.024	0.026	—	4.0
1s.2s ¹ S ₀ -2s.2p ¹ P ₁	T	6.93763	6.93735	6.94162	—	0.028	14.4293	14.4456	—	1.9	0.011	0.013	—	8.3
..... Li-like Fe XXIV														
2p ² P _{3/2} -1s.2s ² ² S _{1/2}	o	6.53583	6.53615	6.53305	6.53624	0.020	12.9854	12.9576	12.9576	3.1	0.018	0.013	0.011	21.0
2p ² P _{1/2} -1s.2s ² ² S _{1/2}	p	6.55180	6.55169	6.54892	6.55179	0.019	12.9702	12.9420	12.9420	3.1	0.017	0.012	0.011	19.7
2s ² S _{1/2} -1s.2s.(³ S).2p ⁴ P _{1/2}	v	6.61369	6.61355	6.61320	6.61329	0.003	12.6901	12.9974	12.6920	36.0	0.012	0.023	0.012	33.1
2s ² S _{1/2} -1s.2s.(³ S).2p ⁴ P _{3/2}	u	6.61666	6.61673	6.61708	6.61682	0.002	13.1965	13.4914	13.2014	34.3	0.029	0.050	0.026	30.5
2p ² P _{3/2} -1s.2p ² ⁴ S _{5/2}	e	6.62041	6.62061	6.61708	6.62071	0.023	13.5223	13.5453	13.5453	2.5	0.044	0.045	0.046	1.8
2s ² S _{1/2} -1s.2s.(³ S).2p ⁴ P _{5/2}	—	6.62781	6.62805	—	—	0.002	9.7959	10.0906	—	32.7	0.034	0.049	—	18.1
2p ² P _{3/2} -1s.2p ² ² D _{3/2}	l	6.63812	6.63940	6.63656	6.63950	0.018	13.5829	13.5798	13.5911	1.1	0.021	0.019	0.019	4.8
2p ² P _{3/2} -1s.2p ² ² D _{5/2}	j	6.64445	6.64474	6.64225	6.64484	0.016	14.3226	14.3304	14.3345	1.1	0.259	0.242	0.241	3.3
2s ² S _{1/2} -1s.2s.(¹ S).2p ² P _{1/2}	r	6.65348	6.65330	6.65045	6.65339	0.019	14.4953	14.5038	14.5038	0.9	0.100	0.127	0.101	11.4
2p ² P _{1/2} -1s.2p ² ² D _{3/2}	k	6.65409	6.65509	6.65223	6.65518	0.018	14.5028	14.5145	14.5145	1.3	0.171	0.171	0.162	2.5
2p ² P _{3/2} -1s.2p ² ² P _{3/2}	a	6.65780	6.65794	6.65544	6.65804	0.016	14.7858	14.7931	14.7931	0.8	0.067	0.073	0.060	8.0
2s ² S _{1/2} -1s.2s.(³ S).2p ² P _{3/2}	q	6.66194	6.66188	6.65973	6.66233	0.015	14.6800	14.9741	14.6875	34.0	0.203	0.353	0.200	28.3
3s ² S _{1/2} -1s.2p.(³ P).3s ² P _{1/2}	a4	6.67078	6.67048	6.66941	6.67058	0.008	13.9225	13.9222	13.9222	0.0	0.020	0.018	0.021	6.3
2s ² S _{1/2} -1s.2s.(³ S).2p ² P _{1/2}	t	6.67644	6.67623	6.67479	6.67632	0.010	14.2499	14.2529	14.2529	0.3	0.089	0.109	0.078	13.9
2p ² P _{3/2} -1s.2p ² ² S _{1/2}	m	6.67690	6.67803	6.67587	6.67812	0.014	14.3786	14.3856	14.3856	0.8	0.024	0.023	0.024	2.0
2s ² S _{1/2} -1s.2s.(¹ S).2p ² P _{3/2}	s	6.67915	6.67911	6.67767	6.67920	0.010	11.9783	11.8910	11.8910	9.8	0.017	0.004	0.008	56.2
3p ² P _{3/2} -1s.2p.(¹ P).3p ² D _{5/2}	d13	6.69054	6.69028	6.68920	6.69037	0.008	14.6241	14.6474	14.6474	2.5	0.060	0.062	0.071	7.4
3p ² P _{1/2} -1s.2p.(¹ P).3p ² D _{3/2}	d15	6.69327	6.69281	6.69208	6.69290	0.006	14.5955	14.6201	14.6201	2.6	0.045	0.049	0.056	9.1
3p ² P _{3/2} -1s.2p.(¹ P).3p ² P _{3/2}	d5	6.69432	6.69353	6.69281	6.69362	0.008	14.5986	14.6253	14.6253	2.9	0.023	0.021	0.025	7.1
3d ² D _{5/2} -1s.2p.(¹ P).3d ² F _{7/2}	h15	6.69597	6.69570	6.69534	6.69579	0.003	14.5762	14.6053	14.6053	3.1	0.036	0.046	0.053	15.5
4p ² P _{3/2} -1s.2p.(¹ P).4p ² D _{5/2}	m13	6.69643	6.69642	6.69534	6.69652	0.007	14.6560	14.6758	14.6758	2.1	0.014	0.015	0.017	8.1
4p ² P _{1/2} -1s.2p.(¹ P).4p ² D _{3/2}	—	6.69705	6.69678	6.69642	6.69688	0.003	14.6468	14.6656	14.6656	2.0	0.016	0.017	0.019	7.2
4d ² D _{5/2} -1s.2p.(¹ P).4d ² F _{7/2}	r15	6.69824	6.69787	6.69715	6.69796	0.006	14.6573	14.6767	14.6767	2.1	0.016	0.019	0.022	12.9
3d ² D _{5/2} -1s.2p.(¹ P).3d ² F _{5/2}	h16	6.69939	6.69932	6.69823	6.69869	0.007	14.2204	14.6776	14.2765	50.9	0.011	0.009	0.017	27.6
3d ² D _{3/2} -1s.2p.(¹ P).3d ² F _{5/2}	h17	6.70106	6.70004	6.69968	6.70013	0.008	14.2982	14.3096	14.3096	1.2	0.013	0.016	0.018	13.1
2p ² P _{3/2} -1s.2p.(³ P).3p ² D _{5/2}	j3	7.78252	7.78111	—	7.78122	0.008	14.0043	14.0128	14.0128	0.9	0.042	0.045	0.051	8.1
2s ² S _{1/2} -1s.2s.(³ S).3p ² P _{3/2}	q3	7.79082	7.78991	—	7.79002	0.005	13.7424	13.7275	13.7275	1.6	0.011	0.023	0.012	35.5
2s ² S _{1/2} -1s.2s.(¹ S).3p ² P _{3/2}	s3	7.82046	7.81988	—	7.81999	0.003	13.6441	13.6571	13.6571	1.4	0.012	0.004	0.011	39.5
2p ² P _{3/2} -1s.2p.(³ P).4p ² D _{5/2}	j4	8.16933	8.16814	—	8.16826	0.007	13.4852	13.4997	13.4997	1.6	0.018	0.018	0.021	7.4
..... Li-like Ni XXVI														
2p ² P _{3/2} -1s.2p ² ² D _{5/2}	j	7.74435	7.74465	7.73451	7.74477	0.056	14.4252	14.4378	14.4378	1.4	0.013	0.013	0.014	3.5
2s ² S _{1/2} -1s.2s.(³ S).2p ² P _{3/2}	q	7.76352	7.76552	7.74418	7.76368	0.112	14.8067	14.8202	14.8169	1.3	0.012	0.010	0.012	8.3
..... Be-like Fe XXIII														
2s.2p ³ P ₂ -1s.(2s.2p ² .2D) ³ ³ D ₃	Σ ₄	6.61012	6.60932	6.60756	6.61047	0.017	14.3508	14.3690	14.3483	2.1	0.014	0.001	0.019	66.9
2s ² ¹ S ₀ -1s.2s ² .2p ¹ P ₁	β	6.62844	6.62876	6.62663	6.62920	0.015	14.6438	14.9415	14.6405	35.2	0.018	0.040	0.024	34.0

*Energies E , A values, and emissivities ε in SPEX v3.03 (S3), AtomDB/APEC v3.0.8 (A), SPEX v2 (S2), and CHIANTI v8.0 (C).[†]Coefficient of variation (standard deviation divided by the mean) on energies E , A values, and emissivities ε .[‡]Key letters for K-shell lines. For 1s-2p and 1s-2s Li-like satellite lines (1s².nl-1s.2p.nl and 1s².nl-1s.2s.nl), notations are by Gabriel (1972), Bely-Dubau, Gabriel, and Volonte (1979), and Bely-Dubau et al. (1982) for $n = 2$ (a-v), 3 (a1-i11), and 4 (j1-u30), respectively. Those for Li-like satellite lines but with $\Delta n \geq 2$ transitions are by Phillips (2008) (a-v with the upper n subscripted). Key letters for He-like (upper cases) and Be-like (Greeks) satellites respectively follow Safronova's notation and Doschek, Feldman, and Cowan (1981).

is one of the broadly used reference sources for effective area calibration. Using a 9.7-ks observation, Tsujimoto et al. (2018) found that the SXS spectrum of the Crab showed a systematic deviation from the canonical model. The deviation, defined as the SXS-to-canonical ratio, behaves differently depending on the energy bands, but in the 3–9 keV band it shows a monotonically decreasing trend on energy within $\pm 5\%$. This is reminiscent of our effective area correction with *knak*, as shown in figure 22a. Therefore, we re-run the baseline fit with the Crab ratio as an effective-area correction instead of the original factor in appendix 1.2.

As shown table 1 (“Crab ARF”), the Crab correction does improve the fit from the no-correction case (“No ARF cor.”) by $\delta C_{\text{stat}} = 25$. This accounts for two-thirds of the improvement by using the original correction factor ($\delta C_{\text{stat}} = 38$). The slightly worse fit than the baseline model might be attributable to the different observation configurations between Perseus and Crab: different pixel contributions and event-grade selections due to different spatial extents of the sources and incoming photon rates.

A.3.4.5. ARF with the latest aharfgen

A newer version (006) of the Hitomi software has been released including an updated ray-tracing ARF generator *aharfgen*, in which a bug in the coordinates calculation for an input image is corrected. A comparison of effective areas between the old and new tools, as well as the new-to-old area ratio, are shown in figure 22b. The ratio curve has an almost constant, smooth structure over the fitting range without any line- or edge-like features. The notable difference is rather in the total effective area. The $\sim 20\%$ lower area results in a comparable increase in the ICM emission measure (“New arfgen” in table 1). Although the new ARF marginally improves the fit, any changes in the best-fit values of the other parameters are less than 0.1%, justifying the use of the old ARF in the baseline model for the current purpose.

A.3.5. Effects of the gain correction factor

The correction on energy scale is crucial for fitting the emission lines. Once it is removed, the fit with the baseline model becomes worse by $\delta C_{\text{stat}} = 627$, and the Si, S, and Fe abundances are affected up to 15%. The temperature and line broadening are not affected by the energy-scale correction.

Appendix 4. Hitomi SXS spectral fits with different codes

Figures 23–25 show the full-band (1.9–9.5 keV) Hitomi SXS spectrum with the best-fit baseline model using SPEX version 3.03 and the relative differences of the best-fit

models obtained with various other plasma models. See section 4 for details.

Appendix 5. List of emission lines

Tables 10 and 11 respectively compare the line energies E of the strongest lines and satellite lines in the observed spectrum between different plasma codes. Einstein coefficient values A and emissivities ε are also compared. The emissivity thresholds are 10^{-26} photons $\text{m}^3 \text{s}^{-1}$ and 10^{-25} photons $\text{m}^3 \text{s}^{-1}$, respectively. See section 4 for details.

References

- Aggarwal, K. M., & Kingston, A. E. 1992, *Phys. Scr.*, 46, 193
- Aglitskii, E. V., Boiko, V. A., Zakharov, S. M., Pikuz, S. A., & Faenov, A. I. 1974, *Soviet J. Quant. Electron.*, 4, 908
- Aglitsky, E. V., Antsiferov, P. S., Mandelstam, S. L., Panin, A. M., Safronova, U. I., Ulitin, S. A., & Vainshtein, L. A. 1988, *Phys. Scr.*, 38, 136
- Angelini, L., et al. 2016, *Proc. SPIE*, 9905, 990514
- Arnaud, K. A. 1996, in *ASP Conf. Ser.*, 101, *Astronomical Data Analysis Software and Systems V*, ed. G. H. Jacoby & J. Barnes (San Francisco: ASP), 17
- Arnaud, M., & Raymond, J. 1992, *ApJ*, 398, 394 (AR92)
- Arnaud, M., & Rothenflug, R. 1985, *A&AS*, 60, 425 (AR85)
- Artemyev, A. N., Shabaev, V. M., Yerokhin, V. A., Plunien, G., & Soff, G. 2005, *Phys. Rev. A*, 71, 062104
- Audard, M., Güdel, M., Sres, A., Raassen, A. J. J., & Mewe, R. 2003, *A&A*, 398, 1137
- Ballance, C. P., Badnell, N. R., & Berrington, K. A. 2002, *J. Phys. B*, 35, 1095
- Bearden, J. A. 1967, *Rev. Mod. Phys.*, 39, 78
- Beiersdorfer, P. 2009, *Can. J. Phys.*, 87, 9
- Beiersdorfer, P., Bitter, M., von Goeler, S., & Hill, K. W. 1989, *Phys. Rev. A*, 40, 150
- Beiersdorfer, P., & Brown, G. V. 2015, *Phys. Rev. A*, 91, 032514
- Beiersdorfer, P., Phillips, T. W., Wong, K. L., Marrs, R. E., & Vogel, D. A. 1992, *Phys. Rev. A*, 46, 3812
- Bely-Dubau, F., Faucher, P., Steenman-Clark, L., Bitter, M., von Goeler, S., Hill, K. W., Camhy-Val, C., & Dubau, J. 1982, *Phys. Rev. A*, 26, 3459
- Bely-Dubau, F., Gabriel, A. H., & Volonte, S. 1979, *MNRAS*, 186, 405
- Berlok, T., & Pessah, M. E. 2016, *ApJ*, 833, 164
- Bernitt, S., et al. 2012, *Nature*, 492, 225
- Beyer, H. F., Deslattes, R. D., Folkmann, F., & La Villa, R. E. 1985, *J. Phys. B*, 18, 207
- Bitter, M., Hill, K. W., Goeler, S. V., Stodiek, W., Beiersdorfer, P., Rice, J. E., & Ince-Cushman, A. 2008, *Can. J. Phys.*, 86, 291
- Böhringer, H., & Werner, N. 2010, *A&A Rev.*, 18, 127
- Bombarda, F., Giannella, R., Kallne, E., Tallents, G. J., & Bely-Dubau, F. 1988, *Phys. Rev. A*, 37, 504
- Brown, G. V., et al. 2006, *Phys. Rev. Lett.*, 96, 253201
- Bruhns, H., Braun, J., Kubiček, K., Crespo, López-Urrutia J. R., & Ullrich, J. 2007, *Phys. Rev. Lett.*, 99, 113001

- Bryans, P., Landi, E., & Savin, D. W. 2009, *ApJ*, 691, 1540 (B09)
- Cash, W. 1979, *ApJ*, 228, 939
- Chantler, C. T., Laming, J. M., Dietrich, D. D., Hallett, W. A., McDonald, R., & Silver, J. D. 2007, *Phys. Rev. A*, 76, 042116
- Cheng, K. T., Chen, M. H., Johnson, W. R., & Sapirstein, J. 1994, *Phys. Rev. A*, 50, 247
- Chuzhoy, L., & Nusser, A. 2003, *MNRAS*, 342, L5
- Conselice, C. J., Gallagher, III, J. S., & Wyse, R. F. G. 2001, *AJ*, 122, 2281
- de Plaa, J., Zhuravleva, I., Werner, N., Kaastra, J. S., Churazov, E., Smith, R. K., Raassen, A. J. J., & Grange, Y. G. 2012, *A&A*, 539, A34
- Del Zanna, G., Dere, K. P., Young, P. R., Landi, E., & Mason, H. E. 2015, *A&A*, 582, A56
- Dere, K. P., Landi, E., Mason, H. E., Monsignori Fossi, B. C., & Young, P. R. 1997, *A&AS*, 125, 149
- Doschek, G. A., Feldman, U., & Cowan, R. D. 1981, *ApJ*, 245, 315
- Drake, G. 1988, *Can. J. Phys.*, 66, 586
- Erickson, G. W. 1977, *J. Phys. Chem. Ref. Data* 6, 831
- Ettori, S., & Fabian, A. C. 2006, *MNRAS*, 369, L42
- Fabian, A. C., & Pringle, J. E. 1977, *MNRAS*, 181, 5P
- Ferland, G. J., et al. 2013, *Rev. Mexicana Astron. Astrofis.*, 49, 137
- Ferruit, P., Adam, G., Binette, L., & Pécontal, E. 1997, *New Astron.*, 2, 345
- Foster, A. R., Ji, L., Smith, R. K., & Brickhouse, N. S. 2012, *ApJ*, 756, 128
- Fujimoto, R., et al. 2016, *Proc. SPIE*, 9905, 99053S
- Fukazawa, Y., Ohashi, T., Fabian, A. C., Canizares, C. R., Ikebe, Y., Makishima, K., Mushotzky, R. F., & Yamashita, K. 1994, *PASJ*, 46, L55
- Gabriel, A. H. 1972, *MNRAS*, 160, 99
- Gabriel, A. H., & Phillips, K. J. H. 1979, *MNRAS*, 189, 319
- Gilfanov, M. R., & Syunyaev, R. A. 1984, *Soviet Astron. Lett.*, 10, 137
- Gu, L., Kaastra, J., & Raassen, A. J. J. 2016a, *A&A*, 588, A52
- Gu, L., Mao, J., Costantini, E., & Kaastra, J. 2016b, *A&A*, 594, A78
- Gu, M. F. 2008, *Can. J. Phys.*, 86, 675
- Gu, M., Beiersdorfer, P., Brown, G., Graf, A., Kelley, R., Kilbourne, C., Porter, F., & Kahn, S. 2012, *Can. J. Phys.*, 90, 351
- Hitomi Collaboration 2016, *Nature*, 535, 117
- Hitomi Collaboration 2017a, *ApJ*, 837, L15
- Hitomi Collaboration 2017b, *Nature*, 551, 478 (Z paper)
- Hitomi Collaboration 2018a, *PASJ*, 70, 9 (V paper)
- Hitomi Collaboration 2018b, *PASJ*, 70, 10 (RS paper)
- Hitomi Collaboration 2018c, *PASJ*, 70, 11 (T paper)
- Hitomi Collaboration 2018d, *PASJ*, 70, 13 (AGN paper)
- Indelicato, P., Gorceix, O., Tavernier, M., Briand, J. P., Desclaux, J. P., Marrus, R., & Prior, M. 1986, *Z. Physik D Atoms Molecules Clusters*, 2, 149
- Inoue, S., Hayashida, K., Ueda, S., Nagino, R., Tsunemi, H., & Koyama, K. 2016, *PASJ*, 68, S23
- Ishisaki, Y., et al. 2016, *Proc. SPIE*, 9905, 99053T
- Johnson, W. R., Cheng, K. T., & Plante, D. R. 1997, *Phys. Rev. A*, 55, 2728
- Johnson, W. R., & Soff, G. 1985, *At. Data and Nucl. Data Tables*, 33, 405
- Kaastra, J. S., et al. 2004, *A&A*, 413, 415
- Kaastra, J. S., & Bleeker, J. A. M. 2016, *A&A*, 587, A151
- Kaastra, J. S., Bykov, A. M., & Werner, N. 2009, *A&A*, 503, 373
- Kaastra, J. S., Ferrigno, C., Tamura, T., Paerels, F. B. S., Peterson, J. R., & Mittaz, J. P. D. 2001, *A&A*, 365, L99
- Kaastra, J. S., Mewe, R., & Nieuwenhuijzen, H. 1996, in *UV and X-ray Spectroscopy of Astrophysical and Laboratory Plasmas*, ed. K. Yamashita & T. Watanabe (Universal Academy Press: Tokyo), 411
- Kaastra, J. S., Paerels, F. B. S., Durret, F., Schindler, S., & Richter, P. 2008, *Space Sci. Rev.*, 134, 155
- Kaufman, V., & Martin, W. C. 1993, *J. Phys. Chem. Ref. Data*, 22, 279
- Kelly, R. L. 1987, *J. Phys. Chem. Ref. Data*, 16
- Kelley, R. L., et al. 2016, *Proc. SPIE*, 9905, 99050V
- Kilbourne, C. A., et al. 2018, *PASJ*, 70, 18
- Kisielius, R., Berrington, K. A., & Norrington, P. H. 1996, *A&AS*, 118, 157
- Kubiček, K., Mokler, P. H., Mäkel, V., Ullrich, J., & López-Urrutia, J. R. C. 2014, *Phys. Rev. A*, 90, 032508
- Landini, M., & Monsignori Fossi, B. C., 1970, *A&A*, 6, 468
- Li, S., Yan, J., Li, C. Y., Si, R., Guo, X. L., Huang, M., Chen, C. Y., & Zou, Y. M. 2015, *A&A*, 583, A82
- Lodders, K., & Palme, H. 2009, *Meteorit. Planet. Sci. Suppl.*, 72, 5154
- Maeda, Y., et al. 2018, *PASJ*, 70, 19
- Medvedev, P., Gilfanov, M., Sazonov, S., & Shtykovskiy, P. 2014, *MNRAS*, 440, 2464
- Mehdipour, M., Kaastra, J. S., & Raassen, A. J. J. 2015, *A&A*, 579, A87
- Mendoza, C., Kallman, T. R., Bautista, M. A., & Palmeri, P. 2004, *A&A*, 414, 377
- Mernier, F., de Plaa, J., Kaastra, J. S., & Zhang, Y. Y. 2016, *A&A* submitted
- Mewe, R. 1972, *Sol. Phys.*, 22, 459
- Mewe, R., Gronenschild, E. H. B. M., & van den Oord, G. H. J. 1985, *A&AS*, 62, 197
- Mewe, R., Kaastra, J. S., & Liedahl, D. A. 1995, *Legacy*, 6, 16
- Mighell, K. J. 1999, *ApJ*, 518, 380
- Mitchell, R. J., Culhane, J. L., Davison, P. J. N., & Ives, J. C. 1976, *MNRAS*, 175, 29P
- Mullen, P. D., Cumbee, R. S., Lyons, D., & Stancil, P. C. 2016, *ApJS*, 224, 31
- Mushotzky, R., Loewenstein, M., Arnaud, K. A., Tamura, T., Fukazawa, Y., Matsushita, K., Kikuchi, K., & Hatsukade, I. 1996, *ApJ*, 466, 686
- Natarajan, L., & Kadrekar, R. 2013, *Phys. Rev. A*, 88, 012501
- Nousek, J. A., & Shue, D. R. 1989, *ApJ*, 342, 1207
- Nussbaumer, H., & Schmutz, W. 1984, *A&A*, 138, 495
- Palmeri, P., Mendoza, C., Kallman, T. R., & Bautista, M. A. 2003a, *A&A*, 403, 1175
- Palmeri, P., Mendoza, C., Kallman, T. R., Bautista, M. A., & Meléndez, M. 2003b, *A&A*, 410, 359
- Palmeri, P., Quinet, P., Mendoza, C., Bautista, M. A., García, J., & Kallman, T. R. 2008, *ApJS*, 177, 408
- Palmeri, P., Quinet, P., Mendoza, C., Bautista, M. A., García, J., Witthoeft, M. C., & Kallman, T. R. 2010, *A&A*, 525, A59

- Palmeri, P., Quinet, P., Mendoza, C., Bautista, M. A., García, J., Witthoeft, M. C., & Kallman, T. R. 2012, *A&A*, 543, A44
- Peterson, J. R., et al. 2001, *A&A*, 365, L104
- Peterson, J. R., & Fabian, A. C. 2006, *Phys. Rep.*, 427, 1
- Phillips, K. J. H. 2008, *A&A*, 490, 823
- Plucinsky, P. P., Beardmore, A. P., Foster, A., Haberl, F., Miller, E. D., Pollock, A. M. T., & Sembay, S. 2017, *A&A*, 597, A35
- Qin, B., & Wu, X.-P. 2000, *ApJ*, 529, L1
- Raymond, J. C., & Smith, B. W. 1977, *ApJS*, 35, 419
- Rice, J. E., et al. 2014, *J. Phys. B*, 47, 075701
- Rice, J. E., et al. 2015, *J. Phys. B*, 48, 144013
- Rosen, A. S., Reinke, M. L., Rice, J. E., Hubbard, A. E., & Hughes, J. W. 2014, *J. Phys. B*, 47, 105701
- Rudolph, J. K., et al. 2013, *Phys. Rev. Lett.*, 111, 103002
- Salomé, P., Combes, F., Revaz, Y., Downes, D., Edge, A. C., & Fabian, A. C. 2011, *A&A*, 531, A85
- Sawada, M., & Koyama, K. 2012, *PASJ*, 64, 81
- Schellenberger, G., Reiprich, T. H., Lovisari, L., Nevalainen, J., & David, L. 2015, *A&A*, 575, A30
- Schleinkofer, L., Bell, F., Betz, H.-D., Trollmann, G., & Rothmel, J. 1982, *Phys. Scr.*, 25, 917
- Scofield, J. H. 1974, *At. Data and Nucl. Data Tables*, 14, 121
- Seta, H., et al. 2012, *Proc. SPIE*, 8443, 84435D
- Shirai, T., Sugar, J., Musgrove, A., & Wiese, W. L. 2000, *Spectral Data for Highly Ionized Atoms: Ti, V, Cr, Mn, Fe, Co, Ni, Cu, Kr, and Mo* (American Institute of Physics: New York)
- Smith, A. J., Bitter, M., Hsuan, H., Hill, K. W., von Goeler, S., Timberlake, J., Beiersdorfer, P., & Osterheld, A. 1993, *Phys. Rev. A*, 47, 3073
- Smith, R. K., Brickhouse, N. S., Liedahl, D. A., & Raymond, J. C. 2001, *ApJ*, 556, L91
- Sugar, J., & Corliss, C. 1985, *J. Phys. Chem. Ref. Data*, 14, Suppl. No. 2
- Takahashi, T., et al. 2016, *Proc. SPIE*, 9905, 99050U
- Tamura, T., et al. 2001, *A&A*, 365, L87
- Tsujimoto, M., et al. 2016, *Proc. SPIE*, 9905, 99050Y
- Tsujimoto, M., et al. 2018, *PASJ*, 70, 14
- Urban, O., et al. 2014, *MNRAS*, 437, 3939
- Urdampilleta, I., Kaastra, J. S., & Mehdipour, M. 2017, *A&A*, 601, A85 (U17)
- Walker, S. A., Kosec, P., Fabian, A. C., & Sanders, J. S. 2015, *MNRAS*, 453, 2480
- Werner, N., Durret, F., Ohashi, T., Schindler, S., & Wiersma, R. P. C. 2008, *Space Sci. Rev.*, 134, 337
- Whiteford, A. D., Badnell, N. R., Ballance, C. P., O'Mullane, M. G., Summers, H. P., & Thomas, A. L. 2001, *J. Phys. B*, 34, 3179
- Yerokhin, V. A., & Shabaev, V. M. 2015, *J. Phys. Chem. Ref. Data*, 44, 033103
- Zhang, H., & Sampson, D. H. 1987, *ApJS*, 63, 487
- Zhuravleva, I., et al. 2014, *Nature*, 515, 85